Aerodynamics of flexible membranes

Rojratsirikul, Pinunta

Award date:
2010

Awarding institution:
University of Bath

AERODYNAMICS OF FLEXIBLE MEMBRANES

Pinunta Rojratsirikul

A thesis submitted for the degree of Doctor of Philosophy

University of Bath

Department of Mechanical Engineering

October 2010

ABSTRACT

Membrane wings are used both in nature and small aircraft as lifting surfaces. For these low Reynolds number applications, separated flows are common and are the main sources of unsteadiness. Adaptability of the membrane wing is known to improve the vehicle performance; and membrane compliancy in animal wings such as bats contributes significantly to their astonishing flights. Yet, the aerodynamic characteristics of the membranes are still largely unknown.

An experimental study of flexible membranes at low Reynolds numbers was undertaken. Two-dimensional membrane aerofoils were investigated, with particular focus on the unsteady aspects. Membrane deformation, flow fields and fluid-structure interaction were examined over a range of angles of attack and freestream velocities. A comprehensive study of the effect of membrane pre-strain and excess length was carried out. Low aspect ratio membrane wings were investigated for rectangular and nonslender delta wings.

The amplitude and mode of membrane vibration are found to be dependent mainly on the location and the unsteadiness level of the shear layer. The results indicate a strong coupling of unsteady flow with the membrane oscillation. With increasing Reynolds number, the separated shear layer becomes more energetic and closer to the surface. The membrane not only has smaller size of the separation region compared to a rigid aerofoil, but also excites the roll-up of large vortices which might lead to delayed stall. The membrane aerofoils with excess length exhibit higher vibration modes, earlier roll-up and smaller separated region, compared to the ones with pre-strain. This smaller separated region delays the onset of membrane vibrations to a larger incidence. For the low aspect ratio membrane wings, the combination of tip vortices and leading-edge vortex shedding results in a mixture of streamwise and spanwise vibrational modes. The flexibility benefits the rectangular wing more than the delta wing by increasing the maximum normal force and the force slope by a larger amount. Similar to the two-dimensional membrane aerofoils, the Strouhal numbers of the oscillations are on the order of unity, and there is a coupling with the wake instabilities in the post-stall region. Stronger tip vortices on membrane wings contribute significantly to total lift enhancement.

ACKNOWLEDGEMENTS

This work has been supported by the Royal Thai Government Scholarship, and the US Air Force Office of Scientific Research (AFOSR). The author would also like to thank the EPSRC Engineering Instrument Pool.

The author is grateful for the support, ideas, focus, and enthusiasm of supervisor Prof I. Gursul, and Dr Z. Wang, and for the help of technicians Mr L. Dudrudge and Mr R. Wiltshire, and instrumentation specialists Mr V. Rajput and Mr C. Brain, and her examiner Dr M. Carley. The author is appreciative of the support of everyone in the office 4E2.27.

Final, the author is grateful for the help and support of her family, and of Tnb.

CONTENTS

LIST OF FIGURES

LIST OF TABLES

NOMENCLATURE

LATIN SYMBOLS

b	wing span
c	chord length
c_e	effective chord length of membrane, excluding the length of rigid leading- and trailing-edges
C_L	lift coefficient
C_{Lmax}	maximum lift coefficient
C_n	normal force coefficient: $F_n/(\frac{1}{2}\rho U_\infty^2 S)$
$C_{n,max}$	maximum normal force coefficient
C_P	pressure coefficient: $P/(\frac{1}{2}\rho U_\infty^2)$
C_T	tension coefficient: $\overline{T}/q_\infty c$
℃	degrees Celsius
E	elastic modulus
f	frequency
f_0	natural frequency
f_s	sampling frequency
F_n	normal force
l	shear layer location
L	length of membrane
L_0	initial length of membrane
$\overline{L}$	time-averaged length of membrane
P	pressure
q_∞	dynamic pressure: $\frac{1}{2}\rho U_\infty^2$
Re	Reynolds number: $U_\infty c/\nu$
S	wing area
St	Strouhal number: fc/U_∞
S_0	pre-stress of membrane: $E\delta_0$
t	membrane thickness
T	tension
$\overline{T}$	time-averaged tension of membrane: $(S_0+E\overline{\delta})t$

u	velocity in streamwise direction
u'	fluctuating velocity in streamwise direction
$\bar{u}$	time-averaged velocity in streamwise direction
U_∞	freestream velocity
v	velocity in cross-stream direction
v'	fluctuating velocity in cross-stream direction
$\bar{v}$	time-averaged velocity in cross-stream direction
V	magnitude of velocity vector
x	chordwise direction
z	membrane displacement in direction normal to chordline
z'	membrane displacement in vertical direction
z_{max}	maximum membrane displacement in z direction
z_{SD}	standard deviation of displacement in z direction
z_{SDmax}	maximum standard deviation of displacement in z direction

GREEK SYMBOLS

α	angle of attack
α_{stall}	stall angle
Γ	circulation
δ_0	pre-strain
$\bar{\delta}$	time-averaged strain
ε	excess length ratio: $(L_0 - c_e)/c_e$
μ	viscosity
ν	kinematic viscosity: μ/ρ
ρ	density of air
ρ_m	density of membrane
ρ_s	surface density of membrane
Λ	leading-edge sweep angle
Π_1	aeroelastic parameter: $(Et/q_\infty c)^{1/3}$
ω	vorticity
$\omega c/U_\infty$	non-dimensional vorticity

ABBREVIATIONS

2D	two-dimensional
3D	three-dimensional
AR	aspect ratio
CCD (camera)	charge-coupled device
DIC	Digital Image Correlation
DPIV	digital Particle Image Velocimetry
FFT	Fast Fourier Transform
fps	frames per second
LAR	low aspect ratio
LE	leading-edge
MAV	micro air vehicle
PC	personal computer
STD	standard deviation
TE	trailing-edge

CHAPTER 1: INTRODUCTION

1.1 BACKGROUND

Flexible membranes have been associated with a number of applications including either *man-made* vehicles such as parachutes, paragliders, hang gliders, yacht sails, microlights, and Micro Air Vehicles (MAVs), or *natural flyers* such as bats. All of these applications operate under a similar idea that they are able to passively adjust the shape of the wing in accordance with the flow environment. For MAV applications in general, where the vehicles operate at Reynolds number below 10^5, poor lift and unsteadiness represent major problems in low Reynolds number aerodynamics. Even without flow separation, the low Reynolds number aerodynamics results in low lift-to-drag ratios. It is highly desirable to design MAVs that are able to operate under gust and unsteady freestream conditions. Several studies have shown that membrane wings can significantly improve longitudinal static stability, delay stall and provide a more favourable lift-to-drag ratio, and therefore enhance the overall aerodynamic performance when compared to a rigid wing of similar geometry due to its aeroelastic effects and the adaptive inflation of the membrane skin (Shyy et al. 1997; 1999a; Waszak et al. 2001; Ifju et al. 2002; Lian et al. 2003b; Deluca et al. 2004; Lian and Shyy 2005; Albertani et al. 2007; Stanford and Ifju 2009). Even membrane skin with low degree of compliance can have substantial effects on the aerodynamic performance (Shyy et al. 1999a; Levin and Shyy 2001; Lian et al. 2003a).

A growing interest in the use of membrane wings is particularly inspired by natural flyers. Flying and gliding mammals are well known for flight capabilities and agility (Bishop 2006). The flying mammals, such as bats, have thin compliant wings as lifting surfaces. These small animals with flexible membranes fly at a

low Reynolds number at moderate to high angles of attack, and exhibit high manoeuvrability. It is suggested that bat flight might be more efficient than that of large insects or small birds at comparable size (Winter and von Helversen 1998). The skin of the bat wing is known to exhibit substantial changes in shape and camber throughout the wingbeat cycle (Swartz et al. 2007) while the effects of multiple joints and anisotropic membrane stiffness across the wing (Swartz et al. 1996) are not understood.

A large amount of literature has been dedicated to this subject through numerical and experimental investigations. Most of the numerical studies have been carried out in order to simulate membrane shapes in steady flows under slightly different assumptions, boundary conditions and methods. However, the neglect of presence of flow separation and viscous effects in those numerical solutions limits the accuracy of the results. The existing potential flow theory can only be sufficient for membranes at small incidences and with small cambers. For larger incidences and cambers, viscous effects and flow separation need to be included. Unsteady aspects of the aerodynamics of membranes receive less attention even though they are far more important and critical for the vehicle performance. For example, even membrane wing MAVs that operates in steady freestream can experience aeroelastic instabilities, which may limit their operating envelope at such a low Reynolds number flight. At low incidences, even mostly attached flows may cause aeroelastic instabilities. At higher incidences, separated flows are expected to interact with the membrane structure. Unsteadiness due to separation might cause buffeting of the membrane structure. Even though the membrane wings have been of interest for over decades, existing experimental studies on this subject are limited, and are confined only to particular model configurations (such as MAVs with interior structures). Experiments that cleanly reveal the nature of interactions between flexible membranes and flows have scarcely been performed.

To fulfil fundamental yet crucial knowledge of this subject, this project thoroughly investigates flexible membranes at low Reynolds numbers. The study covers a wide range of aspects such as the time-averaged shape of membrane, mean flows, membrane oscillations, unsteady flow, and with particular emphasis on the unsteady aspects of the fluid-membrane interaction. The thesis is organised into a further six chapters. Chapter 1 is an introduction and background of

previously published literature surrounding the topic of low Reynolds number aerodynamics and flexible membranes, including experimental and computational studies for both two- and three-dimensional models. The methodology used for the current research is presented in Chapter 2, covering the experimental apparatus, measurement techniques used, how the data was processed, together with the uncertainty of measurements taken. Chapters 3 to 5 outline the results obtained and discuss what conclusions can be drawn. Chapter 3 relates to experiments conducted on two-dimensional membrane aerofoils. The results reveal the fundamental characteristics of the membrane, particularly the interactions of the membrane with the flow. Chapter 4 is a more in depth look at the effects of membrane pre-strain and excess length. How tip vortices affect these characteristics is discussed in Chapter 5 through the investigation of low aspect ratio membrane wings. Chapter 6 summarises the conclusions drawn from Chapters 3 to 5. Finally, references and the list of author's publications are given, and the published journal articles are also attached.

1.2 LITERATURE REVIEW

Firstly, the literature on low Reynolds number aerodynamics as a flow regime for the current membrane applications is presented. Separation bubbles, unsteady phenomena at high angles of attack and vortical flows associated with low aspect ratio wings at low Reynolds number are included. An extensive review for two- and three-dimensional membranes, including membrane aerofoils, sails, as well as low aspect ratio membrane wings of Micro Air Vehicles (MAVs) and bats, is provided. Finally, the wave equation for a vibrating membrane, which was used to determine the natural frequency, is presented.

1.2.1 LOW REYNOLDS NUMBER AERODYNAMICS

The Reynolds number range of 10^4 to 10^6 is considered as a 'low' Reynolds number in this thesis. According to Carmichael (1981), this is the regime where man-made aircraft and nature can be seen together in flight. Examples are large soaring birds, large radio-controlled model aircraft, human-carrying hang gliders, human-powered aircraft, and Micro Air Vehicles.

Low Reynolds number aerodynamics is a major issue of aerofoil design because the boundary layer is much less capable of handling an adverse pressure gradient without separation. The valuable reviews on the low Reynolds number aerofoils can be found at Tani (1964), Carmichael (1981), Lissaman (1983), Gad-el-Hak (1990), and Mueller (2001). The flow surrounding the leading-edge region of such low Reynolds numbers is typically laminar flow. Once the fluid momentum is not strong enough to overcome the adverse pressure gradient on the aft-side of the aerofoil, the flow is separated, as in so-called laminar separation. It is suggested that the separated laminar boundary layers around low Reynolds number aerofoils would behave more like unsteady shear layers. Once the adverse pressure gradient is adequate, and a magnitude of the boundary layer disturbance dramatically increases, the transition towards turbulence emerges. The boundary layer transition process might be related to separation bubble behaviour (Ward 1963), which will be discussed later on.

The turbulent flow induces fluid mixing within the boundary layer, which generates higher momentum fluid from near the freestream to the wall. The flow, once it overcomes the pressure gradient, quickly reattaches and forms a separation bubble (see Figure 1.1). A turbulent boundary layer is formed downstream after the reattachment point, and continues towards the trailing-edge before the flow is separated at or before the trailing-edge, so-called turbulent separation.

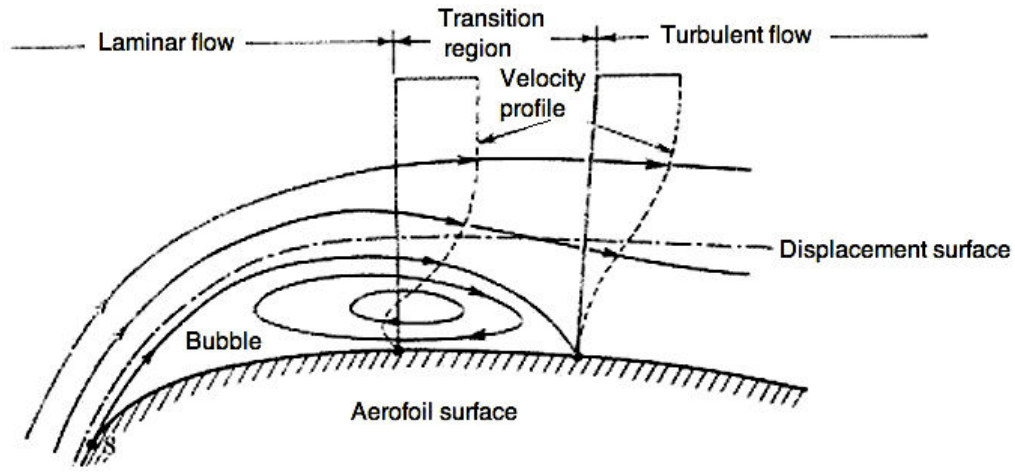

Figure 1.1: Transition, boundary layer separation and reattachment on an aerofoil. Adopted from Thwaits (1960).

Alving and Fernholz (1996) make a distinction between separation caused by sharp gradients in the surface geometry and separation from smooth surfaces caused by adverse pressure gradients. The first one is denoted as geometry-induced-separation, whereas the latter is called adverse-pressure-gradient-induces separation (APG-induced separation). The feature of the first category is that the point of separation is fixed in space and time and separation occurs for all Reynolds numbers (except creeping flow). In contrast, for the latter category, both the separation and the reattachment points can move in the streamwise direction as a response to variations of the flow environment.

SEPARATION BUBBLES AND UNSTEADY PHENOMENA

As discussed earlier, the boundary layer flow over most wings will make a transition from laminar to turbulent at some point. The transition process is often accompanied by a separation bubble, adding profile drag to the wing. Another example of separation bubble is shown in Figure 1.2.

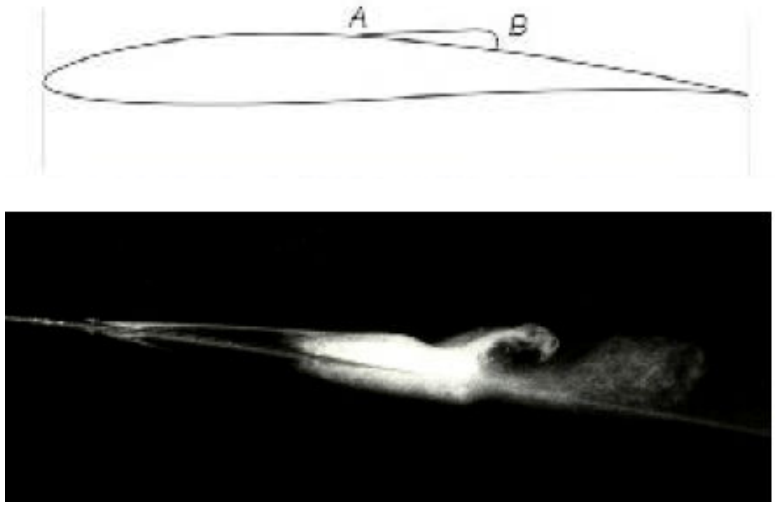

Figure 1.2: Photographs of separation bubble. Courtesy of Greg Cole and Prof Mueller (University of Notre Dame).

The separation bubble can be classified according to the status of the boundary layer at the separation and reattachment points. When the boundary layer is laminar at both separation and reattachment points, the term laminar separation bubble is used. Whereas, in the transitional bubble, the boundary layer is still laminar at separation but turbulent at reattachment. If the boundary layer is turbulent at both points, the separation bubble is called turbulent. In older aeronautical literature the term ‘laminar separation bubble’ is used to denote a

bubble where the boundary layer is laminar at separation but turbulent at reattachment, i.e. a transitional separation bubble according to the above definitions (Häggmark et al. 2001). Laminar separation bubbles are common and unless properly stabilised can lead to undesirable excessive drag and lower maximum lift. The extent of which depends on the Reynolds number. The decreases in Reynolds number cause an increase in viscous damping which tends to suppress the transition process thus delay reattachment.

Separation bubbles can also be classified as 'long' and 'short'. These two types of separation bubbles are studied by Crabtree (1957), of which the long one has a stronger effect on the aerodynamic characteristics of a thin aerofoil. This type of bubble usually starts further behind the leading-edge, with the length as much as 0.2c to 0.3c. It causes a collapse of the leading-edge pressure peak and modifies the total pressure distribution on the upper side of the aerofoil, which is associated with a large loss in lift. This can happen more severely when the bubble increases in length as the incidence is increased. When it has extended to the trailing-edge, the aerofoil stalls. The long bubble usually forms at lower Reynolds numbers.

A short bubble forms just behind the leading-edge. The length of a short bubble, sometimes referred to as a leading-edge separation bubble, is usually only a few percent of the chord length. It only represents a transition-forcing (tripping) mechanism to allow reattachment of an otherwise separated shear layer. It initiates a turbulent boundary layer without significantly altering the surface pressure distribution, thus only slightly affects the lift coefficient. In fact, the actual length from separation to reattachment does not decide whether a bubble should be termed long or short, but rather the effect of the bubble on the static pressure distribution on the surface (Häggmark et al. 2001). The short bubble is usually present at higher Reynolds numbers.

Separation bubbles are also categorised as 'strong' and 'mild' by Alving and Fernholz (1996), on the basis of the height of the shear layer upstream of separation relative to the height of the separation bubble. A separation bubble is referred to as a 'strong' bubble when the height of the shear layer preceding separation is of the same size or smaller than the height of the bubble. On the

other hand, in a 'mild' separation bubble the height of the bubble is considerably smaller than the pre-separated shear layer.

The influence of the freestream turbulence on the separation bubble along the side of a blunt plate are studied by Hillier and Cherry (1981) and Kiya and Sasaki (1983). It is found that a magnitude of bubble length, length scale of vortices in the separation region, and the suction-peak pressure could be well correlated with the turbulence outside the shear layer and near the separation point.

Whether the flow reattaches (and thus a bubble forms) or not depends on the geometry, the surface roughness, the freestream turbulence intensity, and particularly the Reynolds number and the pressure gradient. The flow is fully separated if the Reynolds number is sufficiently low to completely suppress the process of transition to turbulence, or the pressure gradient is so strong that it prevents the reattachment. The strong pressure gradient could be caused by an increasing angle of attack which moves the separation point towards the leading-edge. Once the separation point reaches the leading-edge, the lift decreases dramatically whereas the drag increases abruptly, and the aerofoil is said to stall.

At large incidences where boundary layer separation usually occurs. The wake behind an object normally consists of periodic instability waves and coherent structures. The vortex-induced vibration of an aerofoil and the lock-on phenomenon of vortex shedding frequency are among the most interesting behaviours related to the unsteady flow in the wake (Huang and Lee 2000). The development of the vortex shedding is of interest because it introduces unsteadiness, and affects the flow downstream of the object. For example, it can cause structural vibrations and noise generation. If the frequency of vortex shedding matches the resonance frequency, the structure will begin to resonate and its movement can become self-sustaining.

The wake vortex shedding frequency is usually scaled to form a Strouhal number $St = fd/U_\infty$, where f is the flow oscillation frequency, d is the cross-stream length scale of the body, and U_∞ is the freestream velocity. In the wake of a bluff body, the Strouhal number does not vary significantly over a wide range of Reynolds numbers. Typical values of the Strouhal number are reported to be nearly constant

in the range of 0.16 to 0.22 for flat-plates and thin aerofoils (Fage and Johansen 1927; Abernathy 1962; Miranda et al. 2005).

The wake of an aerofoil at post-stall angles of attack and low Reynolds numbers can be expected to behave similarly to that of a bluff body (Roshko 1954; Huang et al. 2001). However, at pre-stall angles of attack, aerofoil wake characteristics are quite different (Huang and Lin 1995; Huang and Lee 2000). Huang and Lin (1995) investigate vortex shedding of a NACA 0012 aerofoil at low Reynolds numbers. The results show a wide distribution of Strouhal numbers for different Reynolds numbers and angles of attack. Several vortex shedding modes are reported, and vortex shedding characteristics are suggested to be closely related to the behaviour of the boundary layer.

Boundary layer and turbulent wake development for a NACA 0025 aerofoil are studied by Yarusevych et al. (2006). Their results suggest that coherent structures can form in the separated flow region and in the wake of the aerofoil, which is supported by the results of Zhang et al. (2008). The roll-up of the separated shear layer, as can be seen in Figure 1.3, results in vortices forming in the boundary layer. These vortices are linked to the spatial inviscid growth of flow disturbances;

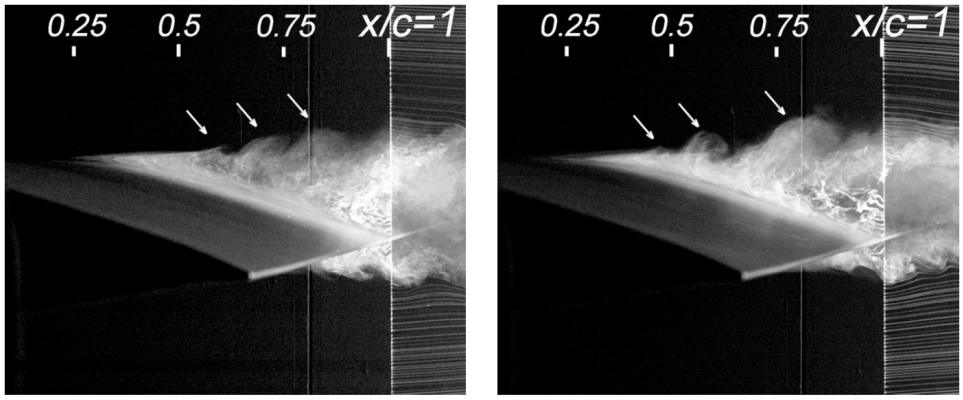

a) **b)**

Figure 1.3: Shear layer roll-up vortices, marked by the arrows, seen from the flow visualisation of separated shear layer for a NACA 0025 aerofoil at $\alpha = 5^o$: a) $Re = 55 \times 10^3$; b) $Re = 100 \times 10^3$ (Yarusevych et al. 2006).

and are similar to those produced by the Kelvin-Helmholtz instability in free shear layers. The development of the roll-up vortices leads to boundary layer transition, and the vortex breakdown during the transition process (Yarusevych et al. 2006). Their results agree well with those from different authors (Watmuff 1999; Lang et

al. 2004; McAuliffe and Yaras 2007), who suggest that coherent structures form during the stage of transition.

Focusing on the framework of the present thesis, it is impossible to ignore these sources of unsteadiness when membrane vibration is discussed. The combination of excitation frequency (due to vortex shedding), membrane tension, and distance from excitation source is a means to determine the vibration frequency of the membrane (Jenkins and Korde 2006). Due to the geometry of a model used in the current study, the presence of the separation bubbles is unavoidable even at low angle of attack because of a tripping angle between a leading edge support and the cambered membrane. However, at low incidences these separation bubbles are expected to be short or mild type, and should not alter pressure distribution significantly. At high angles of attack however, the vortex shedding, which could be related to the bursting of the laminar separation bubbles (Zhang et al. 2008), might become the dominant excitation source of the membrane vibration. And from the active flow control study of Miranda et al. (2005), the frequency of the vortex shedding is shown to be the most effective control frequency for fully separated flow. Therefore if there is a resonance between the natural frequency of the membrane and the vortex shedding frequency, the membrane's excited vibration could be a very promising passive flow control mechanism.

In terms of static response, it is reported in the study of Song et al. (2008a) that as the laminar separation bubble begins to grow when an angle of attack is close to stall, the pressure on the membrane surface rises and the membrane becomes automatically decambered. This leads to a smoother stall by preventing a sharp decrease in lift as the angle of attack is increased. These features of the membrane that improve vehicles' performances will be discussed more in section 1.2.3.

LOW ASPECT RATIO WINGS AT LOW REYNOLDS NUMBER

The main feature of the low aspect ratio wings is the existence of tip vortices. Tip vortices exist on a finite wing due to the pressure difference between the upper and lower wing surfaces. The tip vortex creates a circulatory motion that presents over the wing surfaces and hence substantially affects wing aerodynamics. For low aspect ratio wings at low Reynolds numbers in particular, the induced drag by the tip vortex substantially affects its performance. The induced drag coefficient

due to tip vortices increases as aspect ratio is decreased. Besides the effect on drag force, two contrastive impacts of the tip vortices on the lift are realised. On one hand they lower the lift forces by reducing the effective angle of attack, which is caused by a downwash component (Anderson 1989). On the other hand, they provide additional lift by creating a low pressure zone (Mueller and Delaurier 2003). The low pressure region increases with angles of attack, when the vortex strength becomes stronger. An example of the evolution of flow pattern for a rigid wing versus angles of attack, adopted from Lian et al. (2003a), is shown in Figure 1.4. The streamlines indicate that the higher pressure from the lower surface

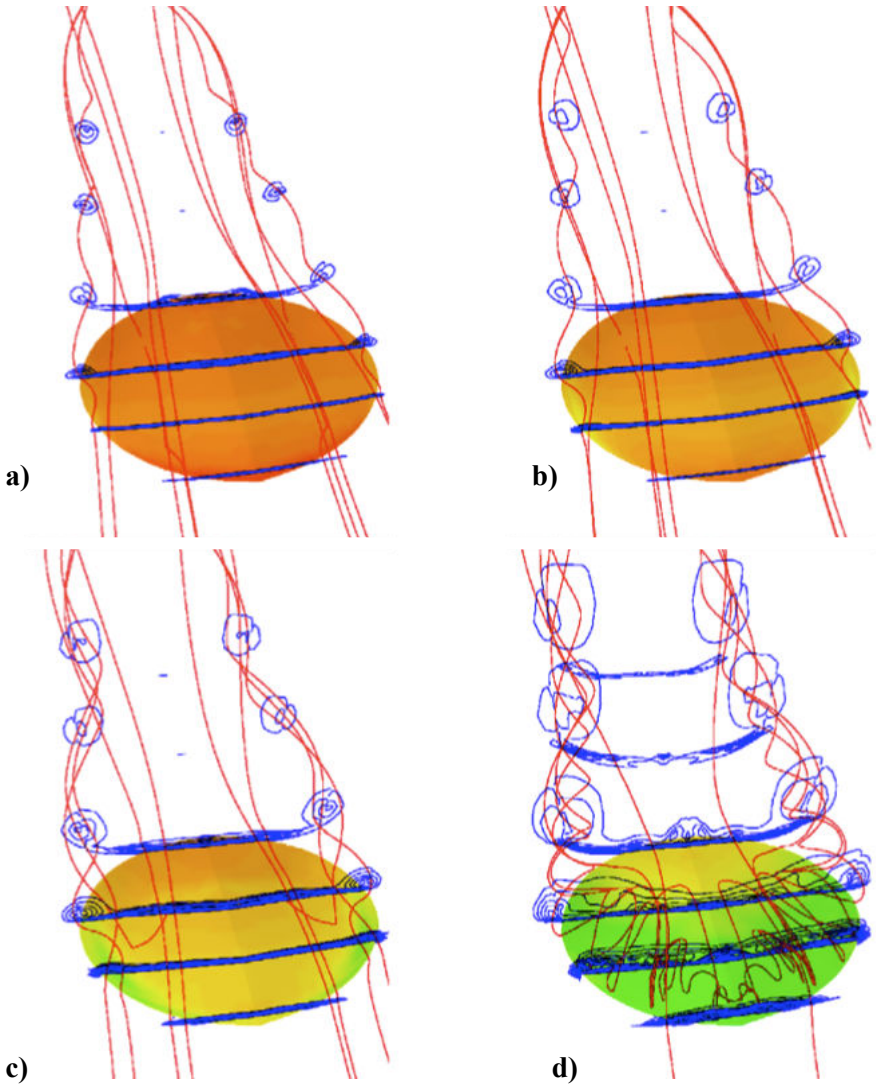

Figure 1.4: Evolution of flow pattern for a rigid wing at different angles of attack: a) $\alpha = 6^{o}$; b) $\alpha = 15^{o}$; c) $\alpha = 27^{o}$; d) $\alpha = 51^{o}$. The vortical structures are shown on selected planes. Numerical result from Lian et al. (2003a).

drives the flow toward the upper wing surface where the pressure is lower. Tip vortices are visible at small incidence ($\alpha = 6^o$), and a strong swirling motion is developed at higher incidences. The effect of endplates is found to increase lift by reducing the flow from going from the lower surface to the upper surface of the wing, hence reducing the downwash and increasing the effective angle of attack (Viieru et al. 2003; 2005). The effectiveness of the endplate diminishes as the angle of attack increases because of stronger tip vortex, however (Viieru et al. 2005).

The vortical flow structures associated with high angles of attack and delta wings are extensively reviewed by Gursul (2004; 2005). Vortical flows over a delta wing are formed by the roll-up of vortex sheets. The flow separates from the leading-edge of the wing and rolls up into a core. Distinct vortical flow can be seen on a delta wing at an angle of attack as low as $\alpha = 2.5^o$ (Taylor et al. 2003). The time-averaged axial velocity of the vortex is approximately axis-symmetric and its maximum can be as large as four or five times the freestream velocity (Gursul 2004). These high axial velocities are caused by low pressures in the vortex core, which create additional suction and lift force on the delta wings. Vortices on slender wings are not as sensitive to Reynolds numbers as nonslender vortices on low sweep angle wings. For the latter, the vortices form closer to the wing surface, and viscous interaction becomes more important (Gursul 2004). The work of Taylor and Gursul (2004a) shows that for a 50 degrees swept wing, high level of turbulence in the near surface plane occurs at the same location as the reattachment line. This indicates that the main source of turbulence on the wing surface is caused by the reattachment of the shear layer, as opposed to vortex breakdown. The effects of vortex breakdown for slender wings are the decreases in lift and nose down pitching moments. On the other hand, it has less influence on nonslender delta wings (Earnshaw and Lawford 1964). In general, vortex breakdown on the nonslender delta wings is much milder and axial flow deceleration is small. Even after vortex breakdown reaches the apex, the shear later reattachment on the wing surface is possible.

There has been a large effort to try to determine the optimum shape for low Reynolds number flight vehicles. In general, thick aerofoils (i.e. a maximum thickness is larger than 6% of the chord) exhibit very low lift performance,

whereas thin aerofoils show superior performance. Different wings of rectangular planform with aspect ratio of 5 are investigated by Schmitz (1967). The wings include a 12% maximum thickness wing, 2.9% thickness flat-plate, and 5.8% cambered-plate. It is found that the maximum lift coefficient of a thin, cambered-plate wing (C_{Lmax} = 1.05) is nearly twice that of a traditional 12% thickness wing. The results of this study indicate the advantage of the thin, cambered-wing for use in low Re regime. These results are supported by Laitone (1997), who studies rectangular wings with aspect ratios of 6 and finds that a 5% circular arc cambered with 1% thickness produces the higher lift-to-drag ratio and C_{Lmax} than a thin flat-plate and a NACA 0012 profile (see Figure 1.5). This work indicates that lift is not as dependent on a sharp trailing-edge in low Reynolds number flow as it is in higher Reynolds number aerodynamics. The rectangular planform is also investigated by Pelletier and Mueller (2000), who carry out a series of low Re tests of thin flat-plate and cambered-plate (circular-arc) wings of low aspect ratios. It is found that the cambered-plate wings outperform the flat-plates. In addition, the hysteresis of the lift curves, which usually exists in traditional wings at low Re, is virtually nonexistent in the thin plates.

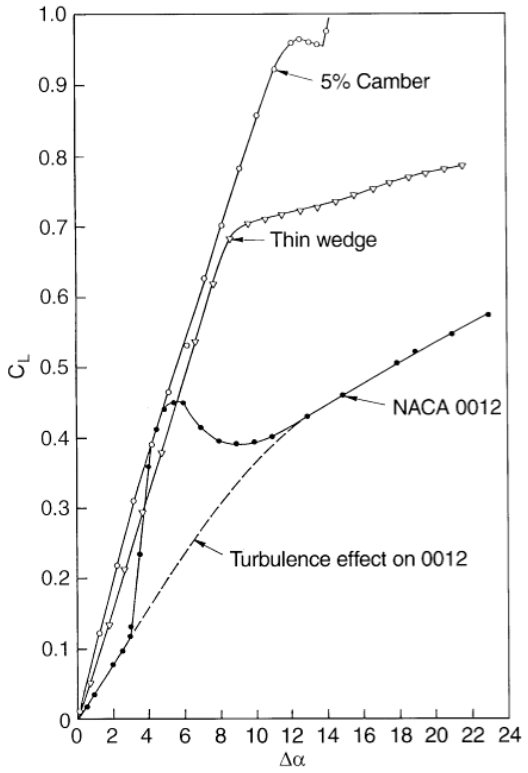

Figure 1.5: Lift coefficient for various rectangular wings of AR = 6 at Re = 20,700. Experimental result from Laitone 1997.

Torres and Mueller (2004) investigate the effects of wing planform and aspect ratio at low Reynolds numbers by using flat-plate wings. Their results show large nonlinearities in the lift curves, particularly for aspect ratios below 1.25. These wings are also found to have higher values of maximum lift coefficient and corresponding angle of attack. An example of the lift coefficient for flat-plate wings with a rectangular planform for different aspect ratios is shown in Figure 1.6. It is seen that the wings with a lower aspect ratio exhibit higher lift. This is not so surprising as tip vortices contribute to lift and affect a large portion of the wing surface. For AR ≤ 1, the rectangular and inverse Zimmerman planform have advantages over Zimmerman or elliptical planform. However, for higher values of AR, the elliptical planform performs better. The location of the center of lift which shifts with angle of attack is found to be related to the wing tip vortices. However, too much camber can result in a decrease in lift. The study on the effect of camber on the aerodynamics of rigid wings conducted by Null and Shkarayev (2005) reports that the wings with 12% camber show a considerable decrease in lift slope when compared with wings with a 3%, 6% and 9% camber. For a higher speed flight, the 3% camber wing shows the highest lift-to-drag ratio. Whereas for a lower speed flight, the 6% and 9% cambers appear to perform best.

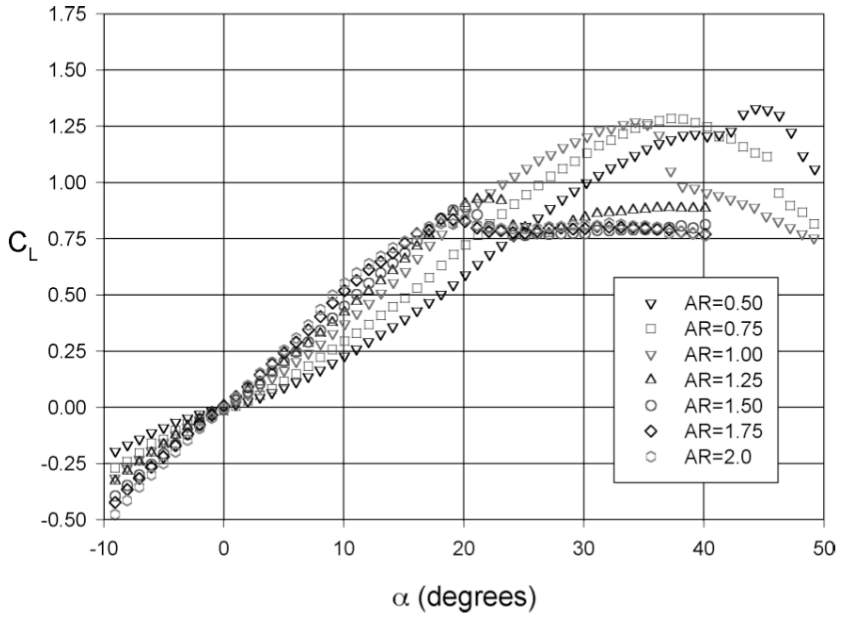

Figure 1.6: Effect of aspect ratio on lift coefficient for flat-plate rectangular wings at Re = 1×10^5. Experimental result from Torres and Mueller (2004).

1.2.2 TWO-DIMENSIONAL MEMBRANES

The study of membrane aerodynamics was first explored to improve sail design. The fundamental idea is that the sail is able to change its shape passively depending on the freestream conditions. Computational work of two-dimensional membrane aerofoils and sails is well-presented in the literature. Early work of the two-dimensional membrane aerofoil is given by Thwaites (1961), who obtains the classical *sail equation* by using the conventional linearised theory of rigid aerofoils along with the static equilibrium of each element of the sail in steady conditions. To simplify the problem, the condition is assumed to be the two-dimensional flow of an inviscid, incompressible fluid passing an infinitely long, inextensible, non-porous sail. The sail equation, which provides a basis for later research, also known as *Thwaites sail equation*, is expressed as

$$1-\frac{C_T}{2}\int_0^1 \frac{d^2(y/\alpha)/d\xi^2}{2\pi(\xi-x)}d\xi=\frac{d(y/\alpha)}{dx} \tag{1}$$

For a given value of angle of attack α and excess length ratio ε, he is able to identify the amount of lift coefficient for the sail that exceeds that of a rigid flat-plate. Thwaites (1961) concludes that the lift coefficient for a concave sail can be represented by the summation of the flat-plate lift coefficient and a term dependent on the square root of the slack ratio. The result for the sail lift coefficient is

$$C_l = 2\pi\alpha + A(L/c)^{1/2} \tag{2}$$

where L is the length of membrane and constant A is found to be slightly different for different authors; 0.636 for Thwaites (1961) and 0.7 for Greenhalgh et al. (1984).

Another feature of these analyses is that tension coefficient C_T and normalised lift slope C_L/α are the only function of the excess length ratio and angle of attack. Later work of Nielsen (1963) solves for lift, pitching moments, and membrane tension by using Fourier series methods. Complete equations for lift and tension obtained by different authors (Thwaites 1961; Neilsen 1963) are found to be slightly different. Multiple solutions are found to exist at small incidence and small excess length ratio. Hysteresis loop, which provides a negatively cambered

sail, is found when the sail approaches $\alpha = 0^o$ from negative angles. Conversely, the sail possesses a positive camber if it approaches from positive angles. Haselgrove and Tuck (1976) attach the trailing-edge of the membrane to an inextensible rope, therefore introducing adaptive aerodynamic twist combined with geometric twist. By increasing the length of the rope, static stability is improved, but lift is decreased. With consideration of nonlinear membrane elasticity, Murai and Maruyama (1982) and Jackson (1983) present the nonlinearity of lift slope as strains develop within the membrane at high incidence.

Greenhalgh et al. (1984) conduct an experimental study of an inextensible *Mylar* membrane. The results, including measurement of lift, drag and tension forces, are in good agreement with theoretical results for low angles of attack up to merely about 6 degrees where the flow is not separated. Hysteresis of lift and tension coefficients are also observed at near zero angle of attack as shown in Figure 1.7. The results also prove that the operating range of a membrane aerofoil is limited by the excess length ratio, which determines the stall due to separation at high incidence. With increasing the excess length ratio, the maximum lift increases but the operating range decreases due to earlier onset of stall. Mixed agreement between experimental results (Greenhalgh et al. 1984; Newman and Low 1984) and the theory is often associated with viscous effects.

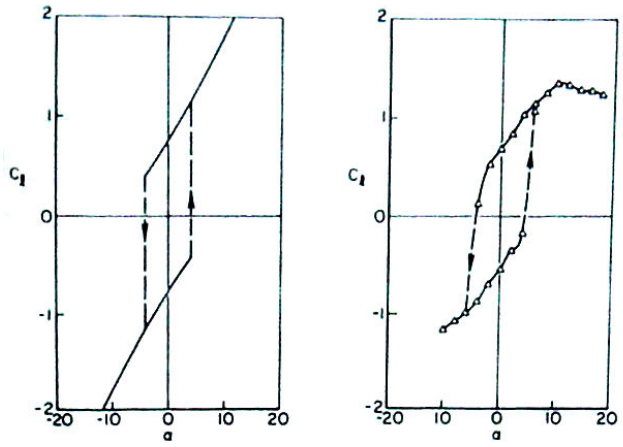

a) **b)**

Figure 1.7: Lift hysteresis of a flexible aerofoil with 1.4% excess length ratio: a) theory; b) experiment (Greenhalgh et al. 1984).

Newman (1987) summarises the aerodynamic theory of membranes based on small curved membrane equilibrium. The theory starts with an equilibrium equation as the normal boundary condition for a membrane. The equilibrium of the membrane in two-dimensional static conditions is a balance between pressure difference on either side of the membrane and the component of tension in that direction.

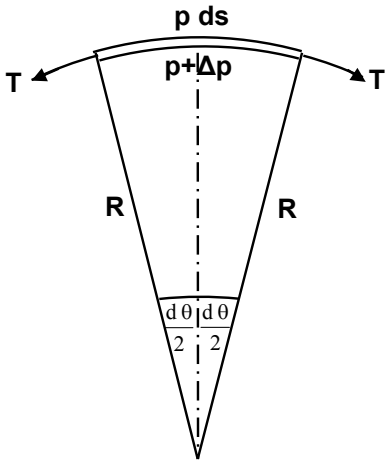

Figure 1.8: Diagram of the equilibrium of a two-dimensional inextensible membrane sail used to summarise the sail equation (Newman 1987).

Figure 1.8 shows a massless membrane with a small curve ds and angle θ at the centre of curvature with local radius of curvature R. It is subjected to dynamic pressure p on the upper side, and p+Δp at the lower side, with Tension T taken as constant along the membrane surface. The force balance in normal and tangential directions is

$$\Delta p \, ds = T d\theta \tag{3}$$

$$\Delta p = T/R \tag{4}$$

Then the classic thin aerofoil equation is used to combine with the membrane equilibrium for small camber and incidence. It is eventually shown that the tension coefficient $C_T = T/q_\infty c$ depends linearly on combined parameter $\alpha/\sqrt{\varepsilon}$. Alternatively, C_T is expected to depend linearly on $C_L/\sqrt{\varepsilon}$ (Jackson and Fiddes 1995). Newman (1987) also explains the loss of lift at the trailing-edge and the presence of leading-edge suction due to thick boundary layers and separation bubbles. In addition, Newman (1987) also examines the condition where the

membrane becomes luffing, when it begins to lose its concave form to become S shaped and finally to oscillate. Double membrane aerofoils, bluff membranes as well as three-dimensional wings and the complications are also presented in his work.

Subsequently, Jackson and Fiddes (1995) add viscous effects into a numerical model for the sail section. This is done via weak viscous-inviscid interaction of a panel method and an integral boundary layer method with a simple model of leading-edge separation bubble. The numerical model is generally in good agreement with experimental results. Nevertheless, the model can not deal with large separation and thus poor prediction of maximum lift.

Later work by Smith and Shyy studies the same problem on steady laminar flow (Smith and Shyy 1995a), unsteady laminar flow (Smith and Shyy 1995b) and turbulent flow (Smith and Shyy 1996), by using viscous flow model of a flexible membrane aerofoil. The investigation is facilitated by a set of dimensionless parameters associated with elastic strain and pretension, solving problems for steady laminar, unsteady laminar, and turbulent flow. The solutions are based on considerations that the membrane is massless and there is no time-dependent movement in the steady freestream.

According to Shyy and Smith (1995), when membrane tension is dominated by elastic strain, the equilibrium of elastic membrane restrained at the leading- and trailing-edges subjected to fluid pressure and shear stress from membrane tension T (see Figure 1.9) is presented in dimensionless form as

$$\frac{d^2x_2}{dx_1^2}\left(1+\left(\frac{dx_2}{dx_1}\right)^2\right)^{-\frac{3}{2}} = -\left(\frac{1}{\Pi_1}\right)^3 \frac{\Delta p}{T} \tag{5}$$

where

$$\Pi_1 = \left(\frac{Et}{qc}\right)^{\frac{1}{3}} \tag{6}$$

On the other hand, when membrane tension is dominated by pretension, the dimensionless equilibrium equation becomes

$$\frac{d^2x_2}{dx_1^2}\left(1+\left(\frac{dx_2}{dx_1}\right)^2\right)^{-\frac{3}{2}} = -\left(\frac{1}{\Pi_2}\right)^3 \frac{\Delta p}{T} \tag{7}$$

where

$$\Pi_2 = \left(\frac{S_0 t}{q c}\right) \tag{8}$$

The parameter Π_1 without a cube root is identical to the aeroelastic number AE proposed by Jackson and Christie (1987), which is used to express the elastic stiffness relative to the applied load. It is mentioned that "two membrane wings of different size but with the same value of AE and the same initial shape and boundary conditions will develop the same lift coefficient and strain distribution at the same angle of attack, that is, they will develop the same final shape" (Jackson and Christie 1987). An analytic solution (Seide 1977) for a pressure loaded membrane also suggests a use of cube root to define an aeroelastic parameter Π_1, which is described as the time scale ratio between the fluid and the membrane to the 3/2 power.

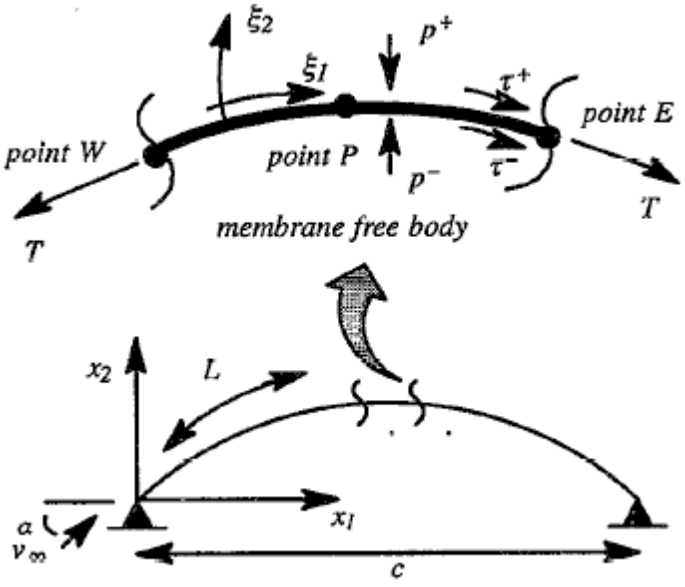

Figure 1.9: Diagram of an elastic membrane used to derive membrane equilibrium equations (Shyy and Smith 1995).

The physical meaning of these aeroelastic parameters Π_1 and Π_2 is that; in the absence of pretension, the non-dimensional deformation of an initially flat elastic membrane is inversely proportional to Π_1. Alternatively, the deformation is

inversely proportional to Π_2 (Smith and Shyy 1995b). However, by using these viscous flow models, a comparison of lift and tension with experimental data indicates that the lift is over-predicted, yet the tension is under-predicted.

These model and solution techniques are later used by Shyy et al. (1997; 1999b) to investigate the aerodynamic performance of a Clark-Y aerofoil with a membrane attached to the upper surface at low Reynolds number (10^4 - 10^5). The aerofoils are subjected to velocity fluctuation 30% in magnitude compared to the mean velocity, along the freestream direction. Their results indicate that for the membrane aerofoil, the separation zone is smaller, and the sensitivity to the fluctuations is reduced, compared to the rigid aerofoil.

Another computational study is carried out Matthews et al. (2008) to investigate viscous flow over a two-dimensional membrane. They are able to demonstrate the unsteady movements, mode shapes, and stable equilibrium shapes for different elastic stiffness. However there is the need for a fully viscous flow solver in order to accurately predict the membrane behaviour and aerodynamic forces. More recently, computations and analysis for a two-dimensional membrane aerofoil by using sixth-order Navier-Strokes solver (Gaitonde and Visbal 1998, 1999; Visbal and Gaitonde 1999) coupled with a membrane structural model developed by Smith and Shyy (1995b) are presented by Gordnier (2009). This investigation employs the same membrane aerofoil geometry as that of the experiments in Chapter 3 for membrane aerofoils with zero pre-strain. The flow is assumed to be laminar flow, at Reynolds number of Re = 2500. The results provide valuable insight into an unsteady aspect of flow-membrane interaction such as a close coupling between unsteady vortex shedding and the membrane oscillation. The coupling results in a delay in stall and enhanced lift at high angles of attack, which will be discussed next. In general, the characteristics of the membrane and its interaction with the flow agree well with the experimental results, which will be discussed later in Chapter 3.

According to the computational results by Gordnier (2009), for low incidences, the aerofoil is largely steady. The location of maximum camber moves forward and becomes more asymmetric as the incidence increases up to $\alpha = 16^o$, and moves back downstream as the angle increases further. As the angle of attack

increases, the extent of the separation bubble increases and the shear layer moves away from the membrane surface as can be seen in Figure 1.10. The vortices also form and strengthen at higher incidences, which are suggested to be interacted with the surface boundary layer.

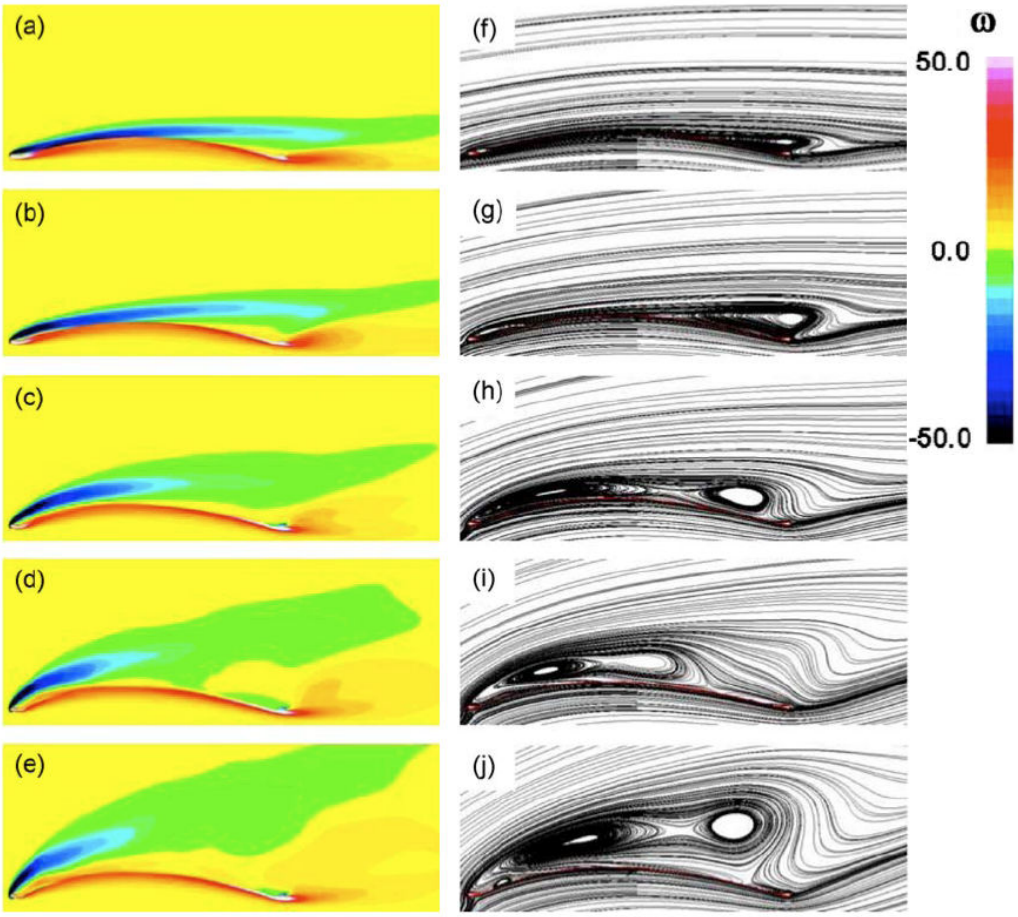

Figure 1.10: Mean vorticity and streamline patterns for a two-dimensional membrane aerofoil at various angles of attack: (a, f) α = 4°; (b, g) α = 8°; (c, h) α = 12°; (d, i) α = 16°; (e, j) α = 20°. Computational simulation by Gordnier (2009).

The spectral analysis illustrates a strong correlation between the measured structural frequencies and the vortex shedding frequency. At moderate incidence the membrane exhibits a third mode standing wave, while at high angles the second mode dominates, though the response is less regular. With increasing Reynolds number, the separation downstream is significantly reduced. The comparison between the membrane and rigid aerofoil of the same mean membrane shape in Figure 1.11 demonstrates that a separation bubble on the rigid aerofoil is larger. The more coherent vortices are found on the membrane aerofoil. Membrane vibration is seen to excite the separated shear layer, prompting earlier

roll up and a series of secondary vortices. In the same figure (c), the pressure distribution indicates a stronger suction region over the front portion of the membrane wing. The combined effects of induced camber and dynamic motion result in a delay in stall and a lift enhancement in a post-stall region as shown in Figure 1.12 (Gordnier 2009).

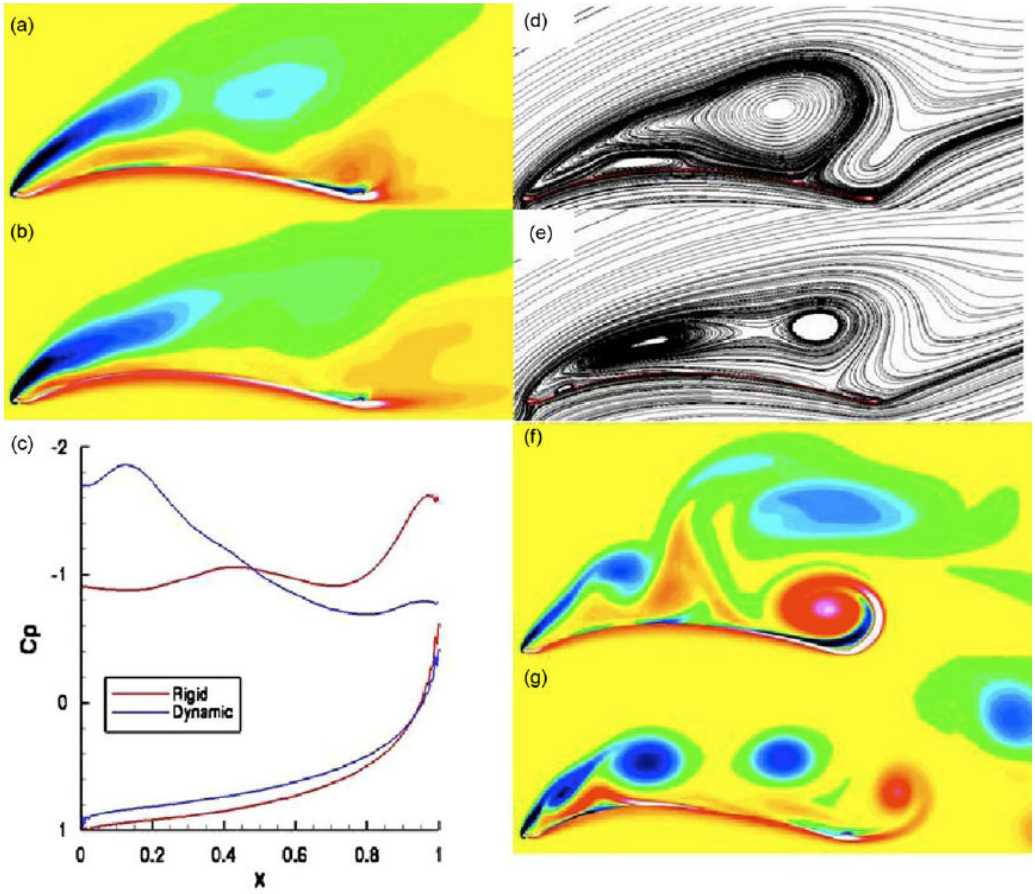

Figure 1.11: Comparison of two-dimensional rigid (a, d, f) and membrane (b, e, g) aerofoil solutions for α = 20°: (a, b) mean vorticity; (d, e) mean streamlines; (c) surface pressure coefficient; (f, g) instantaneous vorticity. Computational simulation by Gordnier (2009).

A subsequent study (Gordnier and Attar 2009) extends the previous investigation to a higher Reynolds number of 48500, where the flow is transitional/turbulent, and a pre-strain of 5%. Similarly, the results show the roll up and shedding of coherent vortical structures, which interact with the membrane causing the unsteady membrane oscillations. Again, the membrane frequencies indicate a close coupling with the unsteady flow over the aerofoil.

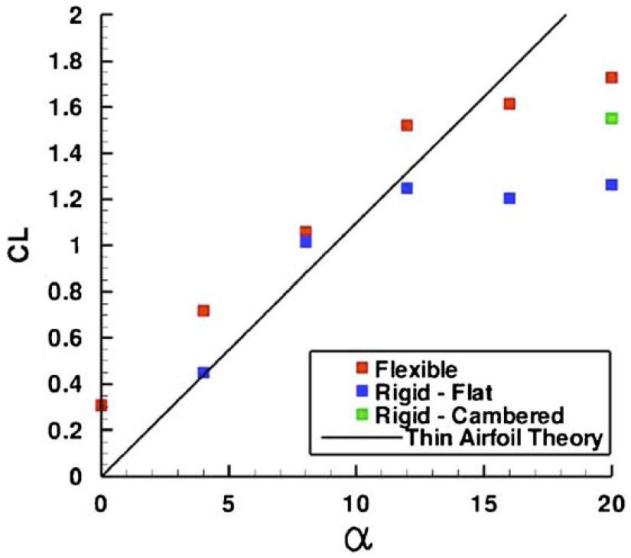

Figure 1.12: Comparison of mean lift coefficient for a membrane aerofoil, a rigid flat aerofoil and a rigid cambered aerofoil (Gordnier 2009).

1.2.3 LOW ASPECT RATIO MEMBRANE WINGS

MEMBRANE WING MAVS

The term Micro Air Vehicle (MAV) is generally referred to as a remotely controlled aircraft with a maximum dimension of approximately 6 inches (15 centimetres), a mass of 80 g (2.8 oz), and flight speed around 10 m/s (Reynolds number 10^4-10^5). The MAVs have been of interest to both military and civilian applications with missions such as reconnaissance, surveillance, communication, targeting, and smoke, chemical, or nuclear materials sensing.

The design and development of the MAVs have advanced greatly in recent years. The design considerations involve the ability to carry payloads such as camera, detection sensors, autopilots, global positioning system (GPS) navigation, and fuel or energy storage for greater range/endurance (Torres and Mueller 2004). The advantages of the MAVs include portability and storage, rapid deployment, real-time data, low radar cross-section and capability to operate inside buildings and confined spaces. The potential for low production cost is also an advantage (Mueller 1999). In general, the MAVs could be categorised into flapping wings and fixed-wings. The studies of flapping wing MAVs have recently involved the flapping mechanism of "natural flying vehicles" such as insects, bats and birds (Shyy et al. 1999a; Wootton 2000; Zbikowski 2002). Whereas the interest of the

fixed-wing MAVs has lately been drawn to flexible membrane wings, which will be focused on in this review.

The fixed wing MAVs are required to operate under a wide range of possible operational environments including urban, jungle, desert, marine, mountains and arctic environments (Mueller 1999). They must also be able to perform their missions in all weather conditions such as wind shear and gusts. Due to a low Reynolds number flight regime, the major issues of the MAVs are laminar boundary layer separation, transition, and low lift-to-drag ratio. At such low Reynolds numbers, it is difficult to avoid leading-edge separation at small incidences, and massive separation at higher incidences. Even without flow separation, the low Reynolds number aerodynamics results in low lift-to-drag ratios. In such low flight speed, small fluctuations of wind could substantially impact on the vehicle. Accordingly, no fixed wing can be expected to have steady characteristics and sustained good performance (Shyy et al. 1999a). It is therefore very challenging to design the MAVs that are able to fly when large wind gusts or an unsteady freestream is present.

The influence of the unsteadiness of the freestream on vehicle performance is of major interest. Mueller et al. (1983) presents the effects of freestream turbulence on lift and drag performance of a Lissaman7769 aerofoil. It is found that the hysteresis characteristics of the lift and drag coefficients appears at the freestream disturbance intensity of 0.10%. However the hysteresis loop disappears when the freestream turbulence intensity is increased to 0.30%. This disappearance seems to be related to the change in flow structure. They suggest that the surface roughness can also give the same result. Hysteresis of the aerodynamic behaviour such as flow separation and reattachment is also a common feature of the unsteady freestream at low Reynolds numbers (Brendel and Mueller 1988). Liu (1992) reports that, at Re = 2.5×10^5 to 4.5×10^5 and under a typical wind condition, the lift, drag, and moment fluctuate substantially with wind speed variations. For MAVs, which fly at lower Re, such fluctuation can affect aerodynamics more significantly. Particularly under gusty conditions, where atmospheric turbulence typically has root mean square levels of the order of 1 m/s near the ground. This means up to 20% variation in flight speed, assuming a flight speed of 5 m/s.

Cross-stream turbulence can cause the effective angle of attack to vary by up to 10 degrees (Gursul 2004).

As discussed earlier, separation bubbles can affect vehicle performances. However this may not be relevant to low aspect ratio wings. An experimental study by Torres and Mueller (2000) indicates that thin and low aspect ratio wings, which are typical for MAVs, may not suffer from separation bubble problems or critical stall even at very low Reynolds numbers. The lift for thin wings with aspect ratios less than 2 is highly tip vortices dominated, and is not too different from delta wings which are quite difficult to stall but susceptible to rolling instabilities (Gad-el-hak 2001).

Low aspect ratio wings with low sweep angles are often employed for MAV configurations. It is known that serious aerodynamic, stability and control issues may exist for these configurations. In most cases, laminar-transitional flows are dominant, and separation, transition and vortical flows play important roles (Gursul et al. 2005). For the next generation of small flight vehicles, the wings will be highly flexible. The coupling of unsteady, separated and vortical flows with the flexible wings may be significant. For a flexible delta wing, the study of Taylor and Gursul (2004b) reveals that the vibration of the flexible wing enhances lift. They are able to show significant lift enhancement of a flat-plate flexible delta wing ($\Lambda = 50^o$) over a rigid and a rigid curved wing in the post stall region. Vardaki et al. (2005) further investigate this phenomenon and find substantial effects on the vortical flow with increasing wing flexibility. The oscillating leading-edge excites shear layer instabilities and promotes reattachment of the separated flow, hence increasing lift.

There is growing interest in the use of membrane wings for Micro Air Vehicles because of their passive shape adaptation and aeroelastic effects of the membrane skin, which has tendency to reduce flow separation. Studies of membrane fixed-wing MAVs have been carried out intensively by a research group from the University of Florida. Examples of their membrane wing MAVs are shown in Figure 1.13. It is found that the membrane can significantly improve longitudinal static stability, provide more favourable lift to drag ratio and gust rejection, and delay stall, though a drag penalty also develops (Shyy et al. 1997; Shyy et al.

1999a; Waszak et al. 2001; Ifju et al. 2002; Lian et al. 2003b; Lian and Shyy 2005; Albertani et al. 2007; Stanford et al. 2008; Stanford and Ifju 2009). Even membrane skin with low degrees of compliance can have substantial effects on aerodynamic performance (Shyy et al. 1999a; Levin and Shyy 2001; Lian et al. 2003a).

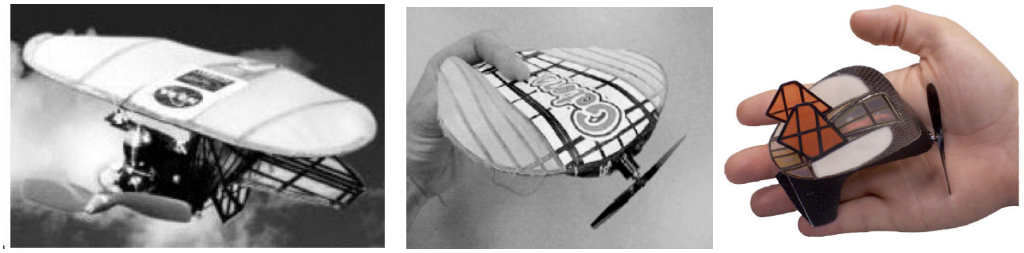

Figure 1.13: Photograph of University of Florida membrane wing MAVs.

Significant deformation of the membrane wing under load, particularly at high angles of attack is presented in the work of Waszak et al. (2001). They suggest that the deformation allows the wing to see a smaller effective angle of attack at the tips. In regard to this membrane deformation, Shyy et al. (2005) reports that the adaptation in its shape under external force has two effects. On one hand, it reduces the lift by decreasing the effective angle of attack. The decrease in the effective angle for the membrane wing is observed in numerical results by Lian et al. (2003a) and Lian and Shyy (2005). On the other hand, it increases the lift by increasing the camber. Billowed shape of the membrane wing is demonstrated by using a visual image correlation (VIC) system in the work of Albertani et al. (2007), and is validated by the numerical results of Stanford et al. (2007a; 2007b). The location of the maximum camber is seen to significantly shift aft-ward at the onset of stall. Tamai et al. (2008) are able to show that trailing-edge washout can keep the flow attached to the flexible surface up to $\alpha = 14^{o}$, while under similar conditions a rigid wing shows a very large separation.

The membrane can have self-excited vibration in even a steady freestream. However, under a gust situation the membrane fluctuation is not expected to cause a sensitive response to the vehicle (Lian et al. 2003a). This is due to the fact that the membrane fluctuates in the time scale much faster than the expected wind gust time scale, in which situation the energy is mainly located in the low frequency range (Liu 1992). An experimental study from Waszak et al. (2001) indicates that

the membrane wings exhibit self-excited vibration on the order of 100 Hz in a steady freestream. Similar observation on the same wing is also reported in a numerical study by Lian and Shyy (2003), using a hyperelastic solver and an unsteady viscous flow solver. Such vibrations and the associated shape deformation alter the pressure distribution on the membrane wing, leading to a fluid-structure interaction problem. At high incidences, numerical results from Stanford and Ifju (2009) indicate the presence of the interaction between recirculating flow and tip vortices, resulting in potential roll instabilities.

A number of studies provide evidence that membrane wings delay stall and improve vehicle performance. Figure 1.14, adopted from Waszak et al. (2001), compares the lift curves as a function of angle of attack for rigid and membrane wings, with configuration similar to that shown in the middle of Figure 1.13. It is seen that the membrane wings have smoother flight platforms and much higher stall angle (30^o to 45^o) than that of the rigid wing of similar geometry.

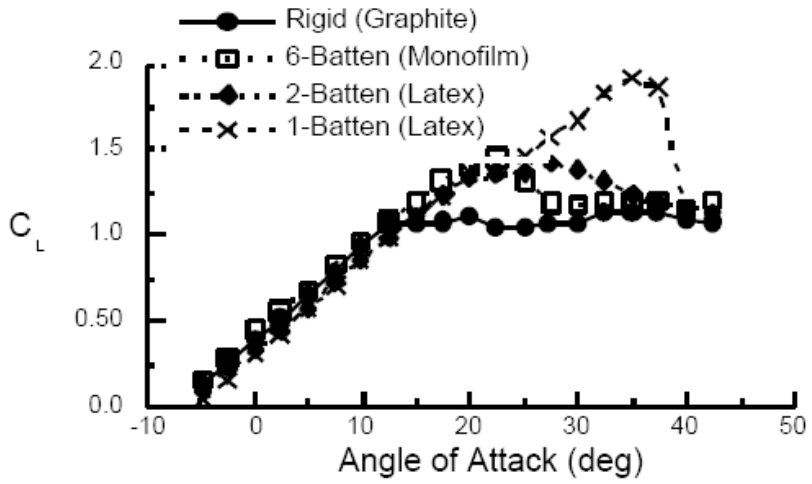

Figure 1.14: Effect of wing stiffness on lift coefficient of the same wing configuration. Experimental results by Waszak et al. (2001).

Similar observation is verified by Shyy et al. (1997). The increase in maximum value of L/D for a flexible wing is also reported in the experimental investigation of Deluca et al. (2004). Higher lift coefficients and substantially improved static longitudinal stability are also demonstrated in the study by Albertani et al. (2007). This is supported by Stanford et al. (2007a,b), whose results also show that the computed pressure distribution affects the shift of low pressure region on the upper surface towards the trailing-edge, hence increasing the nose-down pitching

moment and the static margin. However, drag is also seen to arise with increasing Reynolds numbers, whereas the opposite is true for the rigid wing. The increase in lift, drag, lift slope and L/D is once again verified in the work of Stanford et al. (2008).

MEMBRANE WINGS OF BATS

Unlike birds and insects, bat wings are thin and highly compliant (Swartz 1998) with the ability to adapt its shape to the flow, hence it can undergo substantial changes in shape and camber when experiencing external aerodynamic forces. The wings of bats and birds also differ in another aspect. Since the primary feathers of a bird's wing can be separated, air can pass through and the wing is aerodynamically inactive. Whereas bat wing membranes can be actively stretched and collapsed (Swartz et al. 1996), so they cannot be made aerodynamically inactive as easily as bird wing feathers. Figure 1.15 compares a bat wing with bird wings and a human arm.

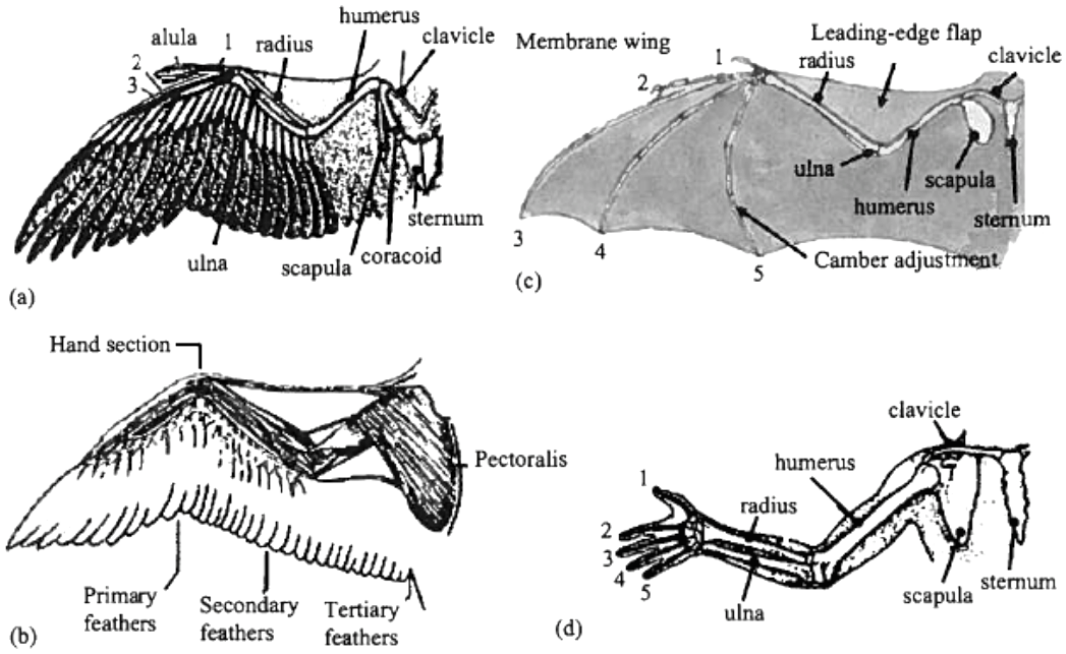

Figure 1.15: Schematics for a), b) bird wing; c) bat wing; d) human arm (Shyy et al. 2008).

A bird has a wrist and fingers, or *hand wing*, to support the weight of the primary feathers and provide strength to the wing tip (Videler 2005). On the other hand, a bat has long rib-like fingers which support the membrane covering it, and provide the ability to alter camber and tension in the membrane for lift adjustments and

dynamic control. For the bats that hunt for insects, they must have high agility, referred to as the rate at which a turn can be initiated (Norberg and Rayner 1987); and good manoeuvrability, referred to as the minimum space requiring for a turn at a given speed. During insect capture, the bats often perform rapid turns, rolls, dives and climbs, whereas nectar feeder type must fly slowly and hover close among vegetation. The wing's flexibility allows the animals to make a 180-degree turns in a distance of less than half a wingspan. Some bat species commute over substantial distance; hence they must be capable of sustained steady flight. These astonishing flight performances of bats can be attributed to their exceptional membrane wing structure (see Figure 1.16), which has recently been a novel inspiration for air vehicle designs.

Figure 1.16: Membrane wings on bat. Photo by T. Beth Kinsey, Tucson, Arizona, America (http://fireflyforest.net/firefly).

Norberg and Rayner (1987) study intensively the classification of bat flight morphology in relation to flight performance and flight behaviour over a range of bat families and feeding classes. Correlations between wing dimensions and body mass are presented in their paper. Wing size and wing shape are interpreted as being equivalent to wing loading and aspect ratio. Relative length and area of wingtip are used to derive a wingtip shape index, which measures the degree of

roundedness of the wingtip. Their approach of identifying correlations of bat flight behaviour and morphological adaptations clarifies the eco-morphological relationships of bats. The more recent study of bat wing structure is carried out by Swartz et al. (2007). They explore the dynamic anatomy of the bat wing in flight. Wing beat cycles with relation to peaks in wing amplitudes are presented as well as differences in skin stretch in spanwise and chordwise direction. Riskin et al. (2008) study the wing beat kinematics which is found to be very complex. A vortex wake pattern behind the wing is investigated in the flapping flight of bats as an aerodynamic footprint by Hedenström et al. (2007). The wakes are found to be meaningfully different from those of birds. Also, leading-edge vortices, once thought to be irrelevant to bat flights, are detected during a slow forward flight of bats (Muijres et al. 2008). The vorticity field and velocity vectors around the bat wing are shown in Figure 1.17. Most recently, Hubel et al. (2009) are able to capture detailed wing kinematics simultaneously with wake structure over multiple wing beat cycles for the medium sized bat *Cynopterus brachyotis*. Nevertheless, how the development and evolution of wake structure link to the dynamically adaptive shape of the wing is still unknown.

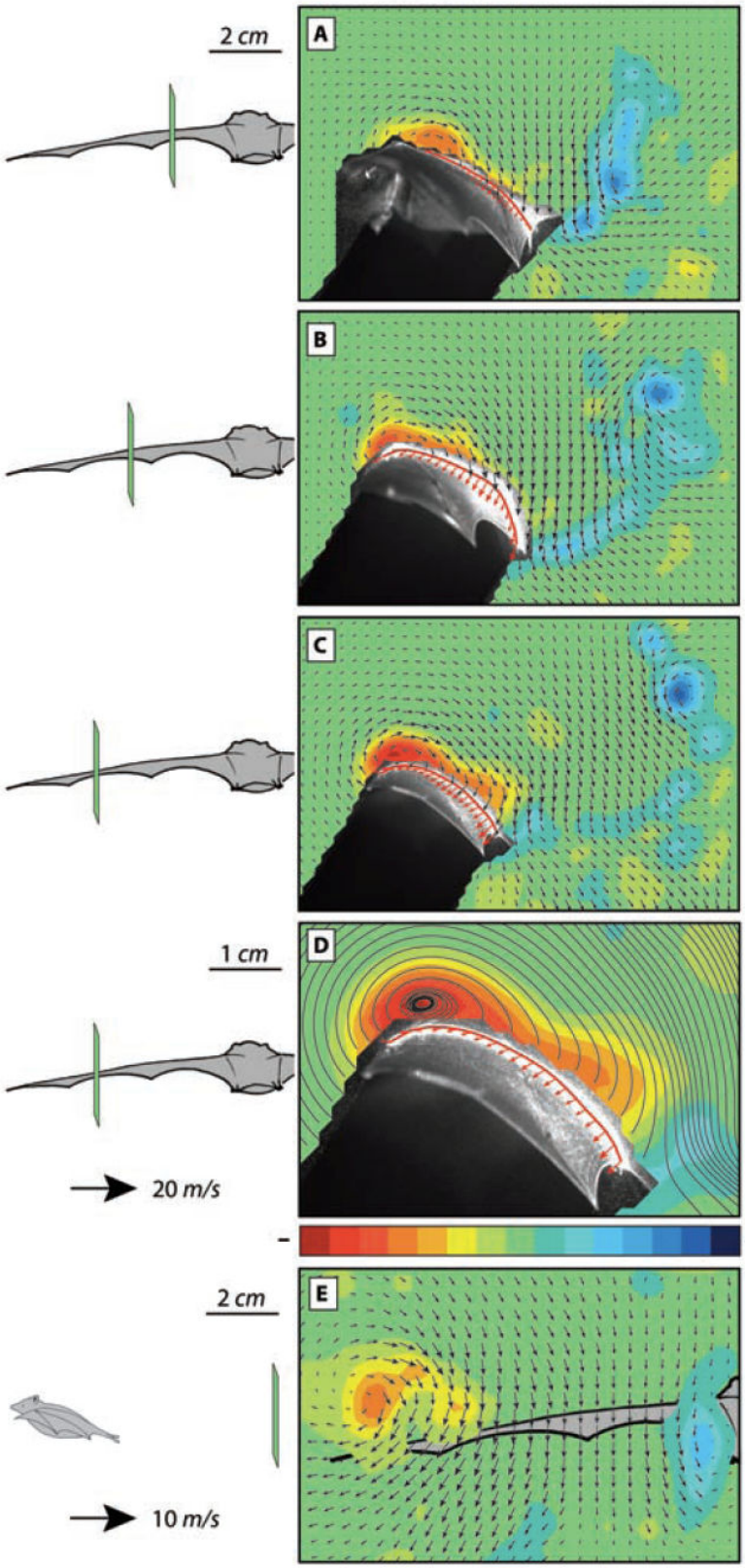

Figure 1.17: **Velocity and vorticity fields around a bat wing in slow forward flight (1 m/s) when the wing is in a down stoke. The study of leading-edge vortex in bats by Muijres et al. (2008).**

In an effort to understand the aerodynamic effects of membrane compliancy on bat flights, Galvao et al. (2006) conducts an experimental study in a wind tunnel on a low aspect ratio (AR = 0.92) membrane wing by using photogrammetric technique to measure the membrane displacement. Their wing is made from latex, with the wing's inner edge clamped fixed to the post, and the wing tip left free as shown in Figure 1.18, therefore the flows are highly three-dimensional, and tip vortices are expected to have strong effects on unsteady vibrations. (The same rig is later adopted by the same research group, with varying wing aspect ratios, which will be discussed next).

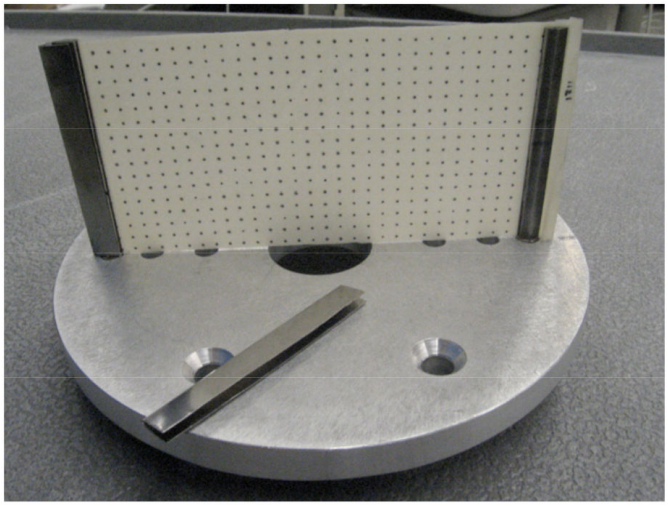

Figure 1.18: Membrane wing model used by the research team from Brown University (Galvao et al. 2006).

They report the presence of standing waves with large mode number (see Figure 1.19-a), and steep lift slopes due to adaptive cambering in response to the aerodynamic loads. Higher power efficiency values ($C_L^{3/2} / C_D$) of the compliant wing than those of a rigid wing at high angles of attack ($\alpha = 35^o$ to 40^o), as well as smoother stall are also illustrated in their work. The latter is suggested due to the decambering of the wing at high incidences where the pressure over the upper surface increases because of flow separation. On one hand this effect delays stall and on the other hand, the cost of this delayed stall is a rise in drag. For the unsteady behaviour, the membrane oscillations are suggested to be forced by leading-edge vortex shedding. At certain velocities, a resonance between the two is believed to cause large membrane vibrations.

In a subsequent study by Song and Breuer (2007), similar vibrational modes are presented for a rectangular wing with aspect ratio of AR = 0.69 as shown in Figure 1.19-b. Higher order modes, which are believed to be a result of resonance between the membrane and flow structures, are observed at the range of angles of attack near the stall region. They report a decrease in camber slope with increasing Reynolds number. In addition, the magnitude of membrane vibrations in the inboard region is reduced as the aspect ratio is increased. This is not surprising because as the aspect ratio is increased, the region of potential lift is increased whereas the region of vortex lift is decreased.

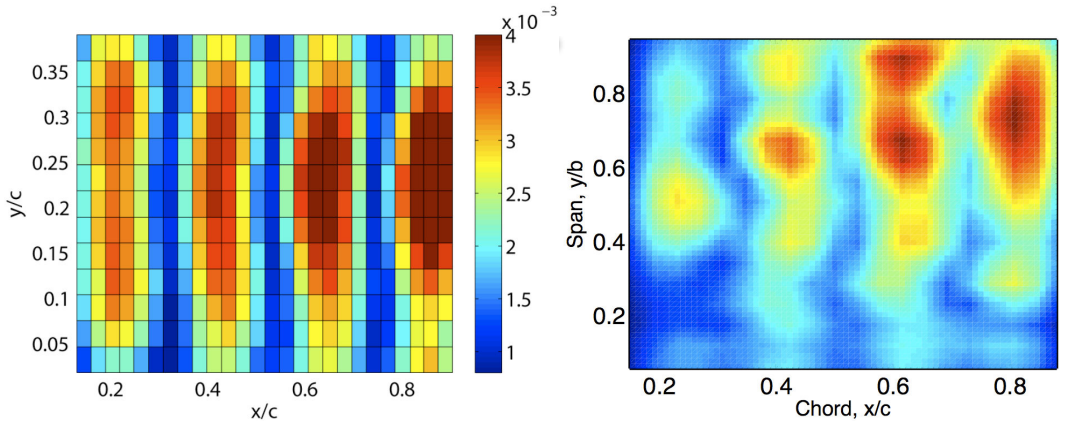

Figure 1.19: Spatial structure of the membrane oscillations showing 4th structural mode. a) AR = 0.46 (Galvao et al. 2006); b) AR = 0.69 (Song and Breuer 2007).

Further, force measurements are presented together with the deformation data by Song et al (2008a,b) for the wings with varying aspect ratio AR = 0.9, 1.4 and 1.8 membrane thickness. Their result shows that, in comparison with rigid wings, compliant wings have higher lift slope and higher drag, as well as delay stall to higher angles of attack, as shown in Figure 1.20. The wings with higher aspect ratio indicate the higher lift slope. They are able to demonstrate a strong hysteresis at around a zero angle of attack (as shown in Figure 1.21) and at the stall angle. The results identify membrane vibrations with spatial structure that are closely related to the free eigenmodes of the membrane under tension. Additionally, the vibration frequencies coincide with the calculated natural frequency of the membrane with higher harmonics, and increase with the freestream velocity. For these low aspect ratio (LAR) wings, the flow is highly three-dimensional and tip vortices are dominant. It is possible that the membrane vibrations can excite the

separated shear layer forming the tip vortices and promote reattachment (Gursul et al. 2005). For a flexible nonslender delta wing as mentioned earlier, this mechanism delays the stall and increases the lift (Taylor et al. 2007).

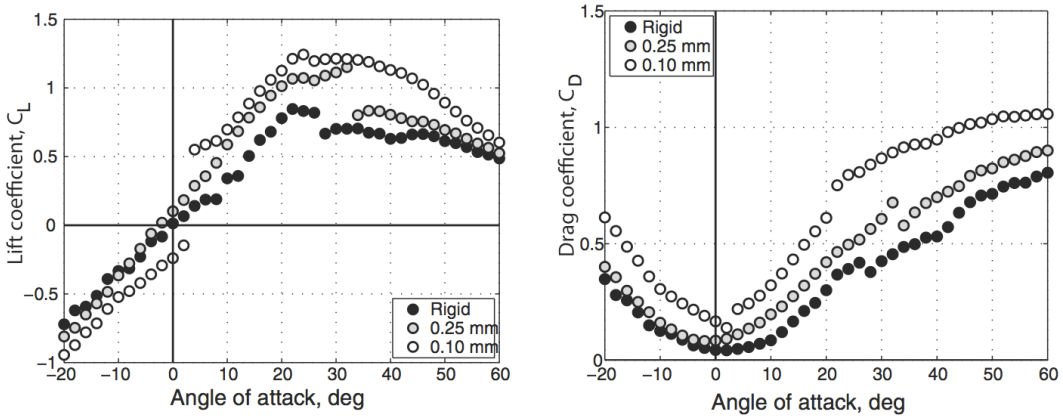

Figure 1.20: Lift (left) and drag (right) coefficient of rigid and membrane wings of AR = 1.4 and Re = 140,000 (Song et al. 2008b).

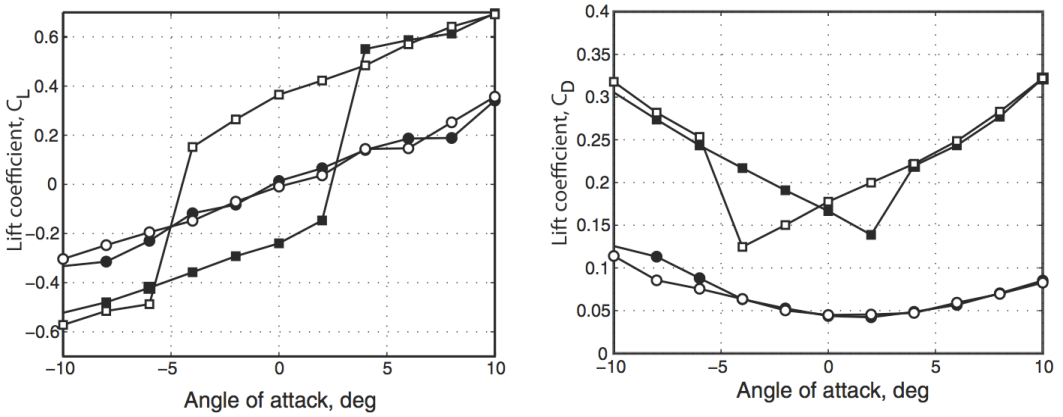

Figure 1.21: Hysteresis in lift (left) and drag (right) of membrane wing near $\alpha = 0^o$ for AR = 1.4 and Re = 140,000. Square and circle symbols represent membrane and rigid wings, respectively (Song et al. 2008b).

1.2.4 NATURAL FREQUENCY OF MEMBRANES

Assuming that a thin membrane is stretched uniformly in all directions, and vibrates transversely with small displacement amplitudes, the natural frequency of the membrane can be determined. According to the theory from *Fundamentals of Acoustics* by Kinsler et al. (1982), the elemental area of the membrane will be pulled apart with a force T dl. In Cartesian coordinates, the forces acting on a displaced surface element of area dS = dx dy is the sum of the transverse forces acting on the edges parallel to the x and y axes as shown in Figure 1.22.

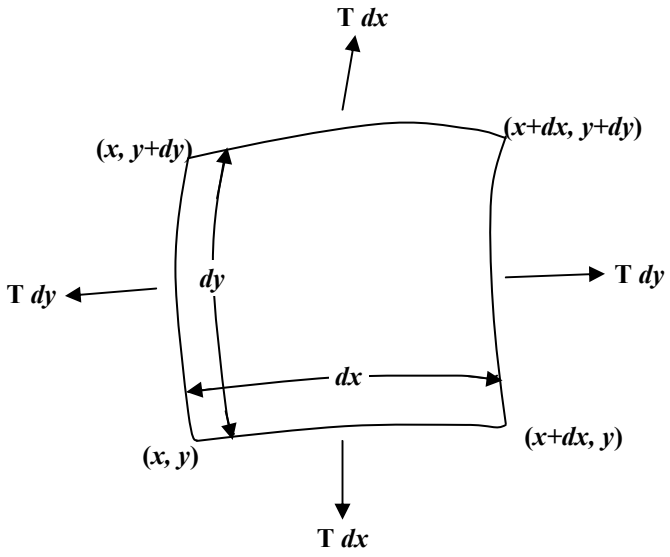

Figure 1.22: Elemental area of a membrane showing the forces acting when the membrane is displaced transversely. The diagram used by Kinsler et al. (1982) to derive the natural frequency of the membrane

By equating the sum of vertical force from two pairs of tension T dx and T dy to the product of the mass of the element ρ_s dx dy and its acceleration $\partial^2 z/\partial t^2$ gives

$$\frac{\partial^2 z}{\partial x^2} + \frac{\partial^2 z}{\partial y^2} = \frac{\rho_s}{T}\frac{\partial^2 z}{\partial t^2} \tag{9}$$

which is the two-dimensional wave equation. To calculate normal modes on membranes, the solutions to (9) can be assumed to have a form

$$z = \quad e^{jwt} \tag{10}$$

where Ψ is function of position. The Helmholtz equation is obtained from substitution and identification of

$$k = \omega\left(\frac{\rho_s}{T}\right)^{1/2} \tag{11}$$

The boundary conditions for a stretched rectangular membrane fixed at x = 0, x = L_x, y = 0, and y = L_y are

$$z(0, y, t) = z(L_x, y, t) = z(x, 0, t) = z(x, L_y, t) = 0 \tag{12}$$

Assuming a solution

$$z(x,y,t) = \quad (x,y)e^{jwt} \tag{13}$$

to (9), hence

$$\frac{\partial^2\Psi}{\partial x^2}+\frac{\partial^2\Psi}{\partial y^2}+k^2\Psi=0 \tag{14}$$

Assuming that Ψ is the product of two functions, each depends on only one of the dimensions

$$\Psi(x,y)=X(x)Y(y) \tag{15}$$

hence

$$\frac{1}{X}\frac{\partial^2 X}{\partial x^2}+\frac{1}{Y}\frac{\partial^2 Y}{\partial y^2}+k^2=0 \tag{16}$$

To sum the three terms to zero for all x and y, the first term and the second term must be constants because the first term is a function only of x and the second term only of y. This provides two following equations

$$\frac{\partial^2 X}{\partial x^2}+k_x^2X=0 \quad \text{and} \quad \frac{\partial^2 Y}{\partial y^2}+k_y^2Y=0 \tag{17}$$

where the constants k_x and k_y are related by

$$k_x^2+k_y^2=k^2 \tag{18}$$

Solutions of (17) are sinusoids, so that

$$y(x,y,t)=A\sin(k_x x+\phi_x)\sin(k_y y+\phi_y)e^{j\omega t} \tag{19}$$

where k_x, k_y, $\emptyset_x$, and $\emptyset_y$ are determined by the boundary conditions. The boundary conditions z(0, y, t) = 0 and z(x, 0, t) = 0 require $\emptyset_x = 0$ and $\emptyset_y = 0$. The conditions $z(L_x, y, t) = 0$ and $z(x, L_y, t) = 0$ require the arguements k_xL_x and k_yL_y to be integral multiples of π. Therefore the standing waves on the membrane are given by

$$\begin{aligned} &z(x,y,t)=A\sin k_x x\ \sin k_y y e^{j\omega t} \\ &k_x=n\pi/L_x \qquad n=1,2,3,... \\ &k_y=m\pi/L_y \qquad m=1,2,3,... \end{aligned} \tag{20}$$

where $|A|$ is the maximum displacement amplitude. The wave numbers k_x and k_y are limited to discrete sets of values, which confine the natural frequencies for the allowed modes to

$$f_{nm} = \omega_{nm} / 2\pi = \frac{1}{2}\left[\frac{T}{\rho_s}\left(\left(n/L_x\right)^2 + \left(m/L_y\right)^2\right)\right]^{1/2} \quad (21)$$

Equation (21) is the natural frequency of a rectangular membrane with all four sides fixed. For the membrane with two sides free and the infinite two sides fixed, the natural frequency can be found by changing the boundary conditions and adding free edges, giving

$$f_{1,l} = \frac{1}{2}\left(\frac{T}{\rho_s L^2}\right)^{1/2} \quad (22)$$

That is

$$f_0 = \frac{1}{2L}\left(\frac{E\,\delta}{\rho_m}\right)^{1/2} \quad (23)$$

Equation 23 could be employed to calculate the natural frequencies with the first mode of the two-dimensional membrane aerofoil in the present study, where L is substituted by the chord length of the membrane. However, it should be noted that the above theory does not take into account the existence of the nonlinear nature of fluid-structure interaction. This will be discussed more in Chapter 3 (3.4) and Chapter 4 (4.4).

1.3 OBJECTIVES

The aim of this research is to expand on the knowledge of aerodynamic characteristics of flexible membranes, through a sequence of experimental investigations. The existing studies have already proven that membrane wings have advantages of delaying stall, enhancing lift and improving vehicle performance. However, important aerodynamic details such as flow-membrane interaction behind those astonishing features are absent from the literature. The main aim of the present research is therefore to focus on the unsteady aspects of the fluid-structure interaction.

As mentioned earlier, separation, unsteadiness and low lift-to-drag ratio are major problems in low Reynolds number aerodynamics. Yet, the characteristics of the membrane that help alleviate such issues are still largely unexplored. With this in mind, one of the objectives of this work is to understand the characteristics of the

membrane deformation and the flow field at varying angles of attack and freestream velocities. By varying the freestream velocities, not only the effect of Reynolds number but also the effect of membrane flexibility can be learned. In addition, since the membrane is known to develop self-induced vibrations, the study aims to gain better understanding of such membrane oscillations, including the vibrational modes and the oscillation frequency. Relation between the membrane vibration and flow instabilities is another aspect of this investigation. Another aspect that remains to be explored is the effect of membrane pre-strain and excess length. The difference in the pre-strain and excess length values alters the membrane tension and the adaptive camber, thus affects the aerodynamic performance. An additional aim of this work is to better understand the influence of tip and leading-edge vortices on the flow-membrane interaction for low aspect ratio (rectangular and delta) wings. The comparison to the rigid wing should clarify the role of flexibility in the enhanced lift and delayed stall.

It is known that high manoeuvrability and agility are desired for MAV applications, and these have increased the interest in the use of membrane wings. Understanding of the passive flow control mechanisms using the flexible membranes is therefore of paramount importance. The findings should ultimately provide valuable insight into the improvement of manoeuvrability and efficiency of the aerial vehicles beyond present limitations.

CHAPTER 2: EXPERIMENTAL APPARATUS AND PROCEDURES

2.1 INTRODUCTION

This Chapter deals with experimental apparatus and data procedures employed for the completion of a three-year research project on the aerodynamics of flexible membranes. The description of the test facility is given, followed by the details of experimental set-up, models used, instrumentation employed as well as methodology utilised for the analysis of the results obtained from each measurement.

2.2 OPEN JET WIND TUNNEL FACILITY

All experiments were conducted in an open-jet wind tunnel facility, located in the Department of Mechanical Engineering, at the University of Bath. The tunnel has a circular working section of 760 millimetres in diameter, and 1 metre long. The open working section allows easy accessibility for the placement of models, and the use of diverse instrumentation systems as well as flow visualisation. A large fan powered by an electric motor enables the tunnel to achieve a maximum speed of approximately 30 metres per second, with a freestream turbulence level of 0.1% when run at the velocity range of the current experiments. The tunnel velocity was measured by a pitot-static tube connected to a Digitron 2020P manometer, with an accuracy of 2% of the typical values measured.

2.3 EXPERIMENTAL SET-UP AND MODELS

Models tested were two-dimensional membrane aerofoils and low aspect ratio membrane wings. The experiments were complemented with a comparative rigid aerofoil and a rigid wing with similar geometries to those of the membrane ones. A two-dimensional membrane aerofoil with zero pre-strain was firstly tested, followed by membrane aerofoils with pre-strain and excess length. Then low aspect ratio membrane wings including rectangular and delta wings were investigated. This section explains the properties of membrane material, the details of experimental set-up, as well as the thorough description of each model.

MEMBRANE MATERIAL

A membrane used for two-dimensional membrane aerofoils and low aspect ratio membrane wings was made from a black latex rubber sheet with a thickness of t = 0.2 mm, Young's modulus (sometimes called elastic modulus or modulus of elasticity) of E = 2.2 MPa, and density of ρ_m = 1 g/cm^3. The membrane's modulus of elasticity was measured by subjecting the membrane to known tension and measuring the strain with a high resolution digital camera (the variation of tension and strain is shown in Figure 2.1).

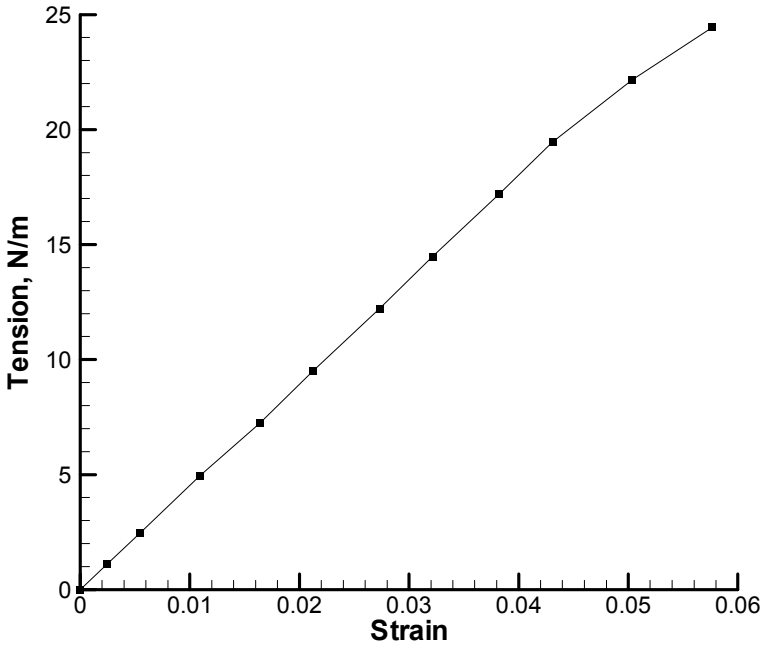

Figure 2.1: Variation of tension and strain of the membrane.

In these experiments, the strain was varied up to 6% and both the new and used membranes were tested. It was found that the tension-strain relation is linear in this range. Since the material has a smooth finish on both sides, it is assumed that flow disturbance from surface roughness is negligible. Additional properties of the membrane material are shown in Table 2.1.

Chemical name	**cispolyisoprene**
Mechanical property:	
Resilience	very good
Tensile strength	21 - 25 MPa
Elongation	750 – 850 %
Tear resistance	very good
Hardness	35-50^{o} shore micro
Thermal characteristic:	
Heat ageing resistance	good
Minimum recommended operating temperature	40^{o}c
Maximum recommended operating temperature	70^{o}c
Flame resistance	poor
Environmental resistance:	
Weather	fair
Ozone	unsuitable
U.V. light	poor
Water	very good
Dilute Acid	good
Dilute Alkali	fair
Petrol, oils, greases, degreasing solvents	unsuitable

Table 2.1: Properties of latex rubber membrane (Four D Latex Rubber™).

EXPERIMENTAL SET-UP

An experimental set-up used to support the models for the entire experimental cases is shown in Figure 2.2. The support frames as well as the circular end plates were made of Perspex® with a thickness of 10 mm. Two edges of the support frames in the upstream direction were sharpened to provide arcs in an effort to maintain a uniform air velocity and reduce flow disturbance. The transparent Perspex® allowed access of membrane and flow visualisation. The circular plates were used to adjust the angle of attack, and the distance between the two end plates was 450 mm. The uncertainty in the angle of attack was determined to be of the order of ±0.5 deg for most test cases. The whole set-up was placed in the open-section of the wind tunnel. The magnitude of blockage factor varied depending on the size of the model and the angle of attack. For the extreme case at

the largest angle of attack, the largest blockage factor was found to be approximately 7.5%.

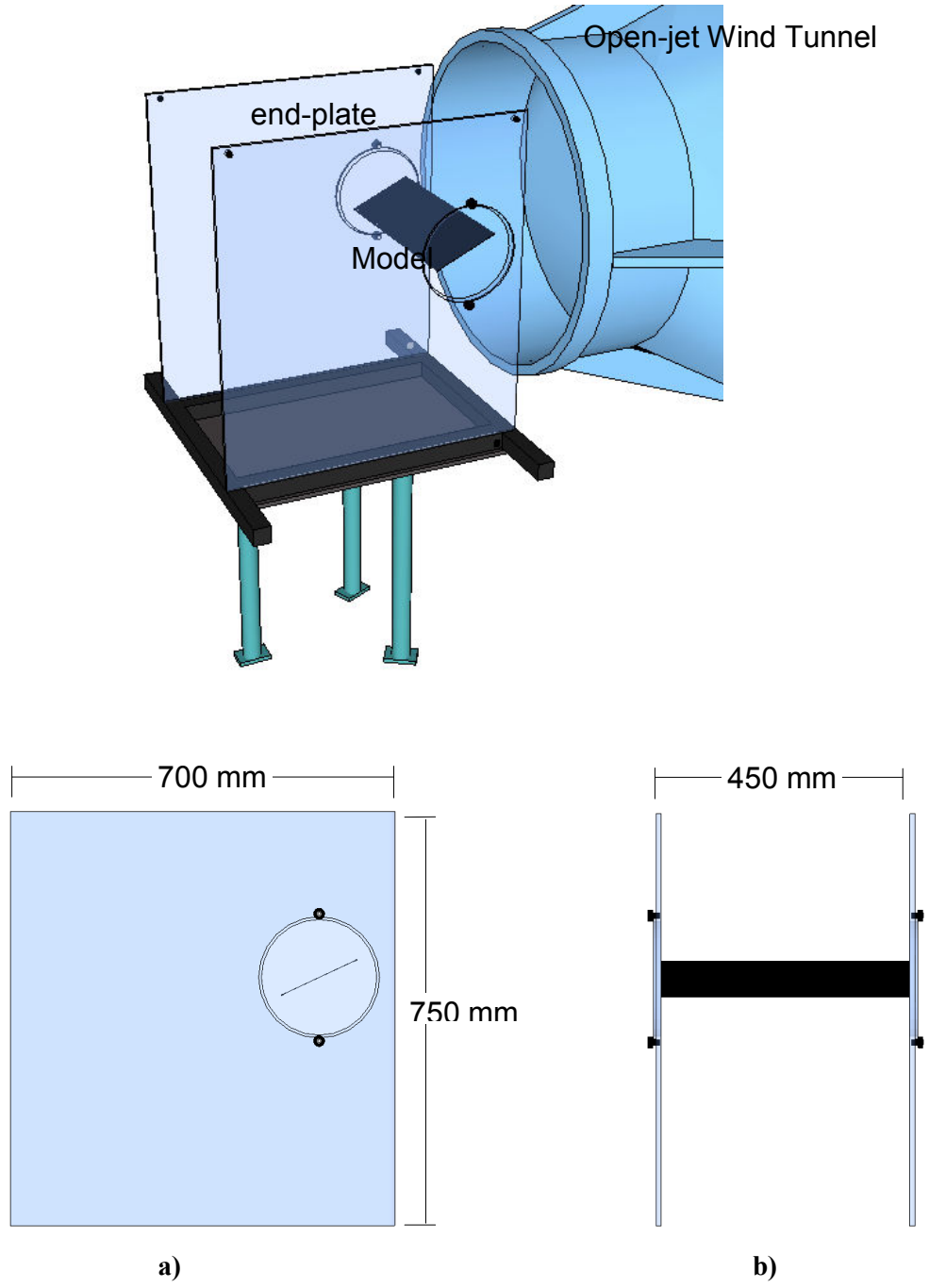

Figure 2.2: **Schematic of the experimental set-up with: a) side-view; b) front-view. The model in black colour represents a two-dimensional membrane aerofoil.**

TWO-DIMENSIONAL MEMBRANE AEROFOIL

For a two-dimensional membrane aerofoil, the membrane was attached to the aerofoil-shaped leading- and trailing-edges. A streamwise cross-section of the aerofoil and its dimensions are shown in Figure 2.3-a, with the details of the rigid support used as the leading- and trailing- edges shown in Figure 2.3-b. The rigid leading- and trailing-edges were made from stainless steel, and were designed with consideration that they must be strong enough to resist bending but small enough to produce a thin aerofoil cross-section. The rigid leading- and trailing-edges run along the whole span of the test section between the two end plates with a small gap (1 mm) between the membrane and the end plates. The main feature of this setup was that the membrane deformation was essentially two-dimensional. The aerofoil had a span of 450 mm and chord length of c = 150 mm, resulting in an effective chord length of the membrane (defined as the distance between the inner edges of the rigid leading-edge and trailing-edge) of c_e = 137 mm.

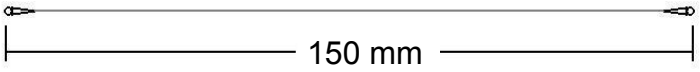

a)

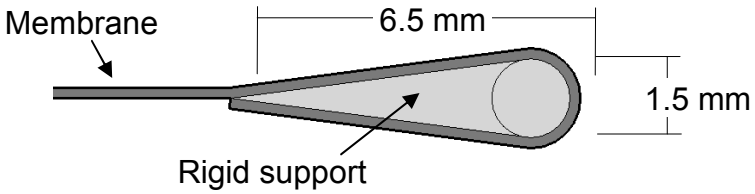

b)

Figure 2.3: a) Cross-section of the two-dimensional membrane aerofoil; b) details of the rigid support used as the leading- and trailing-edges of the membrane aerofoil (showing when it is wrapped by the membrane).

The first investigation started with the membrane aerofoil without presence of an initial stain or excess length, referred to as a two-dimensional membrane aerofoil with zero pre-strain (δ_0 = 0%). To manufacture this aerofoil, no tension was

applied when attaching the membrane to the rigid leading- and trailing-edges. Before attaching, the length equal to the effective chord length was marked on the membrane. Then the membrane was glued to the leading- and trailing-edges, with the mark attaching to the inner edges of both TE and LE. There was a margin of the membrane length which wrapped around the leading- and trailing-edges (see Figure 2.3-b)

The next study involved the investigation of the effect of pre-strain and excess length ratio on the two-dimensional membrane aerofoil. The pre-strain is a dimensionless parameter describing an initial deformation of the membrane which is stretched uniformly in a chordwise direction before it is subject to aerodynamic loads. The pre-strain is expressed as a percentage of the membrane length that is stretched. To manufacture the two-dimensional membrane aerofoil with pre-strain (δ_0 = 2.5% and 5%), the membrane length that was 2.5% and 5% shorter than the effective chord length (i.e. $L_0 = 0.975c_e$ and $0.95c_e$), was marked on the membrane before it was attached to the inner edges of the leading- and trailing-edges.

The definition of excess length ratio can simply be thought of as a membrane aerofoil with initial camber. The excess length is a dimensionless parameter describing the added membrane length given to an effective chord length normalised by the effective chord length, defined as: $\varepsilon = (L_0 - c_e)/c_e$. Similar to the other membrane aerofoils, the membrane length that was 2.5% and 5% longer than the effective chord length ($L_0 = 1.025c_e$ and $1.05c_e$, giving ε = 2.5% and 5%, respectively), was marked on the membrane before it was attached to the inner edges of the leading- and trailing-edges.

The uncertainty in manufacturing the two-dimensional membrane aerofoil involved measuring the length of the membrane and the tension applied when attaching the membrane. It is estimated as $\Delta\delta_0 = \Delta\varepsilon = 0.5\%$.

RIGID AEROFOIL

A rigid aerofoil was a cambered-plate manufactured in an effort to make a comparison with the two-dimensional membrane aerofoil. It was made of stainless steel with a thickness of 1 mm, and with a profile matching that of the average

(over incidences) shape of the membrane aerofoil with zero pre-strain at 5m/s freestream velocity and at angles of attack from 10 to 18 degrees as shown in Figure 2.4-a. The leading-edge and trailing-edge of the rigid aerofoil were rounded to create a similar shape to that of the membrane aerofoil. The cross-section of the rigid aerofoil resembling that of the membrane aerofoil is shown in Figure 2.4-b.

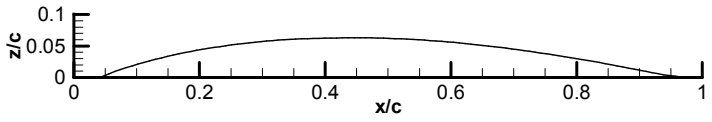

a)

b)

Figure 2.4: a) Averaged shape of the membrane aerofoil at U_∞ = 5 m/s from α = 10° to 18°; b) Cross-section of the rigid aerofoil, for which the profile resembling that of the averaged shape of the membrane aerofoil.

RECTANGULAR MEMBRANE WING

The rectangular membrane wing was composed of a rectangular rigid frame and an attached membrane as shown in Figure 2.5. The wing had an aspect ratio of AR = 2, and a chord length of c = 68.75 mm. The rigid frame was made from stainless steel with a thickness of 2 mm and a width of 5 mm, manufactured to have an aerofoil-shaped cross-section with the sharp edge pointing inwards as shown in Figure 2.6. The wing with its support was attached to a rod, which was attached to two circular plates and end plates.

DELTA MEMBRANE WING

Similar to the rectangular membrane wing, the delta membrane wing was composed of a rigid frame and an attached membrane as shown in Figure 2.7. The delta wing had a sweep angle of $\Lambda = 50^o$, and a chord length of c = 82.83 mm. The rigid frame was made from stainless steel with a thickness of 1 mm and a width of

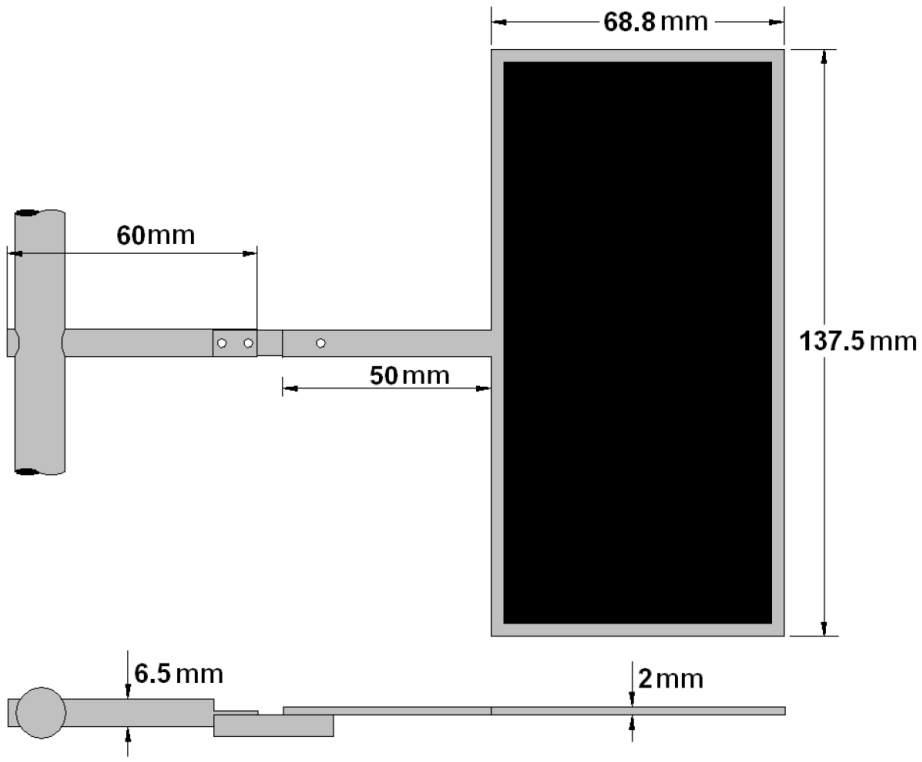

Figure 2.5: **Schematic of the rectangular membrane wing. Black colour represents a membrane and grey colour represents the rigid frame attached to the support.**

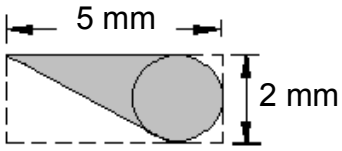

Figure 2.6: **Cross-section of the leading- and trailing-edges of the rectangular membrane wing (the sharp edge pointing inwards).**

3 mm, manufactured to have an aerofoil-shaped cross-section with the sharp edge pointing inwards as shown in Figure 2.8. Likewise, the wing with its support was attached to a rod, which was attached to two circular plates and end plates.

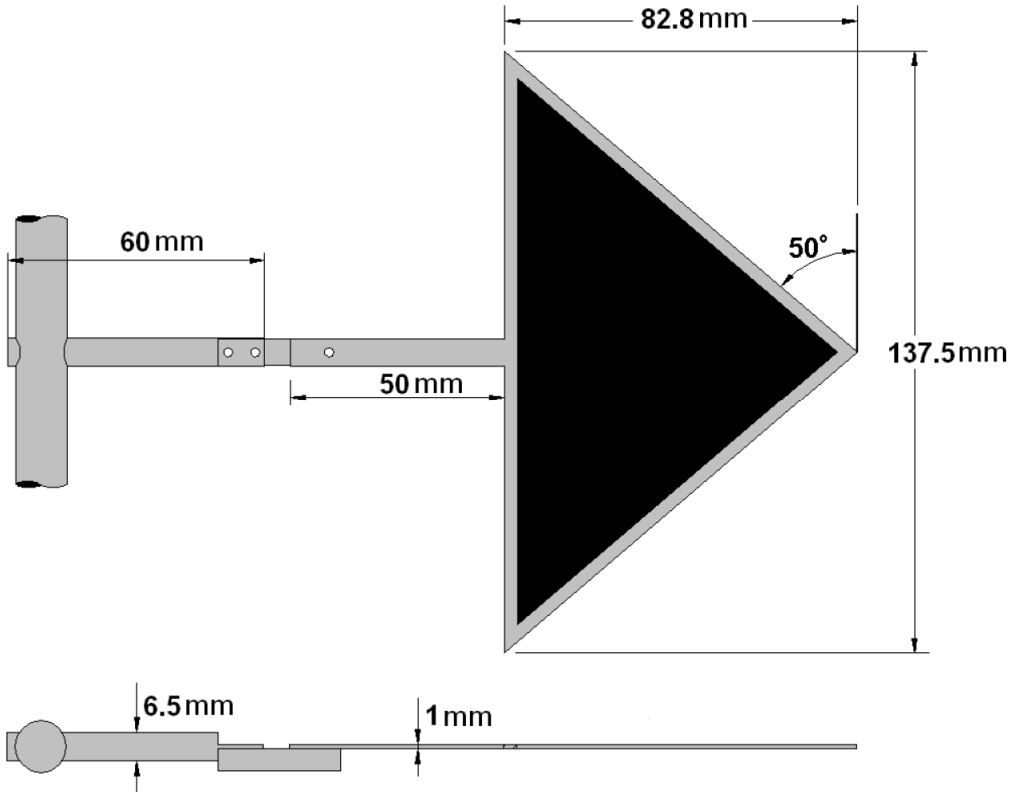

Figure 2.7: **Schematic of the delta membrane wing. Black colour represents a membrane and grey colour represents the rigid frame attached to the support.**

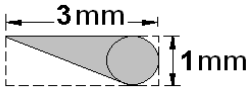

Figure 2.8: **Cross-section of the leading- and trailing-edges of the delta membrane wings (the sharp edge pointing inwards).**

RIGID WING

Two rigid wings were manufactured in an effort to make a comparison with both rectangular and delta membrane wings. The rigid flat-plate wings were made of 1 mm thick stainless steel with the leading- and trailing- edges rounded and with profiles matching those of the membrane wings.

2.4 INSTRUMENTATION AND PROCEDURES

Experiments were conducted over a range of freestream velocities and angles of attack. Shape visualisation, hot-wire measurement, Digital Particle Image Velocimetry (DPIV), smoke visualisation, Digital Image Correlation (DIC) and force measurement were utilised for the completion of this research project. This section describes the technique used, the instrumentation employed as well as a detailed analysis for each measurement.

2.4.1 SHAPE VISUALISATION

PROCEDURE

Shape visualisation technique was employed to investigate the membrane deformation for the two-dimensional membrane aerofoils. In order to measure the membrane shape, a thin laser sheet from a 4W Argon-Ion laser was used to illuminate the membrane upper surface in the streamwise plane at the mid-span of the wing. A high speed camera (Photron FASTCAM APX) was positioned normal to the flow and images were captured at a rate of f_s = 1500 frames per second. The resulting image appeared as a white curve, an example of which is shown in Figure 2.9. The images with 1024x1024 pixel resolution in TIF format were obtained over 2 seconds, resulting in 3000 images per each degree angle of attack for each freestream velocity. Finally, the images were digitised by using MatLab and Image Processing Toolbox to find the coordinates.

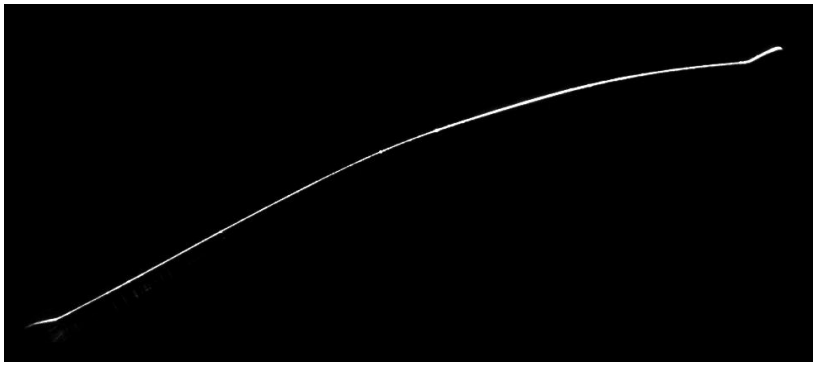

Figure 2.9: An example of the membrane shape obtained from laser sheet visualisation: δ_0 = 0%, U_∞ = 5 m/s, α = 20°. Flow is from *right* to *left*.

This technique can only detect the chordwise modes. The membrane deformation appeared uniform in the spanwise direction in visual inspections. In the preliminary experiments, the time-averaged deformation was measured near the

tip region (near the end plates) and the difference was found to be less than 10% of the values at the mid-span plane. Although the time-averaged deformation is nearly uniform in the spanwise direction, this does not rule out possible existence of the spanwise modes, which may be present due to the end effects (particularly when higher streamwise modes are observed). However, the spanwise modes cannot be detected with the present technique. The uncertainty of the measurements of the membrane displacement with the present technique is estimated to be as $\Delta z/c = 0.1\%$.

From the instantaneous coordinates of the membrane, the time-averaged membrane shape was calculated for each angle of attack and freestream velocity. In addition, the standard deviation of the membrane displacement was calculated as a function of the chordwise distance, which would easily indicate the mode of vibrations. From the digitised membrane shapes as a function of time, it was also possible to study the time history of the displacement. From the time history of the displacement sampling at the point of maximum standard deviation, the dominant frequencies were found by power spectral analysis using Fast Fourier Transform (FFT) method in MatLab. The calculations made from shape visualisation were computed in Microsoft Excel (Windows), MatLab (The Mathworks Inc.) and Tecplot v9.0 and v10.0 (Amtec Engineering Inc.) software, where all the graphics were plotted using Tecplot v9.0, v10.0 software.

DATA ANALYSIS

A) TIME-AVERAGED SHAPE OF MEMBRANE

For each angle of attack and freestream velocity, the time-averaged membrane displacement, $\overline{z}$, in a direction normal to a chordline as a function of chordwise distance, x, was calculated from

$$\overline{z} = \frac{1}{N}\sum_{n=1}^{N} z_n \tag{24}$$

where z_n is an instantaneous membrane displacement in a direction normal to chordline, and N = 3000 (from 3000 images in the present investigation). The small interval of the chordwise distance x was equal to 0.01c, resulting in the

precision of 1% of the chord length (i.e., one hundred x-z coordinates per shape). The coordinates were then nondimensionalised by the chord length.

B) TIME-AVERAGED STRAIN

From the time-averaged shape, it was possible to calculate the time-averaged strain. Strain is defined as the deformation of the membrane elongated due to aerodynamic loads. The time-averaged strain $\bar{\delta}$ was calculated from the change of membrane length ΔL divided by the initial length L_0

$$\bar{\delta} = \frac{\Delta L}{L_0} = \frac{\bar{L} - L_0}{L_0} \tag{25}$$

where $\bar{L}$ is the time-averaged length of membrane calculated from the time-averaged shape

$$\bar{L} = \int \sqrt{\left(dx^2 + d\bar{z}^2\right)}\, dx \tag{26}$$

The time-averaged strain is then used to obtain time-averaged tension and therefore tension coefficient C_T.

C) TENSION COEFFICIENT

Tension occurs when the membrane is stretched, as a result of difference of pressure on either side of the membrane when subject to aerodynamic loads, and/or of the initial tension given in the case of membrane with pre-strain. For the investigation of the two-dimensional membrane aerofoil, the tension of the membrane is assumed to be constant along the membrane surface. The time-averaged tension of membrane is defined as the sum of pre-tension and the tension from aerodynamic loads follows

$$\bar{T} = S_0 t + E\bar{\delta} t = (S_0 + E\bar{\delta})t \tag{27}$$

where S_0 is pre-stress of membrane, defined as

$$S_0 = E\delta_0 \tag{28}$$

For the case of membrane with zero pre-strain and with excess length, S_0 becomes zero and the time-averaged tension reduces to

$$\overline{T} = E\overline{\delta}\,t \tag{29}$$

Tension coefficient is a dimensionless parameter characterising tension, defined as

$$C_T = \frac{\overline{T}}{q_\infty c} \tag{30}$$

D) STANDARD DEVIATION

When the membrane is unsteady, the standard deviation, also known as a root mean square (rms), of the membrane displacement in z-direction can be computed to indicate amplitudes of membrane oscillations. From the time-averaged membrane displacement $\overline{z}$, the standard deviation as a function of chordwise distance was calculated from

$$z_{SD} = \sqrt{\frac{1}{N}\sum_{n=1}^{N}\left(z_n - \overline{z}\right)^2} \tag{31}$$

In the present investigation, the z_{SD} was then nondimensionalised by the chord length c. The maximum value $z_{SD,max}$ for each angle of attack and freestream velocity can also be found.

E) POWER SPECTRAL ANALYSIS

The technique used to identify the membrane oscillating frequency was by observing the power spectral density of the signal from the time history of membrane displacement. The time history of the displacement was sampled at the point of maximum standard deviation ($z_{SD,max}$). From these signals, the power spectra of the membrane oscillations was analysed by *SPTOOL* in MatLab, using Fast Fourier Transform (FFT) method. From the spectral density analysis, the dominant frequency and sub-dominant frequencies could be determined.

F) STROUHAL NUMBER

Strouhal number or nondimensionalised frequency is a dimensionless number describing oscillating flow mechanisms. The term "Strouhal" is named after Vincenc Strouhal, a Czech physicist who studied wires experiencing vortex

shedding and singing in the wind in 1878 (White 1999). The Strouhal number is often defined as

$$St = \frac{fL}{V} \tag{32}$$

where f is commonly the frequency of vortex shedding, L is the characteristic length and V is the velocity of the fluid. However, in the present investigation in which the frequency of the oscillating membrane was measured, an alternative definition of the Strouhal number was used as

$$St = \frac{fc}{U_\infty} \tag{33}$$

where f is the oscillating frequency of the membrane c is chord length and U_∞ is freestream velocity. The oscillating of the membrane f was measured at the location of maximum standard deviation, and either from shape visualisation with laser (for the two-dimensional membranes) or Digital Image Correlation (for the low aspect ratio membrane wings). Exception is given to an additional investigation of vortex shedding frequency of the rigid aerofoil, in which the frequency f is the vortex shedding frequency measured with hot-wire anemometry. Further detail of the hot- wire measurement is explained in section 2.4.2.

G) MODE NUMBER

By plotting z_{SD} as a function of chordwise distance, the dominant mode number could be determined by counting the peaks. An example of the standard deviation showing the fifth mode is shown in Figure 2.10-a. In addition, the mode number could be confirmed by the mode shape of membrane plotted from a sequence of instantaneous shapes over one oscillating cycle (see Figure 2.10-b).

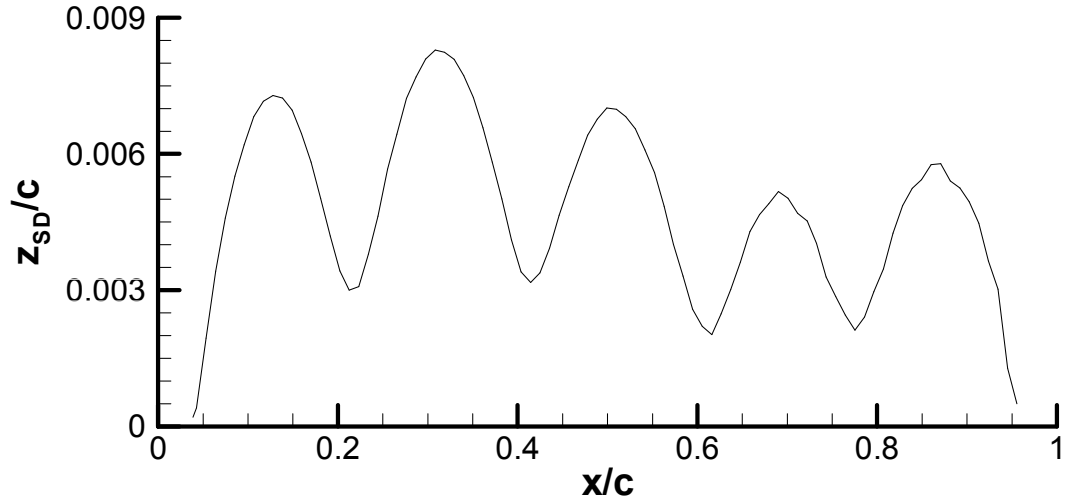

a)

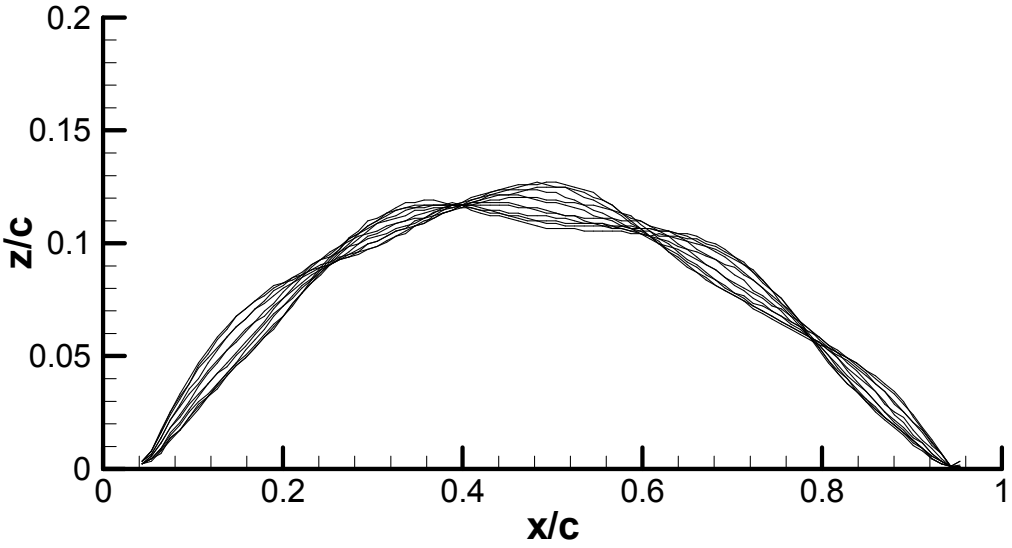

b)

Figure 2.10: Examples of the fifth mode of membrane oscillation for δ_0 = 0%, U_∞ = 10 m/s and α = 13°: a) Standard deviation indicating five peaks; b) Sequence of instantaneous membrane shapes plotted for one oscillating cycle.

2.4.2 HOT-WIRE MEASUREMENT

The hot-wire anemometer, also known as Constant Temperature Anemometer, is a point-measuring technique used for the measurement of time series in one, two, or three dimensional turbulent fluid flows. It measures a fluid velocity by detecting the heat convected away by the fluid. A hot-wire exposed at the core of the anemometer is either heated up by a constant current or maintained at a constant temperature. In either case, the heat lost to fluid convection is a function of the fluid velocity, converted by convective theory. Therefore, this device measures

velocity at a point and provides continuous velocity time series, which can be processed into amplitude and time-domain statistics. Principle diagram of the hot-wire anemometer is shown in Figure 2.11, and the specification of the hot-wire probe used can be seen in Table 2.2. For the present investigation, the hot-wire device was employed to measure the frequency of an unsteady flow over the rigid aerofoil.

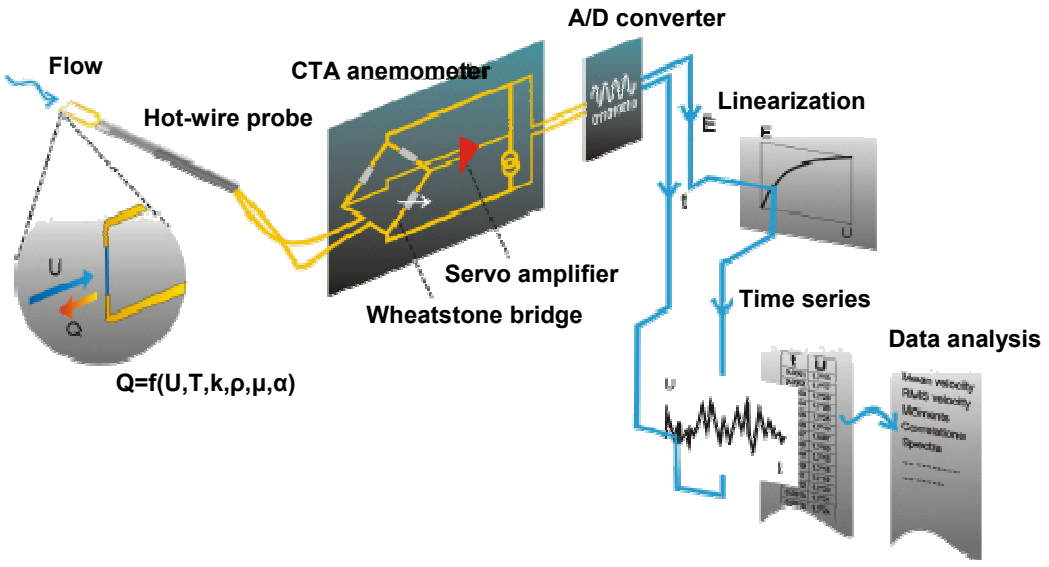

Figure 2.11: Principle of hot-wire anemometry system. Figure courtesy of Dantec Dynamics (www.dantecdynamics.com).

PROBE SUPPORT AND SENSOR PROBE	DANTEC DW2206 PROBE TYPE55
SENSOR RESISTANCE AT 20℃	R_{20} = 3.49Ω
LEADS RESISTANCE	R_L = 1.0Ω
SENSOR TCR	α_{20} = 0.36 %/℃

Table 2.2: Specification of the hot-wire sensor probe.

To measure the frequency of the flow fluctuation, the hot-wire probe was mounted vertically above the aerofoil and at the mid-span, with the sensor laid in a cross-flow direction. Before collecting data, it is necessary to determine a suitable position for placement of the hot-wire probe. It was found that the location downstream at a distance of approximately 2c from the leading-edge and at a horizontal level approximately the same as the leading-edge level was a suitable

position where fluctuating signals from the vortex shedding could be detected. The signal was loaded into a personal computer by using a data acquisition programme code created in HP VEE v.5.01 software. The frequency of the vortex shedding was then determined by using a Signal Processing toolbox (SPTool) in MatLab. Subsequently, the Strouhal number was calculated based on the chord length. The Strouhal number of the vortex shedding from the rigid aerofoil was also referred to as a wake velocity when compared to the oscillating frequency of the membrane, as discussed in Chapter 3 and Chapter 4. The uncertainty of the measurements of the vortex shedding frequency with hot-wire anemometry was estimated as 3%.

2.4.3 DIGITAL PARTICLE IMAGE VELOCIMETRY (DPIV)

PRINCIPLE

Particle Image Velocimetry (PIV) is a whole-flow-field technique providing instantaneous velocity vector measurements in a cross-section of a flow by measuring the velocities of micron-sized particles following the flow. A pulsed laser sheet illuminates a plane in the flow and the positions of the particles are recorded. A second laser pulse later illuminates the same plane, creating the second set of particle images. Once a sequence of two light pulses is recorded, the images are divided into small subsections called interrogation areas (IA). The interrogation areas from each image frame, I1 and I2, are cross-correlated with each other, pixel by pixel. The correlation produces a signal peak, identifying the common particle displacement. An accurate measure of the displacement, and thus also the velocity, is achieved with sub-pixel interpolation. A velocity vector map over the whole target area is obtained by repeating the cross-correlation for each interrogation area over the two image frames captured by the CCD camera. The use of the CCD camera and computing hardware results in real-time velocity maps. Schematic diagram of the PIV principle is shown in Figure 2.12.

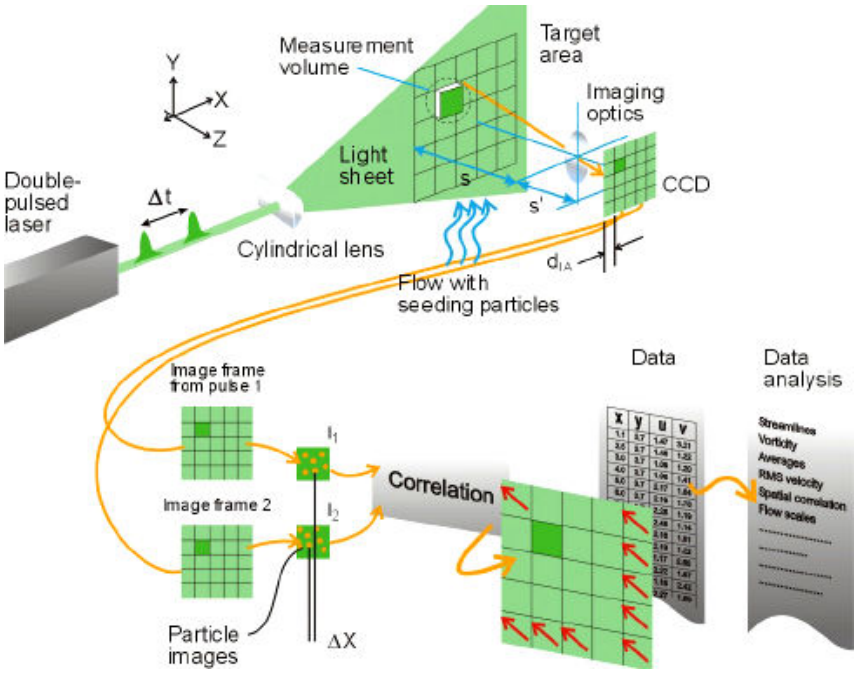

Figure 2.12: Principle of Particle Image Velocimetry (PIV). Figure courtesy of Dantec Dynamics (www.dantecdynamics.com).

PROCEDURE

Two different PIV systems were used. For the two-dimensional membrane aerofoils and the rigid aerofoil, quantitative flow measurements were undertaken using a high frame-rate Digital Particle Image Velocimetry (DPIV) system from TSI (Inc. USA). Illumination of the desired plane was achieved using a New Wave Pegasus Nd:YLF double pulse high speed laser with a maximum energy of 10mJ per pulse. The laser light sheet was placed parallel to the freestream velocity to illuminate a plane at the mid-span of the wing as shown in Figure 2.13. The PIV camera was placed normal to the flow, and the flow over the suction surface of the whole wing was imaged. For certain experimental cases, specific areas near the leading-edge or trailing-edge were investigated. The images were captured using a TSI PowerView HS-3000 high speed CMOS camera. A TSI LaserPulse synchroniser unit was utilised to link the camera and the laser to enable the accurate capture for two frame cross-correlation analysis. For these measurements, the velocity field was captured at a rate of 1,500 frames per second, at a resolution of 1024 by 1024 pixels, producing sequences of 3,000 instantaneous velocity fields over 2 seconds. A TSI model 9307-6 multi-jet

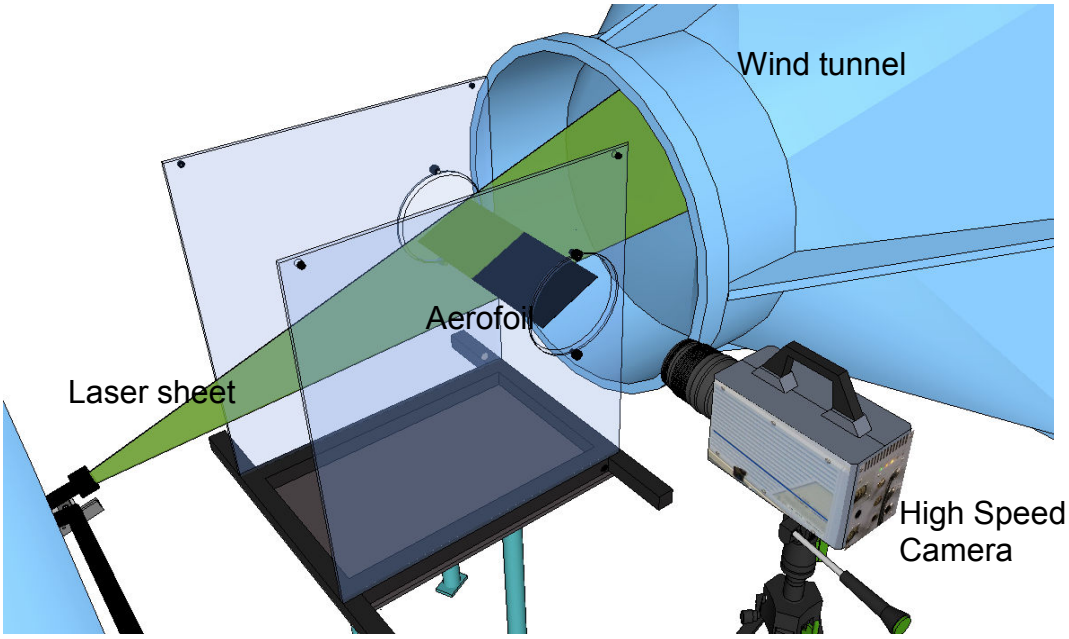

Figure 2.13: Schematic of Particle Image Velocimetry (PIV) measurement for two-dimensional aerofoils.

atomizer was used to produce oil droplets in order to seed the flow. The atomizer worked best using olive oil and the mean size of the droplets was 1μ. The commercial software TSI Insight3G and a FFT cross-correlation algorithm, which was provided in the software, were used for the analysis of the results obtained. The size of the interrogation window was 32 by 32 pixels. The effective grid size was around 2% of the chord length in these measurements. The measurement uncertainty for the velocity is estimated as 2% of the freestream velocity.

Once the studied parameters (time-averaged velocity, turbulence intensity, Reynolds Stress and instantaneous velocity) were plotted and exported as images, each image was then superimposed on the corresponding averaged shape of membrane. The time-averaged shapes of membrane were previously derived from shape visualisation technique. Matched position of the flowfield with the membrane image was calculated. Opacity of the membrane image was adjusted before it was superimposed on the flowfield image using Corel Photo-Paint and Tecplot software.

For the low aspect ratio wings, the flow measurements were undertaken using Digital Particle Image Velocimetry (DPIV). A pair of pulsed mini Nd: YAG lasers with a maximum energy output of 120 mJ per pulse was used to illuminate

the desired plane. The laser sheet was placed parallel to the freestream flow at the mid-span location for the measurements in a streamwise plane, and perpendicular to the freestream very close to the trailing-edge (2 mm distance) for the cross-flow measurements. A combination of cylindrical and spherical lenses was used to adjust both the thickness and the width of the laser sheet. Images were captured using an 8-bit TSI PowerView 4M CCD camera, placed perpendicular to the laser sheet as shown in Figure 2.14, with a resolution of 2048×2048 pixels and a maximum capture rate of 7.5 fps, producing 3.75 frames in cross-correlations.

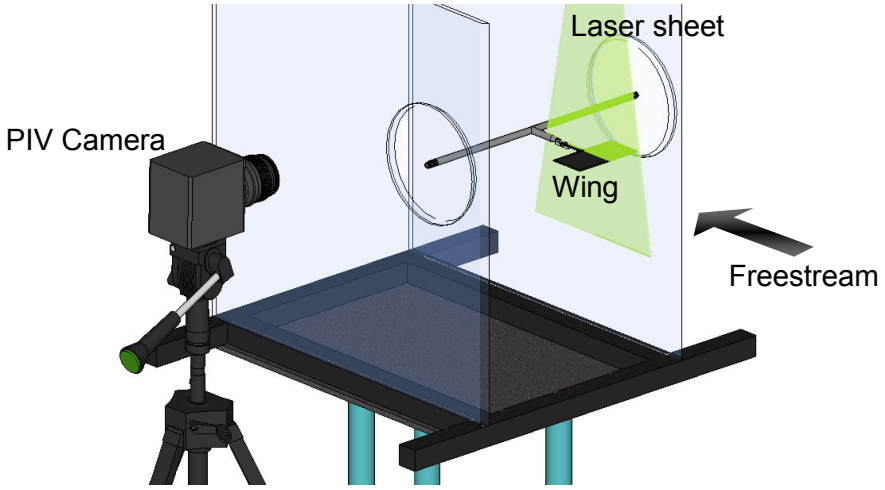

a)

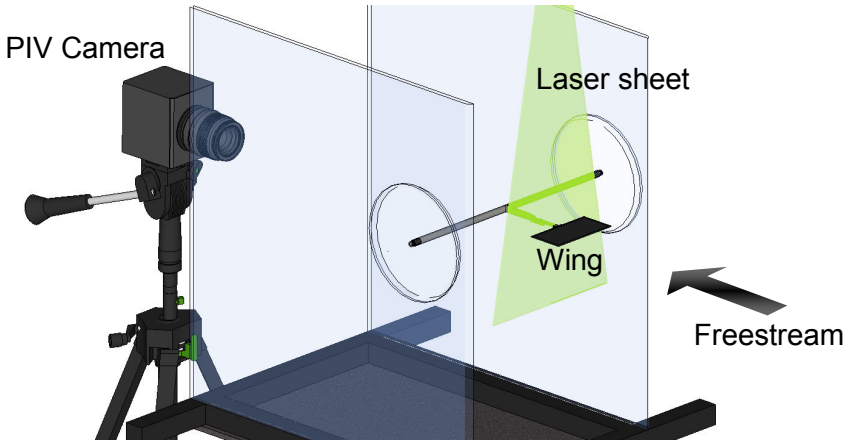

b)

Figure 2.14: Schematic of PIV measurements for a) streamwise plane and b) cross-stream plane near trailing-edge.

Sequences of 200 velocity fields were produced for each measurement. A synchroniser unit was used to synchronise the camera and the laser pulses. The commercial software TSI Insight v6.0 and a fast Fourier transform (FFT) cross-correlation algorithm were used to analyse the images, with interrogation window

size of 32 by 32 pixels, resulting in the effective grid size of approximately 2% of the chord length for both measurements in the streamwise plane and cross-flow plane. The uncertainty of the velocity measurements is estimated to be 2% of the freestream velocity.

Studied parameters for the low aspect ratio wings include time-averaged velocity, turbulence intensity, and circulation. The corresponding averaged shape of the membrane wing was added to the exported flowfield. For the streamwise measurements, these time-averaged shapes were previously calculated from the deformation measurements using Digital Image Correlation (DIC), details of which are described in section 2.4.5.

DATA ANALYSIS

A) FFT CORRELATION

Fast Fourier Transform (FFT) was used to estimate cross-correlation functions. This reduces the computation from $O[N^4]$ operations to $O[N^2 \log_2 N]$ operations in the case of a two-dimensional correlation. The correlation theorem of Fourier transforms (Bendat and Piersol 1986) states that the cross-correlation of two functions is equivalent to a complex conjugate multiplication of their Fourier transforms:

$$R_{AB} \Leftrightarrow \hat{A} \cdot \hat{B}^* \tag{34}$$

, where $\hat{A}$ and $\hat{B}$ are the Fourier transforms of A and B, respectively, and $\hat{B}^*$ represents the complex conjugate of $\hat{B}$.

For PIV measurement, the FFT processing gives the same results as the histogram approach, but is more efficient with the computer. The processing sequence is a 2D FFT on window 1 and a 2D FFT on window 2. The FFT result of window 1 is multiplied by the complex conjugate of the window FFT result of window 2. The correlation result is yielded by computing the 2D FFT of the multiplication result and taking the modulus.

B) TIME-AVERAGED VELOCITY

A sequence of vector files was averaged in TSI Insight 3G and Insight v6.0 software. The time-averaged velocity was calculated from

$$\bar{u} = \frac{1}{N}\sum_{n=1}^{N} u_n \tag{35}$$

$$\bar{v} = \frac{1}{N}\sum_{n=1}^{N} v_n \tag{36}$$

$$V = \sqrt{\bar{u}^2 + \bar{v}^2} \tag{37}$$

Where N is a total number of vector files, and u_n and v_n are instantaneous velocities in streamwise and cross-stream direction, respectively.

Vector files of the time-averaged velocity were then loaded into the Tecplot v9.0 (Amtec Engineering Inc.) data-plotting package, where they were nondimensionalised. The colour level representing a magnitude of the velocity contour was adjusted. In certain cases either the velocity vectors or the streamlines were also plotted.

C) SHEAR LAYER LOCATION

From PIV measurements for the two-dimensional membrane aerofoil, it is possible to measure the instantaneous shear layer location (l). The shear layer location is identified as the location of maximum vorticity measured from the membrane surface (from the time-averaged shape) in a vertical direction, as shown in Figure 2.15. The membrane displacement z' was also measured from the time-averaged membrane shape in a vertical direction. (For some experimental cases, in addition to the flow field, the PIV also simultaneously captured the membrane surface appearing as a white curve which enables the membrane displacement to be calculated). The calculation of vorticity is further explained in the next section. In Figure 2.15 both parameters (l and z') were measured vertically from the time-averaged shape at 75% of the chord length. For most cases, this chordwise distance (0.75c) was an optimal location where both membrane displacement and the shear layer location were more dominant (i.e., there are large membrane oscillations and an unsteadiness of shear layer at this

location, hence the correlation of these two parameters was more visible). The study of the instantaneous shear layer location and the corresponding membrane displacement (z′) as a function of time is particularly useful for the investigation of flow-membrane coupling.

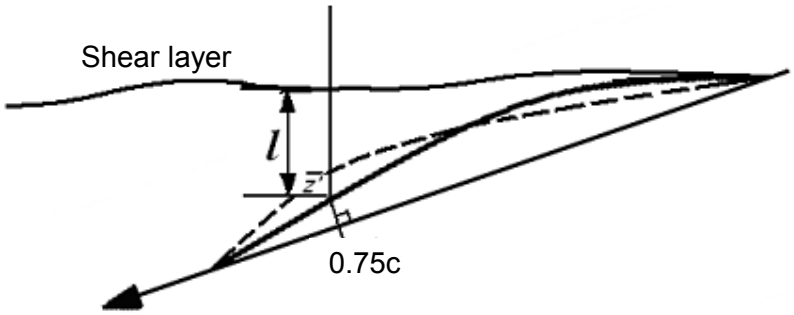

Figure 2.15: Explanation of shear layer location measured at 0.75c on the two-dimensional membrane aerofoil. Flow is from *right* to *left*.

D) VORTICITY AND CIRCULATION

Vorticity is a measure of the magnitude of rotation undertaken by the fluid. When vorticity is zero, the flow is called "irrotational", and the fluid elements have no angular velocity. Since there is no rotation the fluid's motion is purely translational. On the other hand, when the fluid elements have a finite angular velocity, the flow is defined as "rotational" flow, where the rate of the rotation defines the vorticity.

Vorticity, denoted as ω, is a measure of angular velocity where, in Cartesian coordinates,

$$\omega = \left(\frac{\partial w}{\partial y} - \frac{\partial v}{\partial z}\right)i + \left(\frac{\partial u}{\partial z} - \frac{\partial w}{\partial x}\right)j + \left(\frac{\partial v}{\partial x} - \frac{\partial u}{\partial y}\right)k \qquad (38)$$

where u, v and w denote the x, y, and z components of velocity respectively. In other words, the vorticity is equal to the curl of the velocity (Anderson 2001)

$$\omega = \nabla \times V \qquad (39)$$

From PIV data, the vorticity can be calculated from the velocity vectors. For the investigation of the two-dimensional membrane aerofoil, the location of the maximum magnitude of this vorticity measured vertically from the studied

chordwise distance (0.75c) was located in order to denote the shear layer location. Whereas the vorticity provides important information on the flowfield for the investigation of the low the aspect ratio membrane wing (Chapter5). In the latter case, the vorticity was nondimensionalised by multiplying by the chord length, and dividing by the freestream velocity:

$$\frac{\omega c}{U_\infty} \tag{40}$$

(Note that the symbol ω denotes vorticity and not angular velocity in the present thesis).

Another aerodynamic parameter related to the vorticity is circulation. Circulation is simply the negative of the line integral of velocity around a closed curve in the flow. It is a kinematic property depending only on the velocity field and the choice of the curve. The circulation, denoted by Γ, is defined as

$$\Gamma \equiv -\oint_c V \cdot ds \tag{41}$$

It is noted that the positive sense of the line integral is counterclockwise. However, a positive circulation in aerodynamics is considered as being clockwise.

The circulation is related to vorticity, and can also be defined as equal to the vorticity integrated over an open surface

$$\Gamma = \iint_s (\nabla \times V) \cdot ds \tag{42}$$

Whereas the vorticity provides information on the flowfield, the circulation is the quantity to refer to when the strength of a vortex is being discussed.

In the present investigation, both parameters are discussed. The calculation of vorticity was done in Tecplot v10.0. For the calculation of the circulation, the integration area that encompasses each vortex was rectangular in shape, chosen manually by the author. The choice was based on the actual size of vortex calculated and plotted as a contour. The maximum value of the circulation was calculated, and it is this value that is presented in the results discussed later on.

The circulation was then nondimensionalised by the freestream velocity and the chord length as follows

$$\frac{\Gamma}{U_\infty c} \tag{43}$$

The velocity field was loaded into MATLAB, wherein the calculation was made.

E) TURBULENCE INTENSITY

Turbulence can be defined as fluctuations in fluid flow. Generally speaking, a steady flow would have low turbulence, whereas an unsteady flow would have higher turbulence. An ideal flow with no fluctuations in flow speed or direction would have a turbulence intensity value of 0%. Turbulence intensity is a useful measurement scale used to indicate the level of turbulence of the flow.

Turbulence intensity is a dimensionless parameter characterising turbulence. In some literatures the turbulence intensity is defined as the root mean square (rms), or standard deviation, of the fluctuating velocity at a particular location over a specified period of time normalised by the average velocity at the same location over same period of time. However, the present investigation employed an alternative definition of turbulence intensity, which was calculated from the following equation

$$\frac{\overline{u'^2 + v'^2}}{U_\infty^2} \tag{44}$$

where u' and v' are fluctuating velocities (taken from PIV data) in streamwise and cross-stream direction, respectively.

The calculation was done in both TSI Insight 3G and Tecplot v9.0 software. The latter software was also used to finalised and export the plot as an image.

F) REYNOLDS STRESS

In fluid dynamics, the Reynolds stress, also commonly known as the Reynolds stress tensor, is the stress tensor in fluid due to the random turbulent fluctuations in fluid momentum. To illustrate the Reynolds stress, consider the steady,

incompressible flow for a Newtonian fluid in Cartesian coordinate. The momentum equation follows

$$\rho\left(u\frac{\partial u}{\partial x}+v\frac{\partial u}{\partial y}\right)=-\frac{\partial p}{\partial x}+\mu\left(\frac{\partial^2 u}{\partial x^2}+\frac{\partial^2 u}{\partial y^2}\right) \tag{45}$$

If the Reynolds decomposition

$$\begin{aligned} u &= \bar{u}+u' \\ v &= \bar{v}+v' \\ p &= \bar{p}+p' \end{aligned} \tag{46}$$

are used in the momentum equation, the equation can be rearranged to arrive at a well known form

$$\rho\left(\bar{u}\frac{\partial \bar{u}}{\partial x}+\bar{v}\frac{\partial \bar{u}}{\partial y}\right)=-\frac{\partial \bar{p}}{\partial x}+\frac{\partial}{\partial y}\left(\mu\frac{\partial \bar{u}}{\partial y}-\rho\overline{u'v'}\right) \tag{47}$$

where the Reynolds stress, $-\rho\overline{u'v'}$, is collected with the traditional surface shear stress terms $\mu\frac{\partial \bar{u}}{\partial y}$.

The present investigation used an alternative term of nondimensionalised Reynolds stress calculated from the following term

$$\frac{-\overline{u'v'}}{U_\infty^2} \tag{48}$$

where fluctuating velocities u' and v' were taken from PIV data. This parameter could imply the magnitude of mean forces imposed on the mean flow by turbulent fluctuations. Similar to the turbulence intensity, the calculation was done in both TSI Insight 3G and Tecplot v9.0 software, and the latter software was also used to finalised and export the plot as an image.

2.4.4 SMOKE VISUALISATION

Smoke visualisation technique was developed for the investigation of flow pattern over the two-dimensional membrane aerofoil as well as the rigid aerofoil. A strip of wire was clamped vertically in the upstream direction, and at the mid-span of the aerofoil. The distance between the wire and the leading-edge of the aerofoil was 7mm. The diameter of the wire was as small as 0.12 mm; therefore the disturbance effect on the freestream from the wire was negligible. In order to generate smoke, oil (Propanol: $C_3H_8O_2$) was dropped onto the wire continuously by a small valve from a dripping system placed above the wire. With a current from the power supply applied to the wire, the oil was burnt by the heat, and the smoke was generated. A spotlight was used to illuminate the smoke, hence to improve visualisation quality. The high speed camera (*Photron FASTCAM APX*) was employed to capture images of smoke flow over the aerofoil's upper surface at 1,000 frames per second. The images were recorded for a period of time of approximately 10 seconds each case. The images presented in this thesis (in Chapter 3 and Chapter 4) represent typical flow patterns showing the interesting characteristics of flow-membrane interaction.

2.4.5 DIGITAL IMAGE CORRELATION (DIC)

PRINCIPLE

Digital Image Correlation (DIC) system is a non-intrusive full-field measurement technique originally developed at the University of South Carolina (Chu et al. 1985; Bruck et al. 1989; Peter and Ranson 1982). It employs a mathematical correlation method to measure deformation on an object's surface. The underlying principle is to track the deformation of grey value pattern applied to the surface by capturing consecutive images and then calculate the displacement field of the specimen. Two pre-calibrated CCD cameras acquire the speckling patterns when no load is applied to the specimen, referred to as a reference image. The cameras then acquire the patterns after loading, and the analysis finds a region that maximizes a normalised cross-correlation function corresponding to a small subset or facet of the reference images. The coordinates of the reference frame are then transformed to coordinates within the deformed image. The principle of 3D image correlation is shown in Figure 2.16.

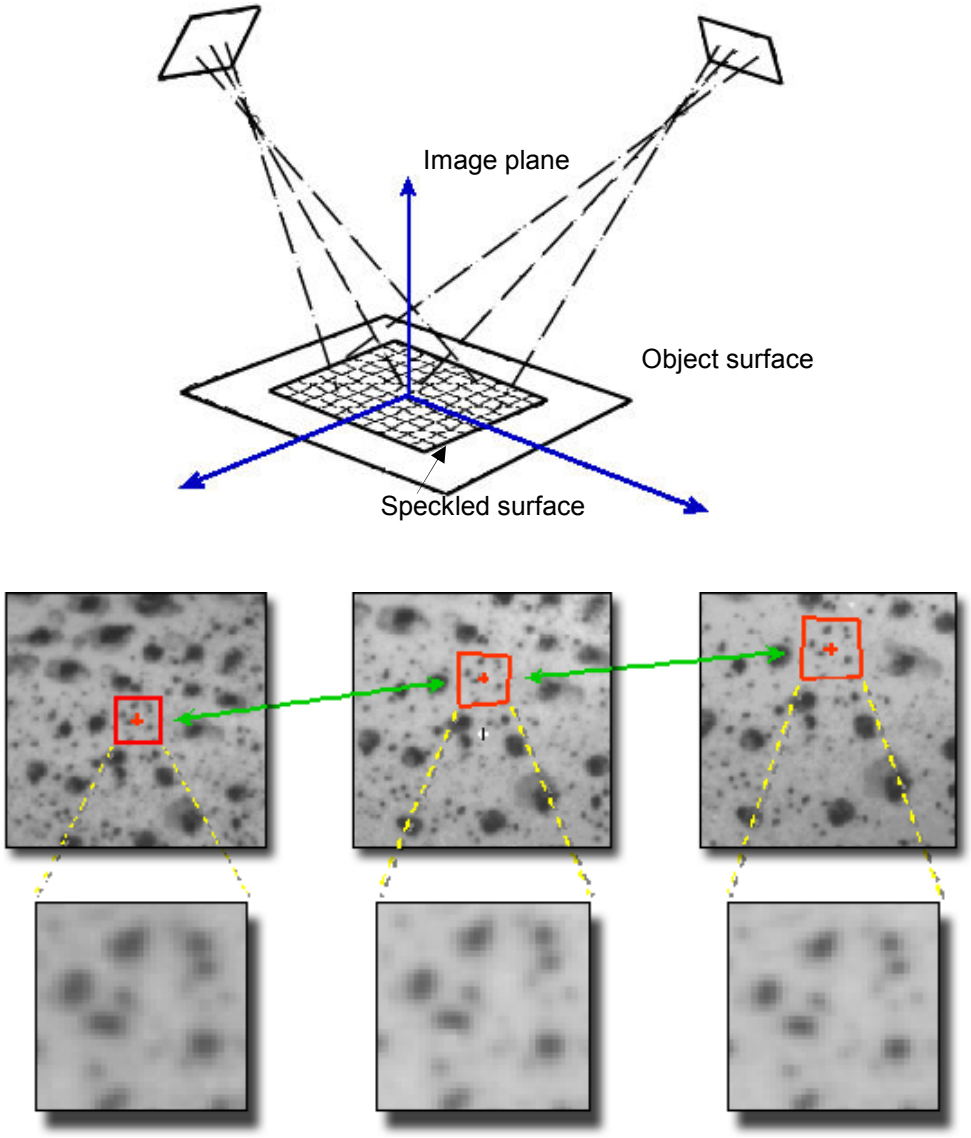

Figure 2.16: Principle of 3D Image Correlation System. The method tracks the gray value pattern in small neighborhoods called subsets (indicated in red) during deformation. Figure courtesy of Correlated Solutions (www.correlatedsolutions.com).

PROCEDURE

The investigation of the low aspect ratio membrane wings (rectangular and delta wings) employed the 3D digital image correlation which allowed the measurement of all three surface displacement fields simultaneously. Two calibrated and synchronised cameras (FASTCAM SA1.1, Photron 192.168.0.11 lens: Nikon AF NIKKOR24 24-85mm 1:2.8-4 D) were mounted above and behind the set-up, looking from a different viewing angle (as shown in Figure 2.17). Two flash lamps were used to illuminate the model (due to the cooling effect of the wind tunnel, the energy emitted from the lights which could damage

the membrane was not a concern). The cameras captured images at a rate of 1500 frames per second, corresponding to exposure time of 0.667 ms, producing sequences of 1500 instantaneous deformation fields over 1 second.

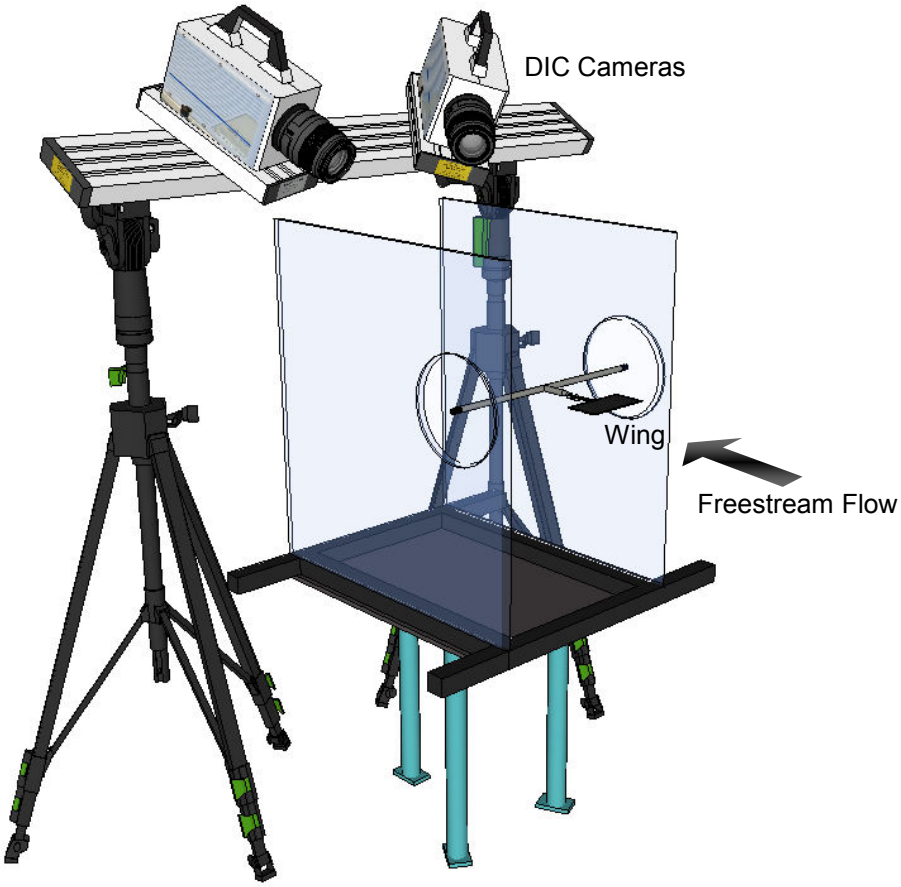

Figure 2.17: Schematic of 3D Digital Image Correlation for the membrane deformation measurement.

The custom software VIC3D 2007 (Limess Messtechnik und Software GmbH) was used for the analysis of the digital images obtained. The subset size (or correlation window size) varied from 17-21 pixels, and the grid step from 4-6 pixels, resulting in an effective grid size around 1% of the chord length in these experiments. The uncertainty of the deformation measurements in the out of plane direction is estimated to be 0.04% of the chord length. Typical data results consist of the geometry of the surface in discrete coordinates and the corresponding displacements. Post-processing within the software involved transformation of coordinates, and selecting the wing's rigid body as a reference plane. Final post-processing was complemented in MATLAB to calculate mean displacement (z), extract the maximum value (z_{max}), calculate standard deviation (z_{SD}) and find the

maximum value ($z_{SD,max}$). Time history of the displacement was acquired at the location of the maximum standard deviation. From the time history of the displacement, the oscillating frequencies were determined by power spectral analysis. The principles for all calculations are similar to those of the shape visualisation technique. The calculations were computed in MatLab (The Mathworks Inc.) and Tecplot v10.0, where all the graphics were plotted in Tecplot v10.0 software.

2.4.6 FORCE MEASUREMENT

Force measurement was conducted for the investigation of the low aspect ratio membrane wings as well as the rigid wings. A load cell was used to make direct force measurements in a normal direction to the chordline. The drawings and specifications of the load cell are shown in Figure 2.18.

Calibration was performed by loading the load cell with known weights. Calibration was repeated before each set of experiments to ensure consistency. Sets of data chosen at random were repeated to ensure that the results could be reproduced. The load cell was attached underneath the wing, with the other end screwed to the wing's support as shown in Figure 2.19. The force data was collected at a sampling frequency of 3000 Hz over 20 seconds.

The time-averaged normal force F_n was calculated from the captured signal. The normal force coefficient is a dimensionless parameter given by

$$C_n = \frac{F_n}{\frac{1}{2}\rho U_\infty^2} \tag{49}$$

The measurement uncertainty for the normal force coefficient is estimated to be 2%. In the present investigation, the normal force is a component that significantly contributes to the lift. Disruption in the normal force as the angle of attack increases could therefore indicate stall.

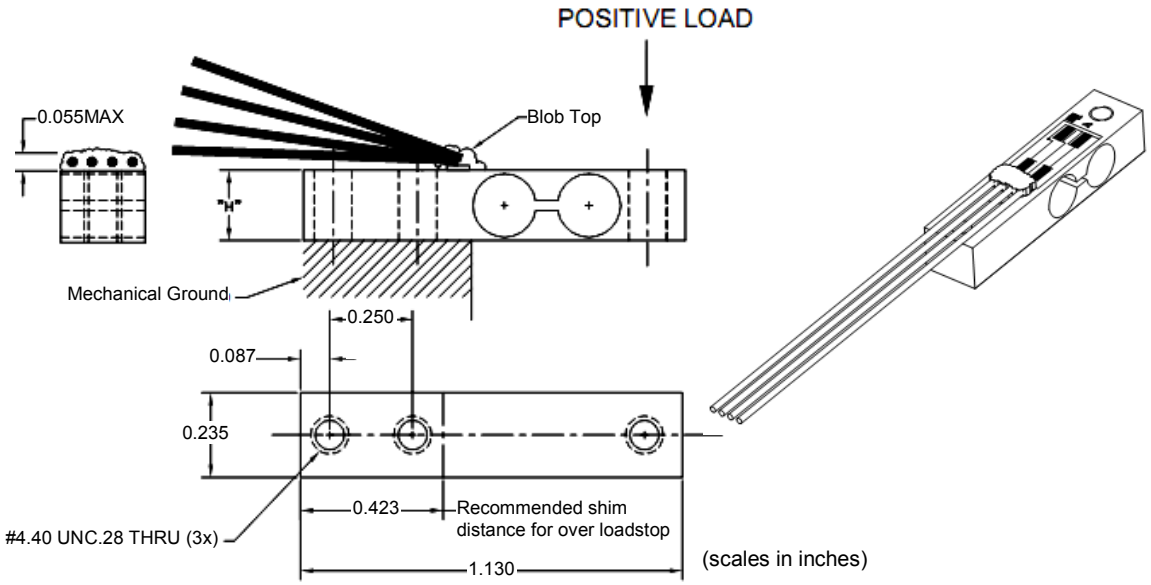

CAPACITIES	2, 4, 12, 22 lbf (900g., 1.8, 5.5, 9.9
RATED OUTPUT	2 mV/V NOMINAL
ZERO OFFSET	±0.3 mV/V (OPTIONAL ±%RO)
OVERLOAD SAFE	200% RO
EXCITATION RECOMMENDED	UP TO 20Vdc
BRIDGE RESISTANCE	10000 Ω±3%
BRIDGE CONFIGURATION	4-WIRE CLOSED BRIDGE
INSULATION RESISTANCE	>1000 MΩ at 50Vdc
OPERATING TEMP. RANGE	-40℃ TO +150℃ (200℃ OPTIONAL)
CALIBRATED TEMP. RANGE	-40℃ TO 125℃
TEMP. EFFECT ON ZERO BALANCE	±0.03%/℃ (±0.017%/℉)
TEMP. EFFECT ON SPAN	±0.03% READING/℃ (±0.017%/℉)
LONG TERMS STABILITY	<0.1% RO PER YEAR
NONLINEARITY	±0.03% RO
HYSTERESIS	±0.03% RO
NONREPEATABILITY	<0.01% RO
CREEP, IN 20 MINUTES	<±0.02% RO
CLEARANCE FOR WIRES AND STRAIN	0.055”MAX ABOVE TOP OF LOAD
ELECTRICAL TERMINATION	32AWG TEFLON WIRE, 2.5” LONG
DEFLECTIONS	0.0045” (2lb-F)

Figure 2.18: Drawing and specifications of the load cell used for force measurement. Figure courtesy of Strain Measurement Devices (www.smdsensors.com).

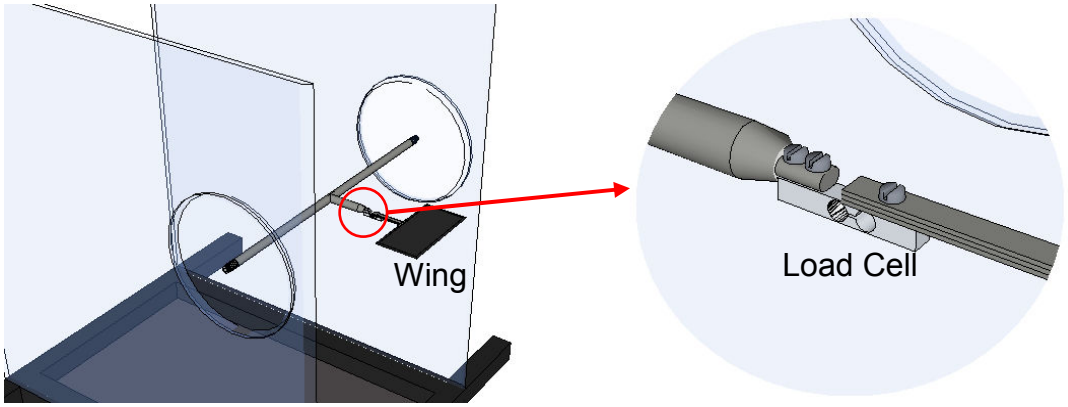

Figure 2.19: Schematic of a load cell attached underneath the wing's support for force measurement.

2.4.7 TEST PARAMETERS

REYNOLDS NUMBER

All the experiments in the current research were conducted at freestream velocities U_∞ = 5, 7.5, and 10 m/s. The Reynolds number was calculated, based on the chord length of the model tested each time, using

$$\mathrm{Re} = \frac{U_\infty c}{\nu_\infty} \tag{50}$$

,where $\nu_\infty = 1.412\times10^{-5}$ m^2/s. Reynolds numbers for each experimental case are summarised in Table 2.3.

AEROELASTIC PARAMETER

Effects of membrane elasticity are as important as Reynolds number due to its contribution to membrane tension and hence pressure difference between upper and lower surface. Therefore, aeroelastic parameter Π_1 was considered for each test. The aeroelastic parameter is defined as

$$\Pi_1 = \left(\frac{Et}{q_\infty c}\right)^{1/3} \tag{51}$$

Further details of this parameter are discussed in Chapter 1 (Two-dimensional membranes). Aeroelastic parameter numbers for each experimental case are summarised together with Reynolds number in Table 2.3.

Model	Reynolds Number, Re	Aeroelastic Parameter, Π_1
2D Membrane	53100, 79700, 106000	5.77, 4.41, 3.64
Rectangular Wing	24300, 36500, 48700	7.51, 5.73, 4.73
Delta Wing	29300, 44000, 58600	7.06, 5.38, 4.44

Table 2.3: Reynolds numbers and aeroelastic parameters tested for different models.

CHAPTER 3: AERODYNAMICS OF MEMBRANE AEROFOILS WITH ZERO PRE-STRAIN

3.1 INTRODUCTION

This Chapter was initially inspired by the encouraging results obtained from researches on membrane wing MAVs such as an improvement in longitudinal static stability, lift to drag ratio and gust rejection compared to a rigid wing with similar geometry (Shyy et al. 1997; Shyy et al. 1999a; Waszak et al. 2001; Ifju et al. 2002; Lian et al. 2003b; Lian and Shyy 2005; Albertani et al. 2007; Stanford et al. 2008; Stanford and Ifju 2009). Even though these impressive performances of the membrane wing have been demonstrated, various fundamental characteristics of the membrane are still unexplored, particularly the unsteady aspects. Most of the numerical studies neglect the presence of flow separation and viscous effects, and hence limit the accuracy of the results. The existing potential flow theory can only be sufficient for membranes at small incidences and with small cambers. As the first step of the experimental investigations for the current thesis, the study was simplified by using a simple two-dimensional membrane aerofoil without added pre-strain or excess length ratio. The main objectives of this Chapter were therefore to understand the characteristics of low Reynolds number flow over a two-dimensional membrane aerofoil with zero pre-strain. Membrane deformation, mean flow, membrane oscillations, unsteady flow, and the interaction of the separated flows with the membrane were examined. These aspects were investigated by using a high-speed camera with laser for the visualisation of membrane shapes, and by using Digital Particle Image Velocimetry for time-

accurate velocity measurements. Smoke flow visualisation was also included, and a comparison with a rigid aerofoil was also made.

3.2 MEAN SHAPE OF MEMBRANE

Figure 3.1 shows examples of the time-averaged membrane shape for various angles of attack for U_∞ = 7.5 m/s. Note that the displacement is zero in the small regions near the rigid leading-edge and trailing-edge. It is also seen in this plot that the maximum membrane displacement (also the point of maximum camber) is forward of the mid-chord point for high angles of attack, which is consistent with previous predictions and experiments from Greenhalgh et al. (1984).

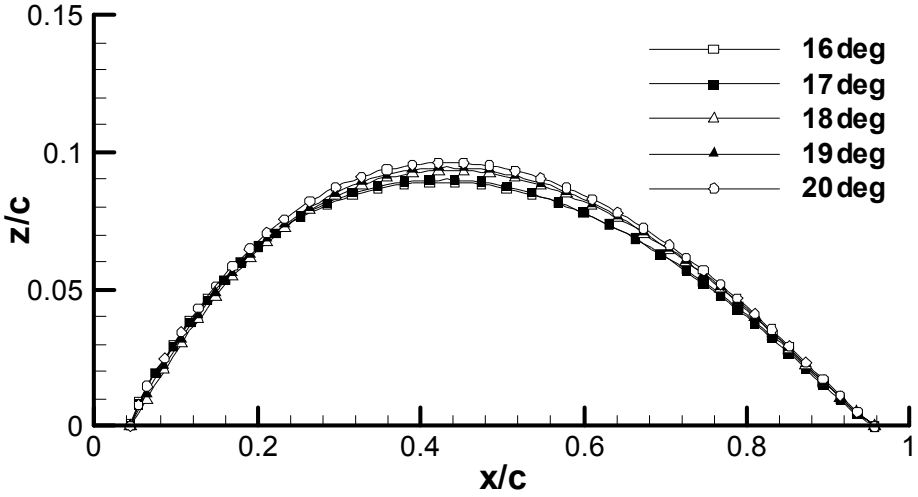

Figure 3.1: Examples of time-averaged membrane shapes at different angles of attack, U_∞ = 7.5 m/s.

Figure 3.2 and Figure 3.3 show the maximum camber and its chordwise location as a function of angle of attack for three different freestream velocities. Note that the data for $\alpha \leq 2°$ are not shown as the bistable instability known as luffing (Newman 1987) occurs in this region when the membrane is just as likely to set itself on one side as the other. The lift also experiences hysteresis (Greenhalgh et al. 1984) in this region. The maximum camber increases gradually up to about α = 16° for the lowest speed (U_∞ = 5 m/s) and then stays roughly constant. For U_∞ = 7.5 m/s, the maximum camber exhibits very small increase with angle of attack. For the largest freestream velocity, the variation in the maximum camber with incidence is relatively small. In general, the changes in the maximum camber are small as the angle of attack is varied for all three speeds, which is consistent with

previous observations presented by Newman and Low (1984) and simulations by Gordnier (2008). This is different from what is expected in attached flows, and is due to the separated flows being predominant at these low Reynolds numbers.

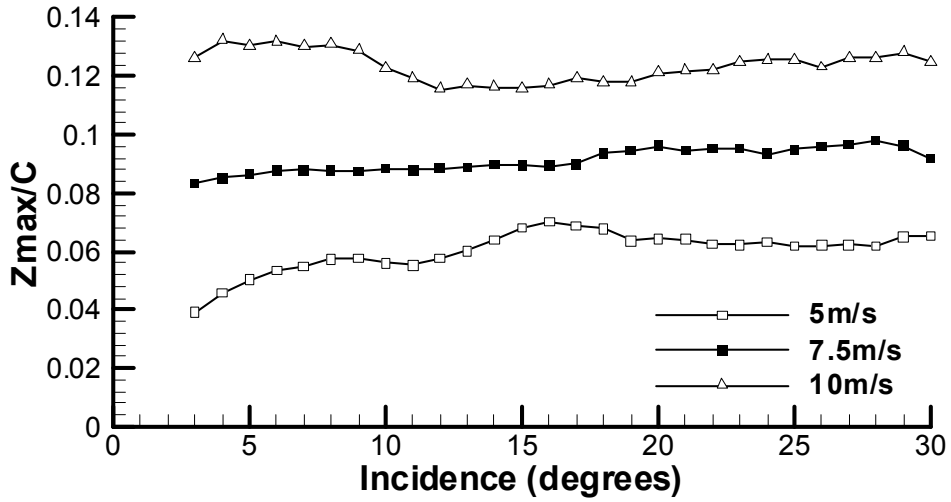

Figure 3.2: Variation of maximum camber as a function of angle of attack for three freestream velocities.

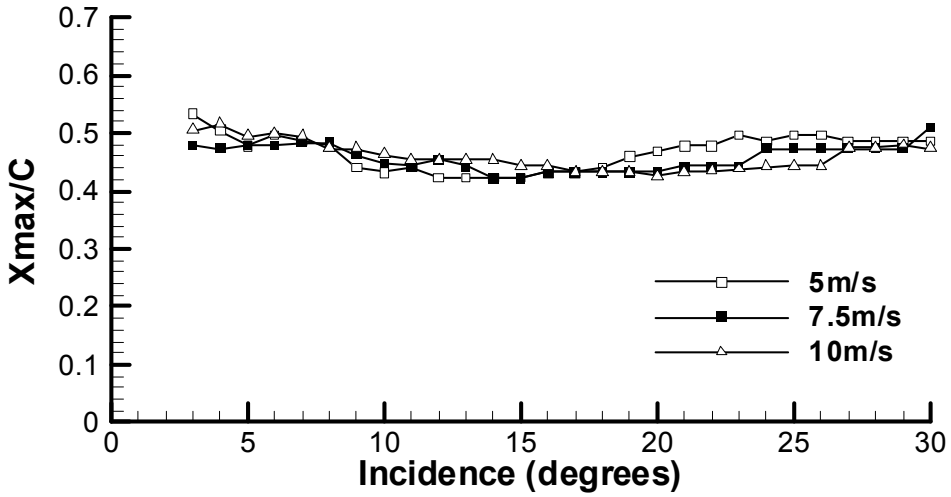

Figure 3.3: Variation of chordwise location of the maximum camber as a function of angle of attack for three freestream velocities.

Figure 3.3 shows that the location of the maximum camber is not very sensitive to the freestream velocity either. For all cases, the membrane shape is symmetrical about the mid-chord point for small incidences, which is also predicted theoretically (Newman and Low 1984). The location of maximum camber moves forward as the angle of attack is increased up to $\alpha \approx 15°$. This is also consistent with previous observations and predictions (Newman and Low 1984). There is a

trend of the location of the maximum camber moving back to the mid-chord point at higher angles of attack.

From the mean shape of the membrane acquired experimentally, an additional analytic prediction of lift coefficient was done, based purely on the classical thin aerofoil theory. By using the thin aerofoil theory on the time-averaged membrane shape, it is seen in Figure 3.4 that the lift is higher for the membrane. This is not surprising because the self-induced camber is expected to raise the lift coefficient of a flat plate. As previously shown in Figure 3.2, the camber is also larger for higher freestream velocities and this results in a larger lift shown in the prediction. Since the changes in maximum camber when varying angle of attack are relatively small, the lift slopes are virtually constant, and are close to the theoretical value. However the camber alone is not the only feature that explains the advantage of the membrane. It will be shown later that the membrane oscillation can differ the flow significantly especially at high incidences, at which the accuracy of the theory would be limited due to viscous effect and unsteady flow.

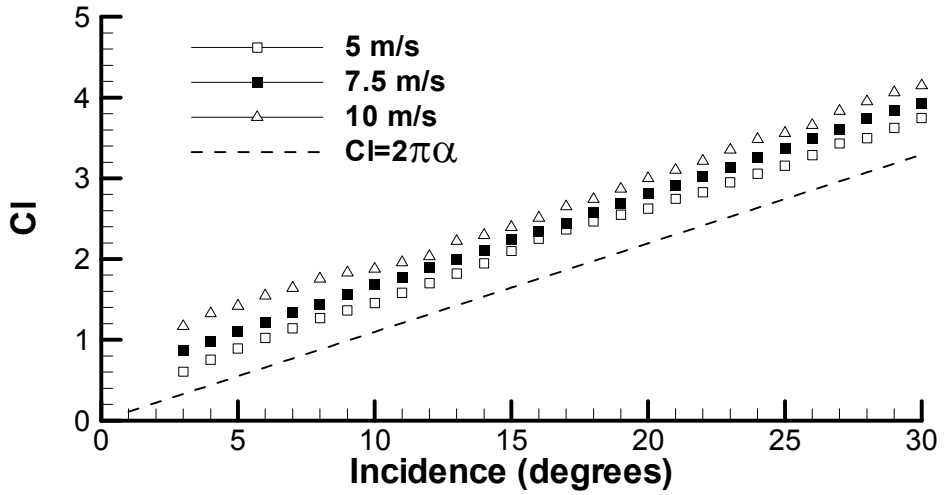

Figure 3.4: Lift coefficient estimated from the time-averaged shape of membrane aerofoil based on the thin aerofoil theory at different freestream velocities.

3.3 MEAN FLOW

Even though the flow remains attached to the membrane surface at low degrees of angle attack, a small leading-edge separation bubble is evident. This mild separation bubble is not expected to affect the pressure distribution significantly, however. When the flow remains attached, oscillations of the membrane are very

small. Consequently, the present investigation focuses on larger angles of attack near the stall and in the post-stall regime. Figure 3.5 shows the magnitude of the time-averaged velocity field superposed on the streamline pattern. For selected angles of attack, the data were taken in two different regions (one near the leading-edge and the other near the trailing-edge).

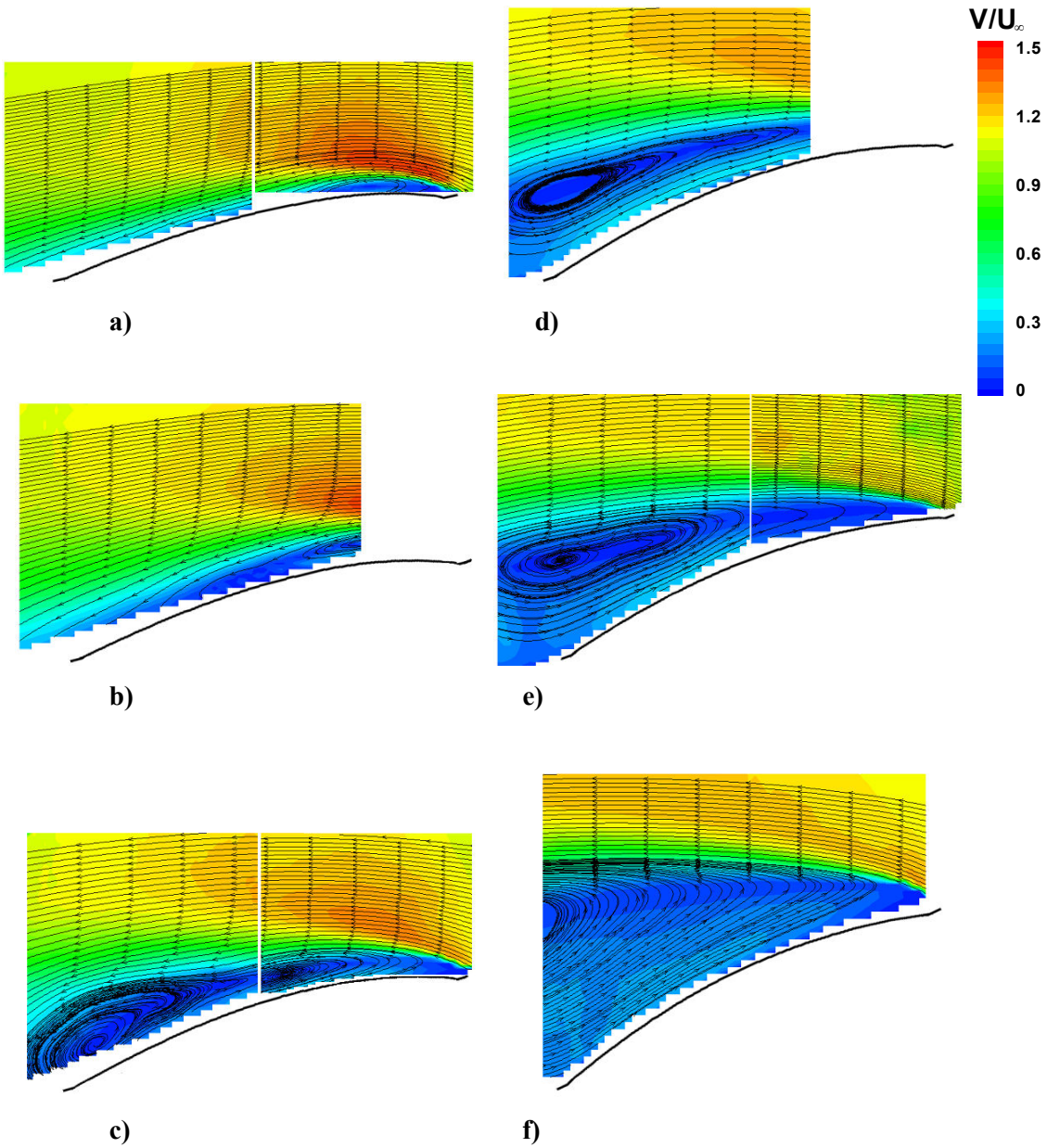

Figure 3.5: **Magnitude of the time-averaged velocity and streamlines at different angles of attack, U_∞ = 5 m/s: a) $\alpha = 12^o$; b) $\alpha = 14^o$; c) $\alpha = 16^o$; d) $\alpha = 18^o$; e) $\alpha = 20^o$; f) $\alpha = 25^o$. Flow is from *right* to *left*.**

Starting with $\alpha = 12°$, the flow is separated, but the shear layer remains very close to the membrane. With increasing angle of attack, the separated shear layer moves away from the surface. For $\alpha = 16°$, closed streamline pattern develops near the trailing-edge. The recirculation region becomes larger and moves further downstream with increasing angle of attack to $\alpha = 18°$ and 20°. For the largest angle of attack $\alpha = 25°$, the centre of the closed recirculation region is no longer on the membrane surface. If the time-averaged membrane shape (Figure 3.2 and Figure 3.3) and the time-averaged flow (Figure 3.5) are considered together, it is concluded that the changes in the mean membrane shape are much smaller than the changes in the mean flow as the angle of attack is varied for a given freestream velocity.

Figure 3.6 shows the magnitude of the time-averaged velocity and streamlines for different freestream velocities at $\alpha = 20°$. With increasing freestream velocity (increasing Reynolds number Re and decreasing aeroelastic parameter Π_1), there is a trend of shear layer getting closer to the surface while the camber increases. It will be shown later on that this affects the onset and the amplitude of the membrane oscillations. Although the effect of Re and Π_1 could not be separated in these experiments, this was done in the numerical simulations by Gordnier (2008). It was shown that there was a significant reduction in the size of the separation zone with increasing Reynolds number at a fixed parameter Π_1.

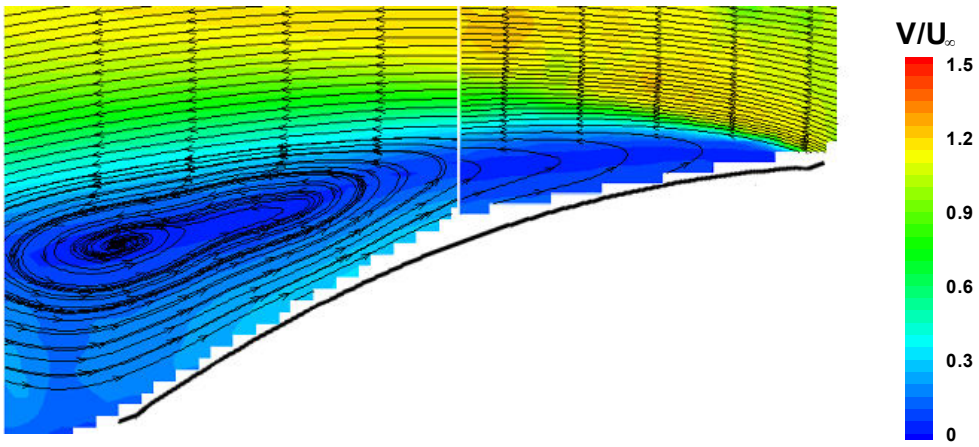

a)

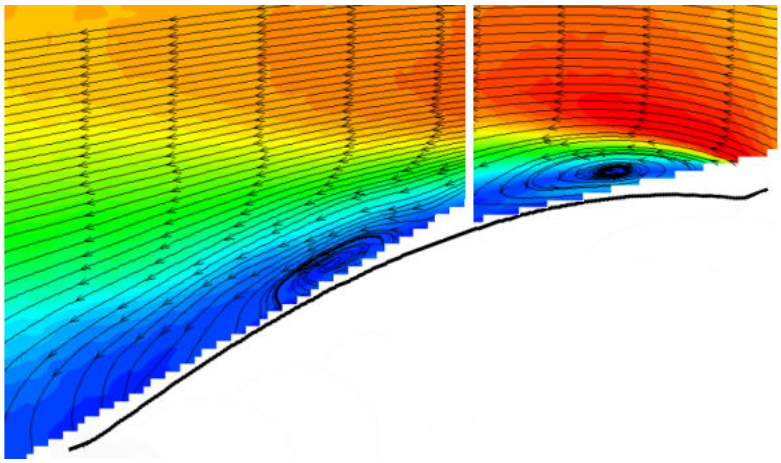

b)

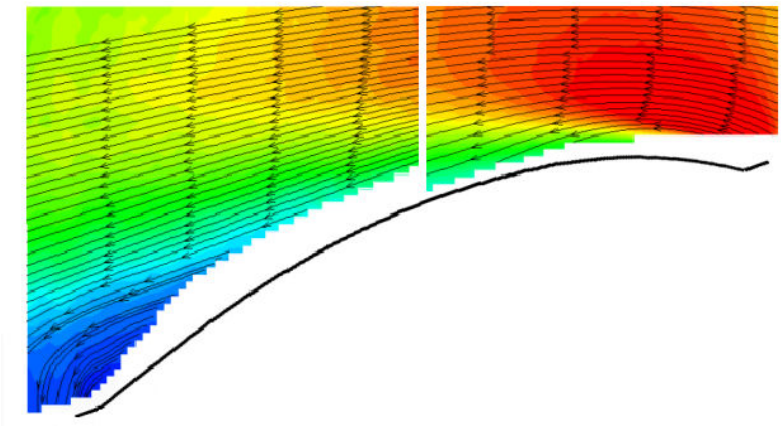

c)

Figure 3.6: **Magnitude of the time-averaged velocity and streamlines at different freestream velocities, α = 20°: a) U_∞ = 5 m/s; b) U_∞ = 7.5 m/s; c) U_∞ = 10 m/s. Flow is from *right* to *left*.**

3.4 MEMBRANE OSCILLATIONS

Figure 3.7 shows examples of different modes of membrane oscillations as indicated by the variation of the standard deviation with the chordwise distance. Examples of the second mode (Figure 3.7-a), the third mode (Figure 3.7-b), the forth mode (Figure 3.7-c) and the fifth mode (Figure 3.7-d) are shown for various freestream velocity and angle of attack combinations. Actually, it is noted for α = 10° and 11° in Figure 3.7-d that, the mode number appears to be three, and jumps to five for other incidences in this figure.

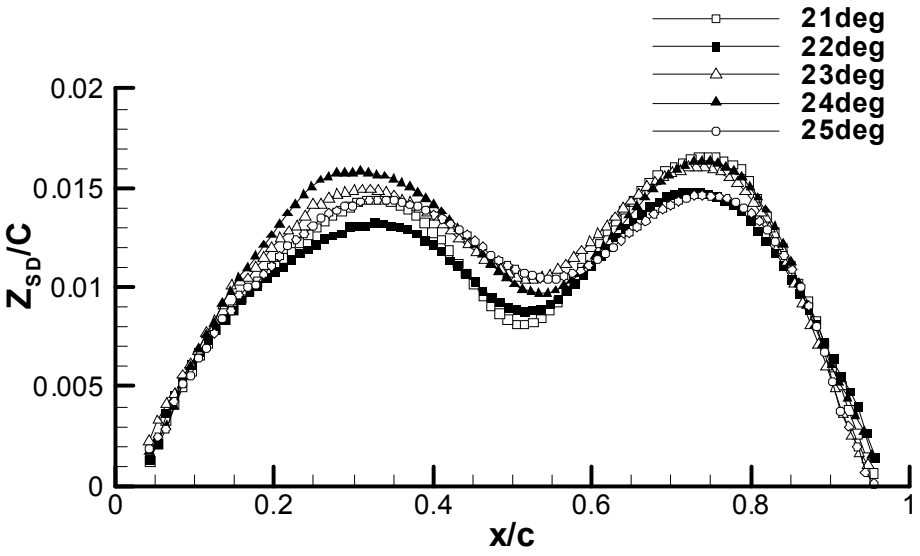

a)

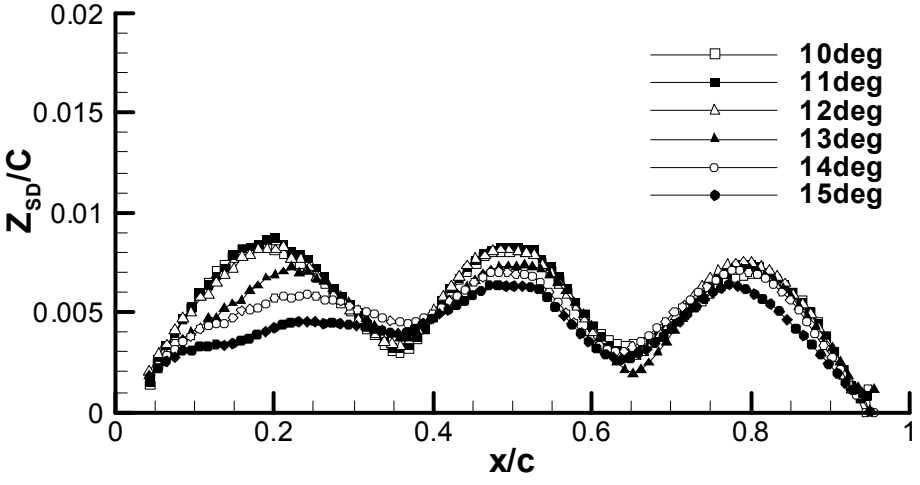

b)

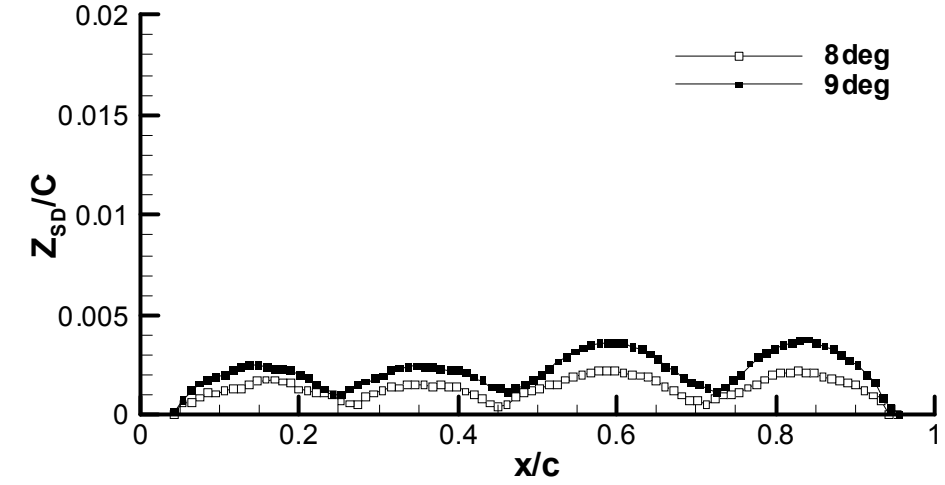

c)

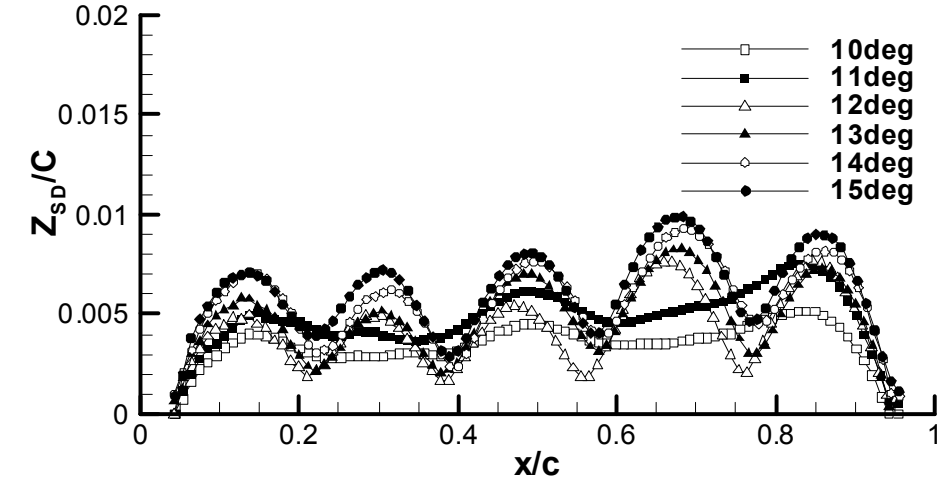

d)

Figure 3.7: **Variation of the standard deviation of the membrane displacement normalised by chord length, showing examples for: a) U_∞ = 10 m/s, second mode; b) U_∞ = 7.5 m/s, third mode; c) U_∞ = 10 m/s, forth mode; d) U_∞ = 10 m/s, fifth mode.**

The power spectral densities of the membrane oscillations are shown in Figure 3.8. The densities are plotted as an intensity map, indicating the membrane vibration in log-scale. At moderate incidences, it is seen that the mode number increases with the freestream velocity. It is interesting that, when $\alpha \geq 20°$, the second mode is observed regardless of the freestream velocity. This suggests a possible coupling of membrane with the wake flow at these post-stall incidences.

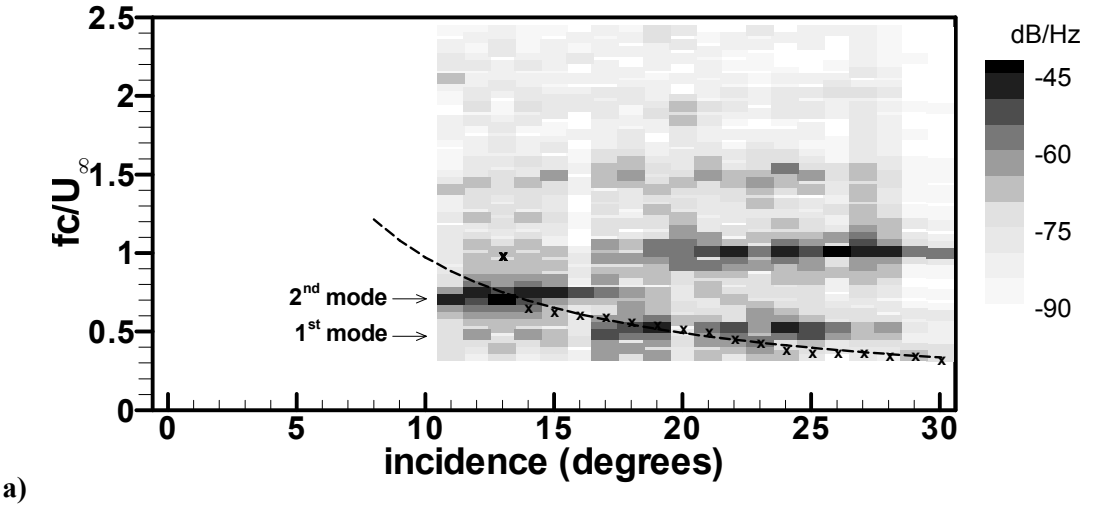

a)

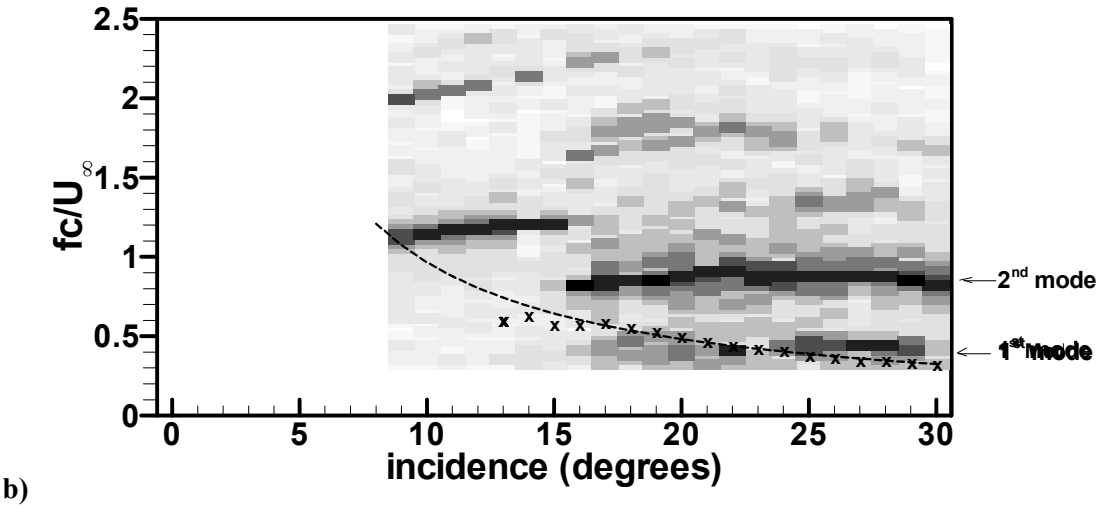

b)

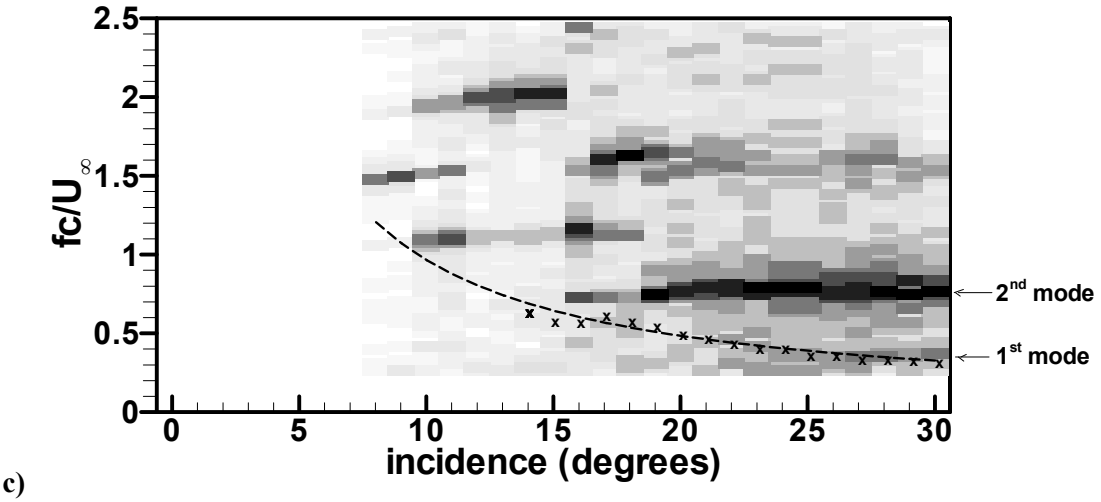

c)

Figure 3.8: **Power spectral density of the membrane oscillations for δ_0 = 0% for a) U_∞ = 5 m/s; b) U_∞ = 7.5 m/s; c) U_∞ = 10 m/s. The density is plotted as an intensity map, indicating the membrane vibration in log-scale. The symbols are the shedding frequencies in the wake measured from an equivalent rigid cambered aerofoil.**

From the spectra plot, the dominant frequency is found as a function of angle of attack for three different freestream velocities as shown in Figure 3.9 (solid lines). It is seen that, for the same mode number of two (for $\alpha \geq 20°$), the measured frequencies are slightly different for different freestream velocities. This is probably due to the change in the membrane shape, and therefore the tension.

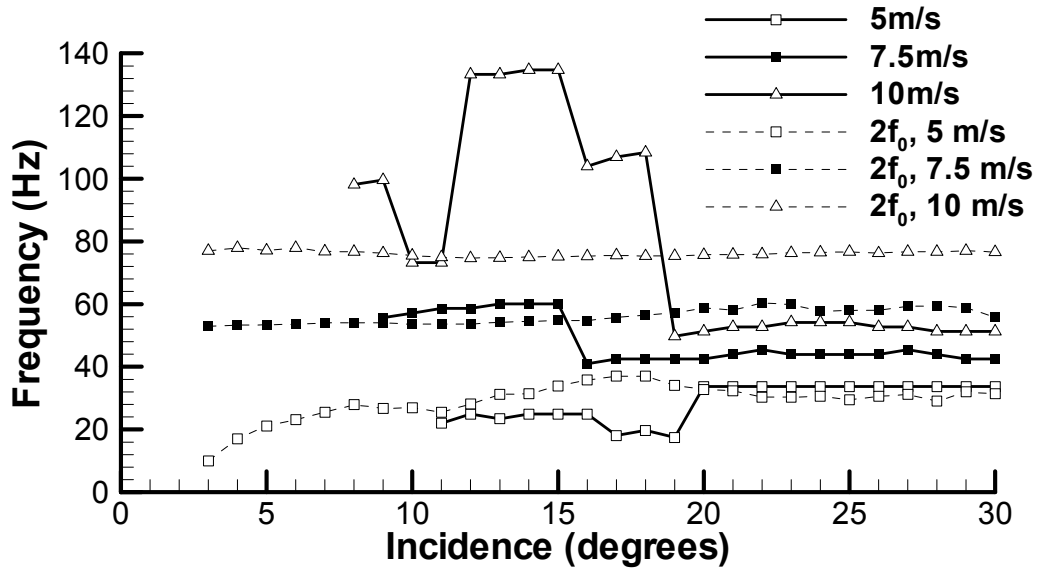

Figure 3.9: Variation of the dominant frequency of membrane oscillations as a function of angle of attack. Dash lines are the second harmonic of natural frequencies, f_0, predicted using the elastic theory and the measured mean shape of membrane.

Also shown in Figure 3.9, in dash lines, is an attempt made to predict the natural frequencies of the membrane. The natural frequencies of the membrane are estimated based on the linear elastic theory mentioned earlier in section 1.2.4:

$$f_0 = \frac{1}{2L}\left(\frac{E\,\delta}{\rho_m}\right)^{1/2} \tag{52}$$

, where L was substituted by the effective chord length of membrane (c_e = 0.137 m) and the membrane strain δ was estimated from the mean deformation. It is said earlier that at high angle of attack the second mode is always observed regardless of the freestream velocity. (The second mode can be confirmed from the standard deviation plot such as Figure 3.7-a). Therefore the analytical prediction shown is Figure 3.9 is for the second mode, $2f_0$. It is interesting that the predicted frequency is closely matched to the experimental value at the lowest freestream (U_∞ = 5 m/s)

and at high incidences. However, the difference between these two values becomes greater at higher freestream velocities. Although it is not clear whether the linear elastic theory can be justified for this highly nonlinear problem, the analytical prediction for the low freestream velocity is proved to be quite promising. However, it should be kept in mind that this theoretical prediction is valid only for vacuum. The added mass effects as well as the effects of a mean flow are not taken into account. Substantial changes in the added mass are expected in separated flows (for an oscillating circular cylinder, the added mass may even become negative). It will be shown later from the study of unsteady flow (section 3.5) that the Reynolds stress over the membrane is larger for the larger freestream velocity. This may explain the larger difference of the experimental membrane frequencies from the theoretical values. Additionally, the comparison of the Reynolds stress between the membrane and rigid aerofoil (later shown in Figure 3.19) reveals that the Reynolds stress over the membrane is significantly stronger compared to the rigid one. The information of this fluid forcing is therefore a crucial supplement to the existing elastic theory. The membrane natural frequencies were predicted successfully for low aspect ratio membranes by using this approach (Song et al. 2008a,b). However, Song et al. (2008a,b) adjusted the value of the pre-strain (by adding additional strain of around 0.05) in order to fit to the theoretical model for the camber and argued that this value is within the fabrication uncertainty. Such a large pre-strain would correspond to nearly 7.5 mm difference in length in the present setup, which would not be realistic. It is believed that the difference between the linear theory and experiments highlights the nonlinear nature of the fluid-structure interaction.

The variation of the Strouhal number $St = fc/U_\infty$ as a function of angle of attack is shown in Figure 3.10. In general, the Strouhal number is in the order of unity. This is consistent with the findings of simulations for the same geometry but at much lower Reynolds number (Gordnier 2008). It is seen that, in particular, for $\alpha \geq 20°$, the Strouhal number is close to unity in Figure 3.10. The Strouhal number increases with increasing freestream velocity at moderate incidences. Song et al. (2008a,b) also reported increasing Strouhal number with freestream velocity for a low aspect ratio wing. An alternative definition of the Strouhal number, based on

the vertical distance between the leading-edge and trailing-edge, is often used in the literature (Fage and Johansen 1927; Abernathy 1962):

$$St_{\alpha} = \frac{fc \sin \alpha}{U_{\infty}} \tag{53}$$

This modified definition of the Strouhal number is reported to be constant for flat-plates and thin aerofoils, with the values given in the range of 0.16 to 0.22 (Fage and Johansen 1927; Abernathy 1962; Miranda et al. 2005). Vortex shedding frequency in the wake of the rigid membrane (equivalent rigid cambered aerofoil) was measured with hot-wire anemometry and added to Figure 3.10. It is seen that measured Strouhal numbers are not very different from those of flat-plates and aerofoils. Also, the dashed line shows $St_{\alpha} = 0.17$, which agrees very well with our measurements at the three freestream velocities. This figure suggests that there might be coupling of the membrane oscillations with the vortex shedding from the membrane. In particular, for $\alpha \geq 20°$, where the second mode is always observed, the membrane oscillations might be coupled with the first harmonic of the natural frequency. In active flow control studies with rigid aerofoils (Miranda et al. 2005; Wu et al. 1998), it was found that vortex shedding may lock on the first harmonic or the subharmonic of the natural frequency.

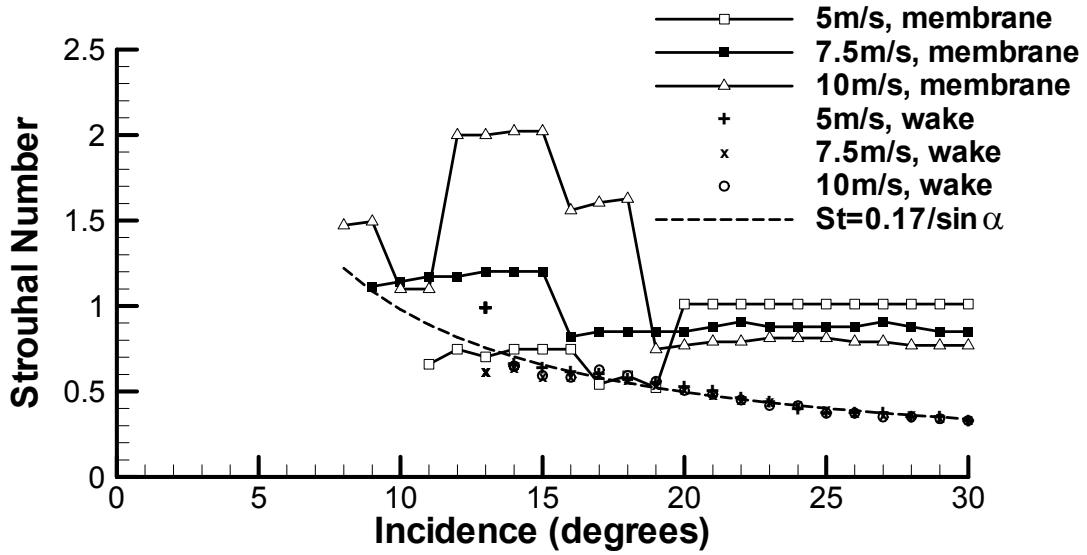

Figure 3.10: Variation of the Strouhal number of membrane oscillations as a function of angle of attack.

Finally, the maximum standard deviation of the membrane oscillations is shown as a function of angle of attack in Figure 3.11. The amplitude of the oscillations

starts to increase rapidly at a certain angle of attack and this incidence decreases with increasing freestream velocity. A local maximum is observed for α = 10° to 12°, followed by increases or decreases depending on the freestream velocity and the mode jumps. For the lowest freestream velocity (and largest Π_1), the amplitude of the oscillations is somewhat smaller at high incidences. However, for the higher freestream velocities (and smaller Π_1), the amplitude has an increasing trend at high angles of attack. This might be partly due to the shear layer getting closer to the surface at higher freestream velocities.

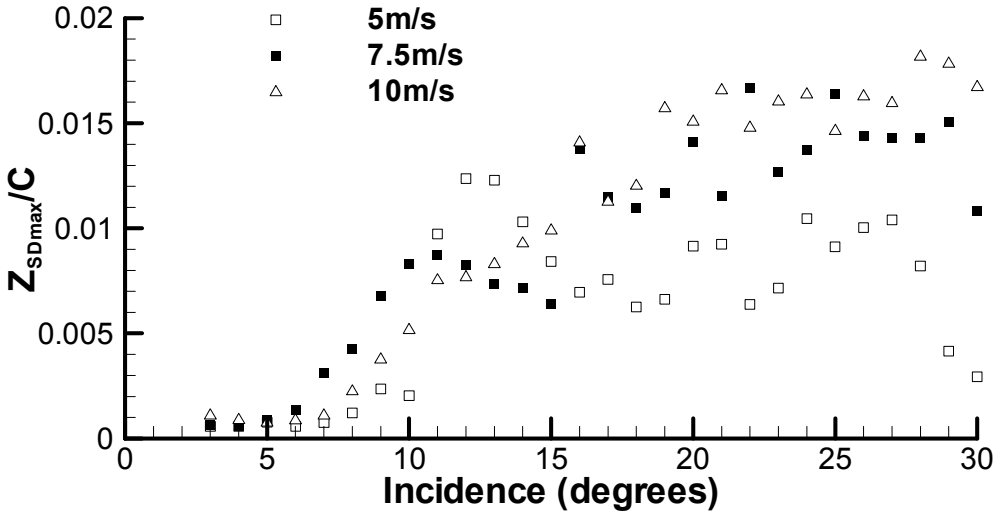

Figure 3.11: Variation of the maximum standard deviation of membrane displacement normalised by chord length, as a function of angle of attack.

3.5 UNSTEADY FLOW

Figure 3.12 shows the turbulence intensity $\overline{u'^2 + v'^2} / U_\infty^2$ in the measurement plane at different angles of attack for U_∞ = 5 m/s. The shear layer fluctuations move away from the surface with increasing angle of attack and also become stronger. Note that, for this freestream velocity, the largest membrane oscillations occur at α = 12° (see Figure 3.11) for which the shear layer is closest to the surface as seen in Figure 3.12. The velocity fluctuations become weaker and move away from the surface at very large incidences (see, for example, α = 30°) and the membrane oscillations decrease.Figure 3.13 shows a comparison of the turbulence intensity when the freestream velocity is increased from U_∞ = 5 m/s to 7.5 m/s for

$\alpha = 20°$. It is seen that the shear layer becomes closer to the surface (which is also seen in the time-averaged flow in Figure 3.6) while the magnitude of the fluctuations also increase. This explains the earlier onset of the membrane oscillations and also larger membrane oscillations at higher freestream velocities (see Figure 3.11).

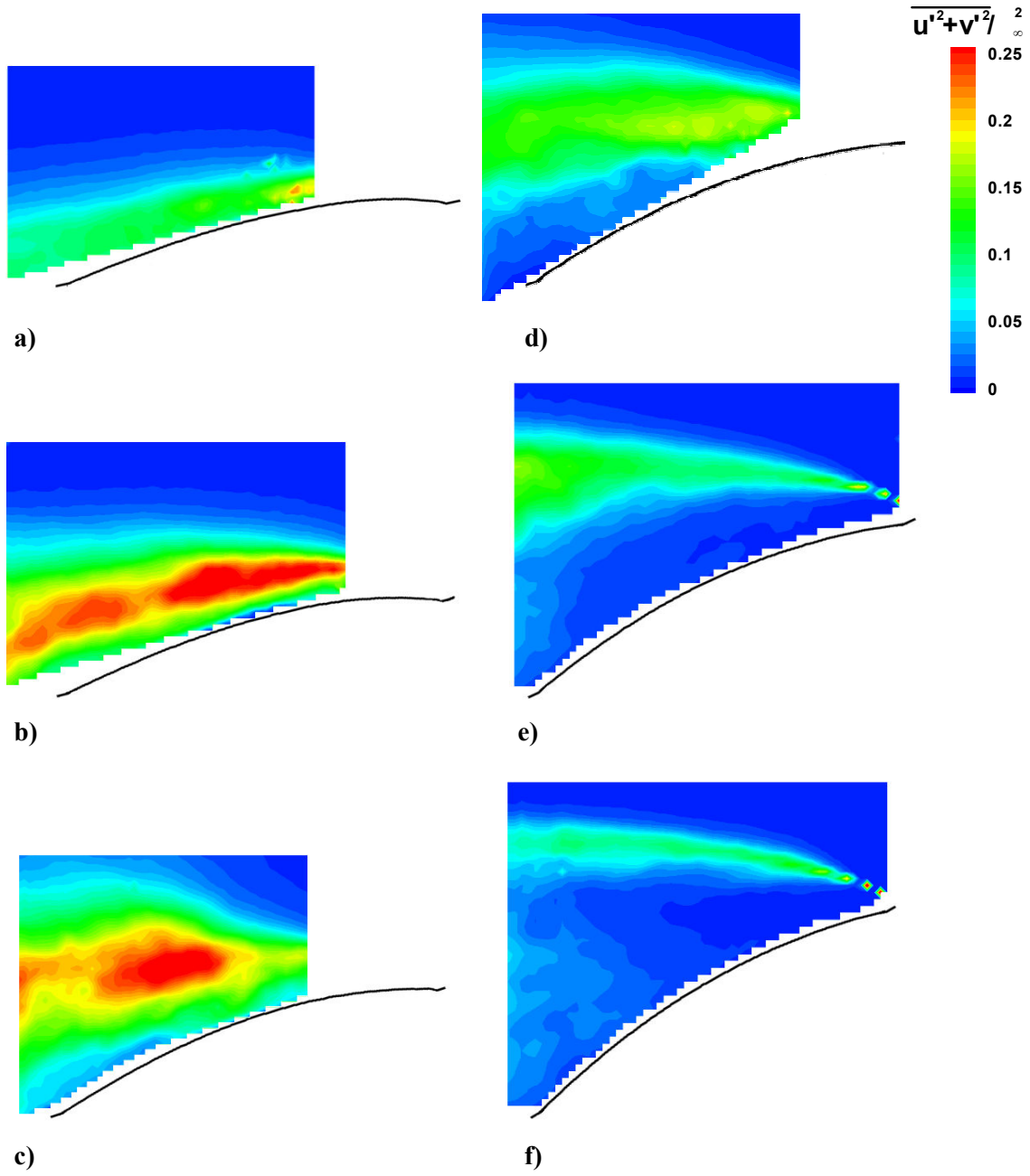

Figure 3.12: Turbulence intensity at different angles of attack, U_∞ = 5 m/s: a) α = 12°; b) α = 14°; c) α = 18°; d) α = 20°; e) α = 25°; f) α = 30°. Flow is from *right* to *left*.

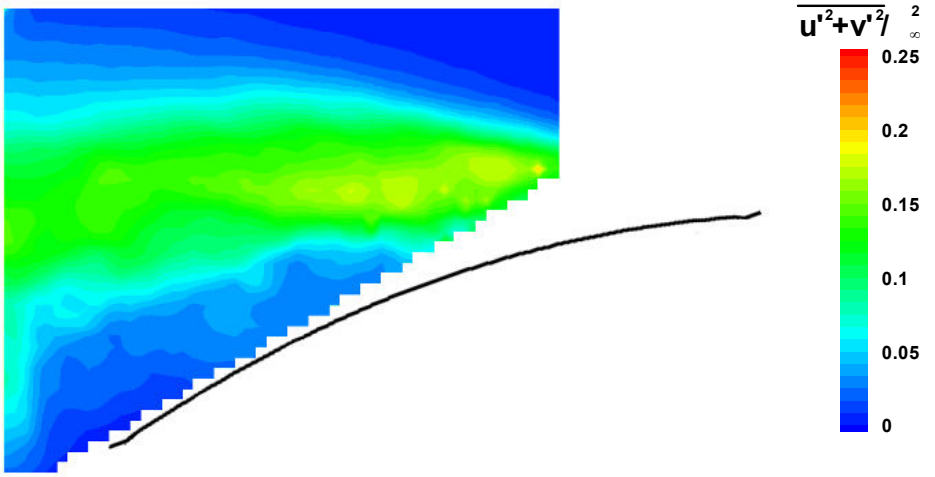

a)

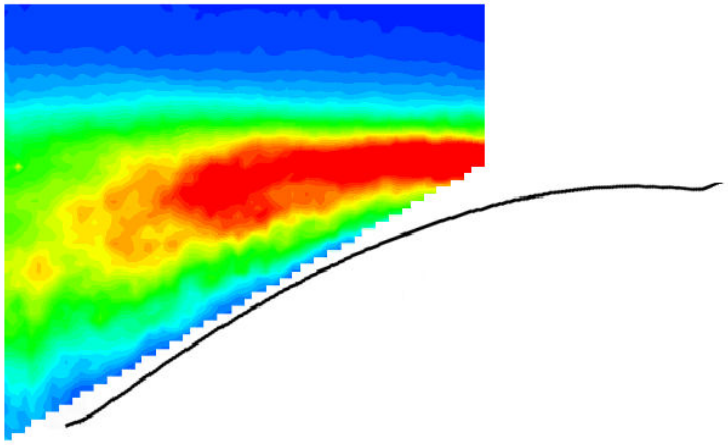

b)

Figure 3.13: Turbulence intensity at α = 20°: a) U_∞ = 5 m/s; b) U_∞ = 7.5 m/s. Flow is from *right* to *left*.

Figure 3.14 shows the Reynolds stress component as a function of angle of attack for U_∞ = 5 m/s. The peak in the Reynolds stress occurs along the shear layer where the time-averaged vorticity is maximum. The location of the maximum values of the Reynolds stress moves away from the membrane surface and downstream with increasing angle of attack. Peak magnitudes are observed for α = 14° to 18° range, then the peak value decreases at higher angles of attack. The relatively large value of the Reynolds stress observed for moderately high incidences is related to the formation of coherent structures. Examinations of the instantaneous flow fields suggest that the peak of the Reynolds stress coincides with the roll-up of the large vortices as shown in Figure 3.15 for α = 18°.

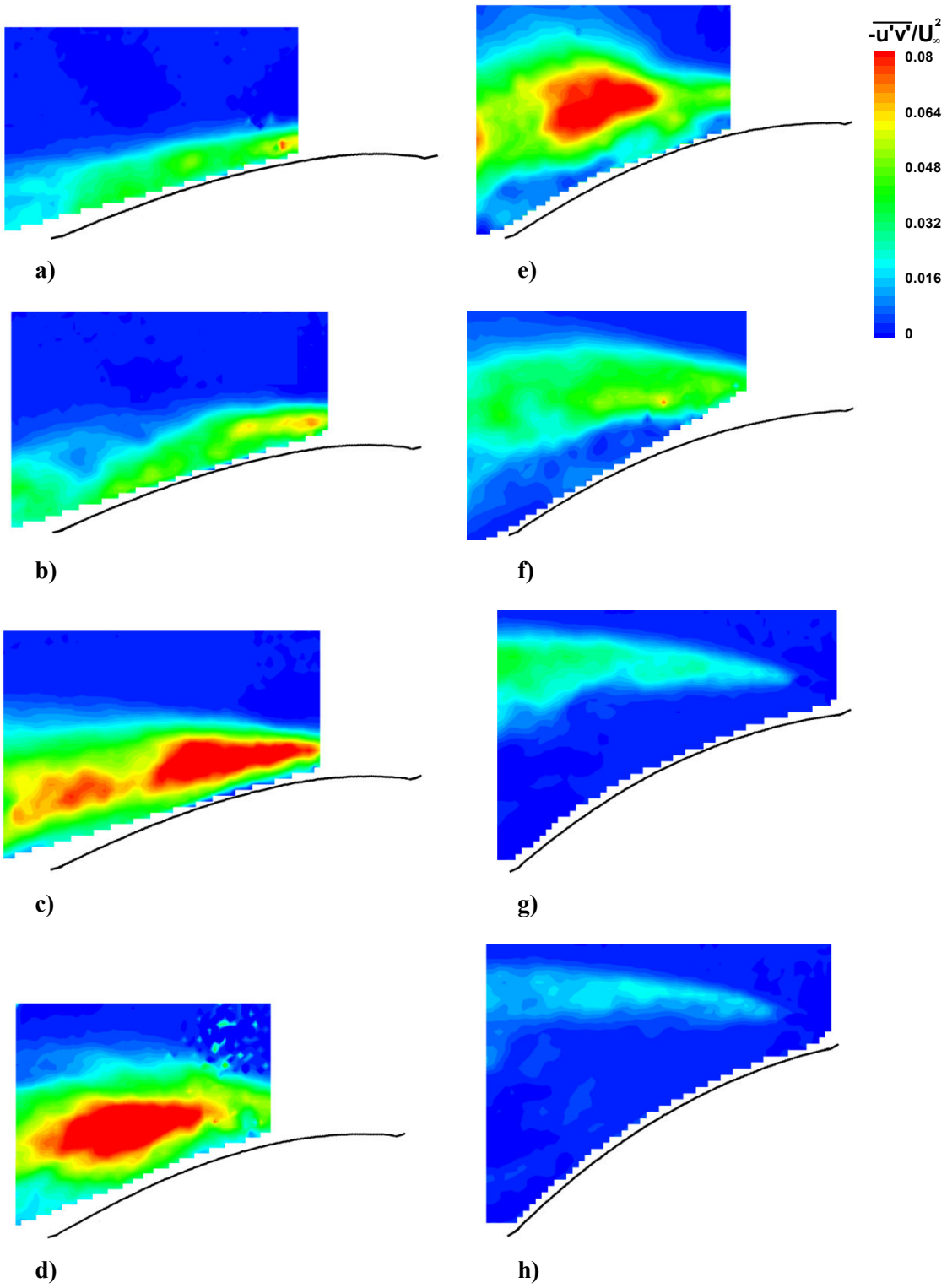

Figure 3.14: Reynolds stress at different angles of attack, U_∞=5 m/s: a) $\alpha = 12^o$; b) $\alpha = 13^o$; c) $\alpha = 14^o$; d) $\alpha = 16^o$; e) $\alpha = 18^o$; f) $\alpha = 20^o$; g) $\alpha = 25^o$; h) $\alpha = 30^o$. Flow is from *right* to *left*.

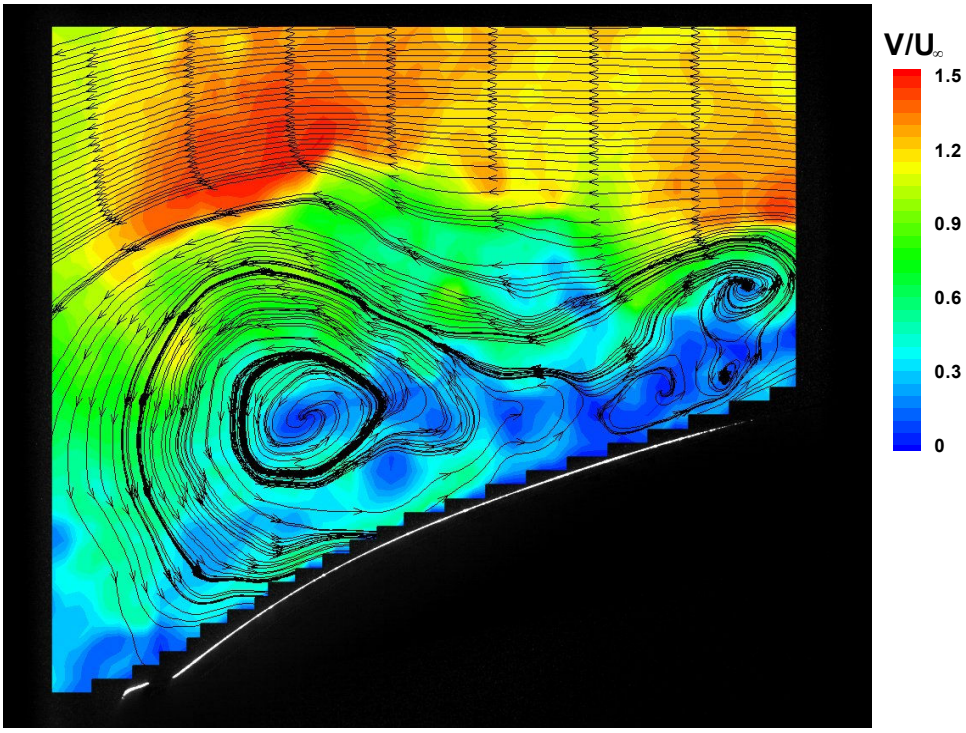

Figure 3.15: An example of instantaneous velocity magnitude and streamlines: U_∞ = 5 m/s and α = 18°. Flow is from *right* to *left*.

3.6 FLOW-MEMBRANE COUPLING

Instantaneous velocity field measured by the high speed PIV system was examined to study the coupling of the instantaneous flow with the membrane deformation. In order to demonstrate the high degree of correlation between the unsteady flow and membrane shape, both the location of the shear layer (identified as the location of maximum vorticity) and the membrane displacement were analysed for each instantaneous flow over several cycles of membrane oscillations. Figure 3.16-a shows the variation of the location of the shear layer and membrane displacement as a function of time for α = 13° and U_∞ = 5 m/s. It is seen that the location of the shear layer is highly correlated to the membrane oscillations. When the membrane displacement is maximum, the shear layer is farthest away from the surface at this chordwise location. Figure 3.16-b and Figure 3.16-c show two instantaneous flow fields at instants corresponding to the minimum and maximum displacements of membrane at 0.75c, respectively. For this angle of attack, the shear layer flapping is significant, which might be the cause of the largest membrane oscillations for this freestream velocity.

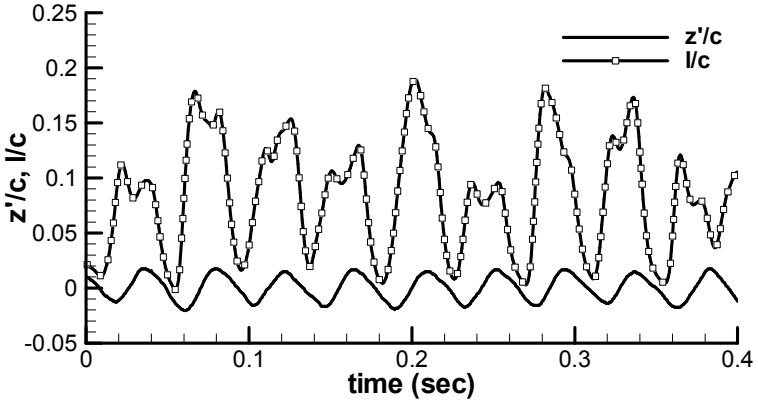

a)

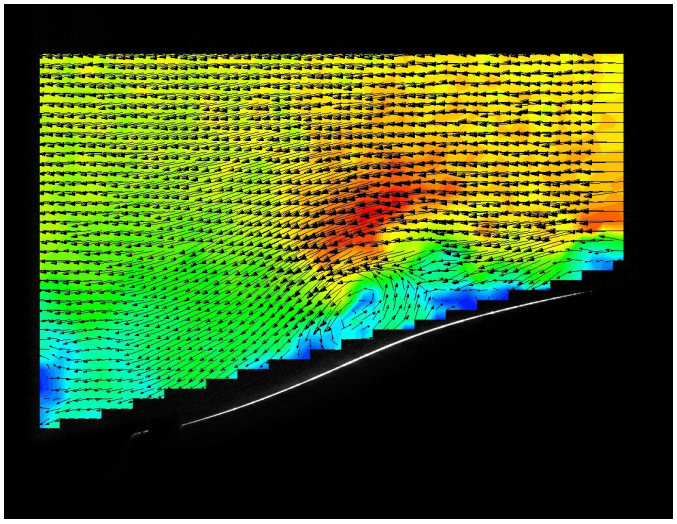

b)

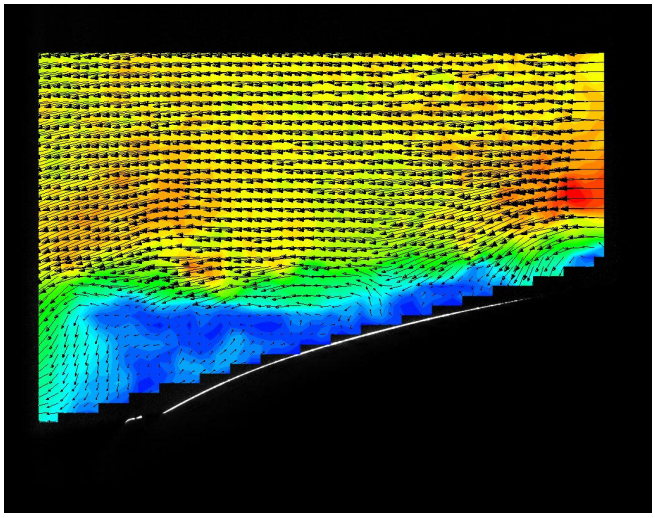

c)

Figure 3.16: **a) Time history of the locations of the shear layer and membrane as measured at 0.75c; b) Instantaneous flow field at minimum and c) maximum values of membrane displacement, U_∞ = 5 m/s, α = 13°. Flow is from *right* to *left*.**

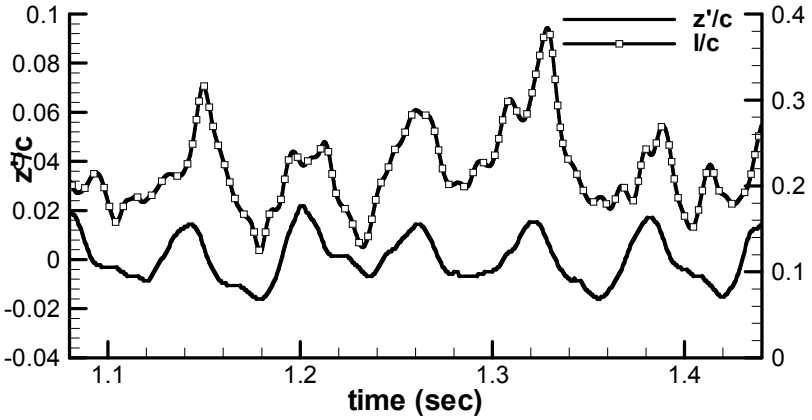

a)

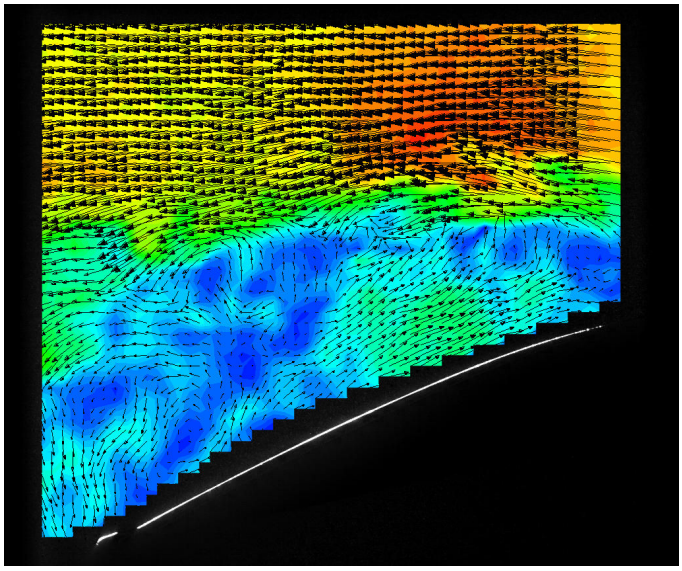

b)

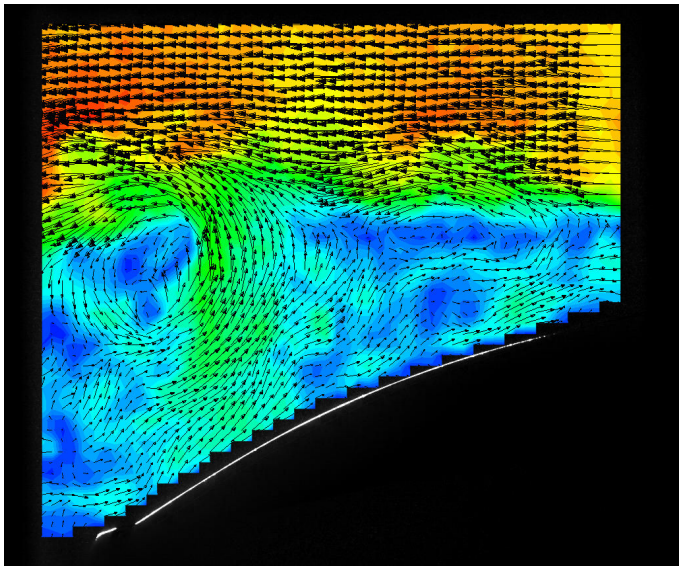

c)

Figure 3.17: **a) Time history of the locations of the shear layer and membrane as measured at 0.75c; b) Instantaneous flow field at minimum and c) maximum values of membrane displacement, U_∞ = 5 m/s, α = 18º. Flow is from *right* to *left*.**

Figure 3.17 shows similar data for a higher angle of attack (α = 18°) and U_∞ = 5 m/s. Positive correlation between the shear layer location and membrane displacement at 0.75c is similar to the case of α = 13°. Figure 3.17-b and Figure 3.17-c show two instantaneous flow fields at instants of minimum and maximum membrane displacements, respectively. At this angle of attack, the roll-up of large vortices is more evident (see also Figure 3.15).

3.7 COMPARISON OF RIGID AND MEMBRANE AEROFOILS

Figure 3.18 shows smoke flow visualisation with a high speed camera for the flexible membrane aerofoil with zero pre-strain (left column) and the rigid aerofoil (right column). For the rigid aerofoil (a curved metal sheet), the mean camber is the same as of the flexible membrane, but of course there is no vibration. This presence or absence of membrane vibrations affects the separated flow significantly. It is seen that for all incidences, the size of the separation and recirculation region is smaller for the flexible membrane. Also, at higher incidences (α = 18° and 20°), the roll-up of large vortices is evident over the flexible membrane whereas the shear layer does not exhibit large vortices for the rigid membrane. The oscillations of the membrane excite the shear layer, resulting in the roll-up of the large vortices. As the location of the shear layer (distance from the membrane surface) is smaller for the flexible membrane, this suggests that drag might be smaller and stall might be delayed compared to the rigid membrane.

Figure 3.19 shows the magnitude of the Reynolds stress for the flexible and rigid membrane aerofoils for α = 18° and 20°. It is seen that the Reynolds stress is much larger for the flexible membrane due to the membrane vibrations, which excite the shear layer and promote the roll up of the vortices.

A similar comparison of flexible and rigid membranes was made in the simulations by Gordnier (2008) at Re = 2,500. It was shown that the dynamic motion of the membrane excites the shear layer causing it to roll up sooner and to form a series of vortices. This resulted in an increase in lift and decrease in drag.

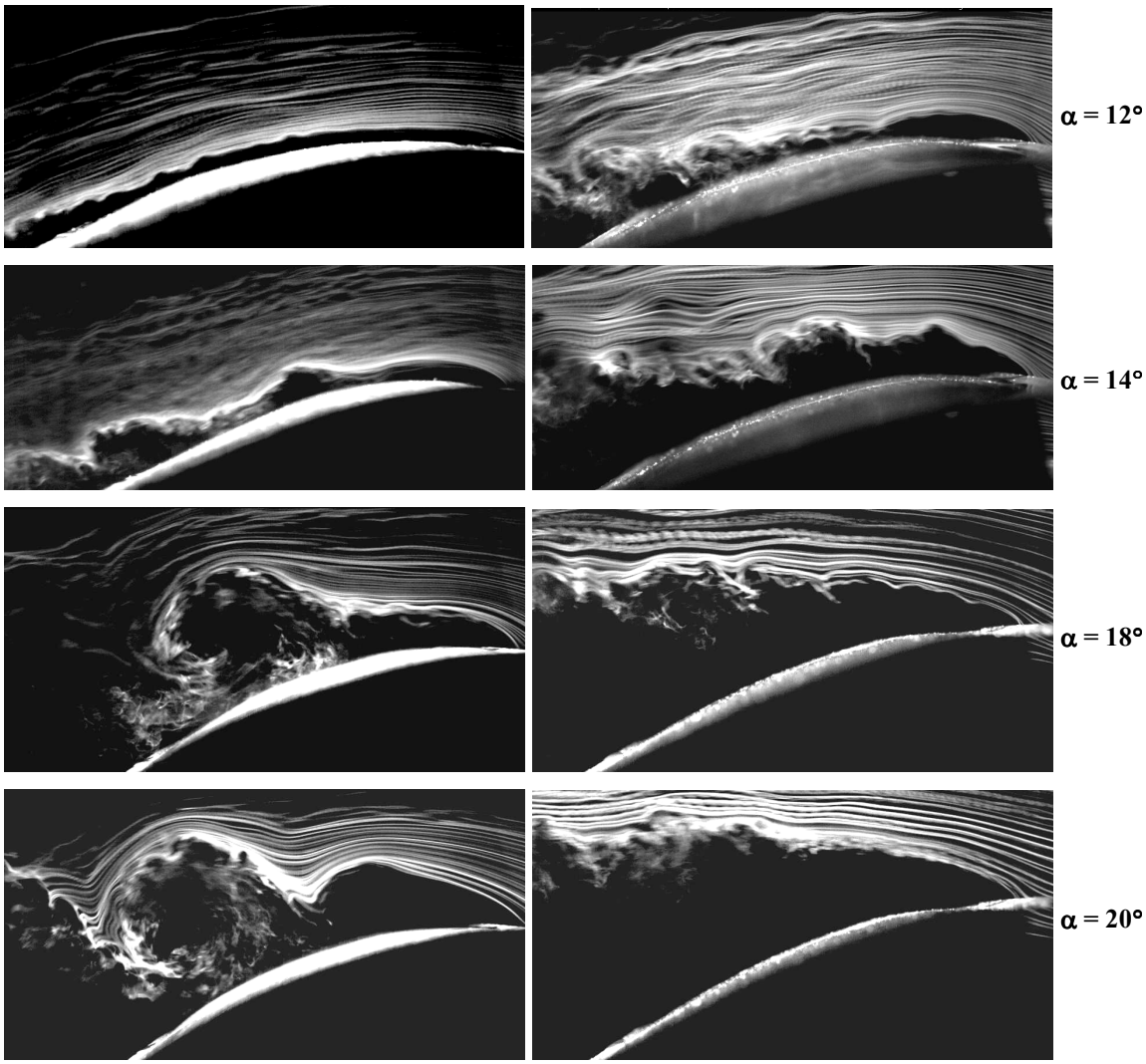

Figure 3.18: **Smoke flow visualisation with a high speed camera at different angles of attack, U_∞ = 5 m/s for: a) flexible membrane aerofoil; b) rigid aerofoil. Flow is from *right* to *left*.**

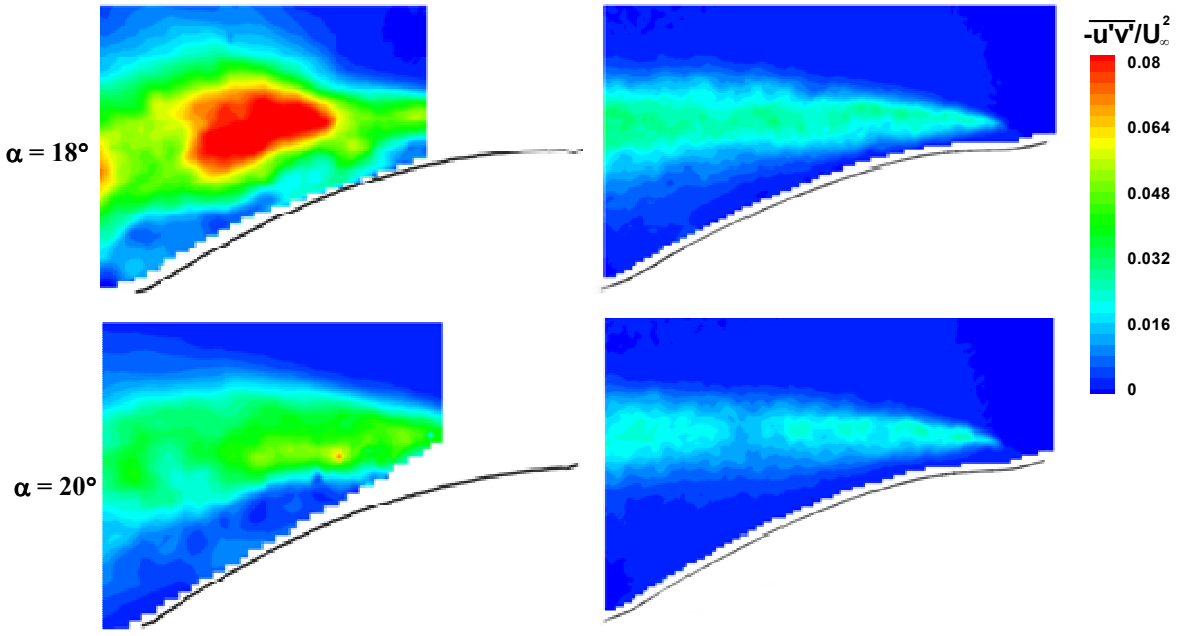

Figure 3.19: Magnitude of the Reynolds stress, U_∞ = 5 m/s for: a) flexible membrane aerofoil; b) rigid aerofoil. Flow is from *right* to *left*.

3.8 CONCLUSIONS

Unsteady aerodynamics and fluid-structure interaction of a nominally two-dimensional membrane aerofoil with zero pre-strain were investigated. Measurements of membrane shape, measurements of velocity field with a high speed PIV system, and flow visualisation were performed. The following conclusions are drawn:

- Mean membrane shape is not very sensitive to the changes in angle of attack, even though the time-averaged flow differs considerably: attached flow at small incidences, weakly separated flow at moderate incidences with the shear layer remaining close to the surface, and massively separated flows with large recirculation regions at high incidences.

- When the flow remains attached, the membrane oscillations are negligibly small. With increasing angle of attack, the amplitude of the oscillations increases rapidly around $\alpha = 10°$ for the lowest Reynolds number. The largest membrane oscillations occur when the separated shear layer remains close to the surface.

- With increasing angle of attack, the shear layer moves away from the surface. With increasing freestream velocity (increasing Reynolds number and decreasing aeroelastic parameter Π_1), the camber of the membrane increases while the separated shear layer becomes more energetic and closer to the surface. This affects the onset of the vibrations and increases the amplitude.

- Membrane oscillations with mode numbers of up to five were observed in the present experiments. The mode number increases with the freestream velocity at moderate incidences, whereas the second mode is always observed regardless of the freestream velocity for $\alpha \geq 20°$.

- The natural frequencies of the membrane were predicted based on the linear elastic theory, using the estimated strain from the mean deformation. However, added mass effects or fluid forcing information would need to be added in order to predict the response frequency more accurately.

- The variation of the Strouhal number suggests a possible coupling of membrane oscillations with the Karman vortex shedding phenomenon in the wake. In particular, for $\alpha \geq 20°$, the data suggest possibility of the membrane oscillations locking on the first harmonic of the natural frequency.

- Coupling of the membrane oscillations and separated shear layer has been demonstrated with the high degree of correlation between the membrane displacement and location of the shear layer from the analysis of instantaneous flow fields. At moderate incidences, the flapping of the shear layer is more dominant, whereas at larger incidences (α = 16° to 20°), the roll-up of large vortices is more characteristic of the flow. At even higher angles of attack (α = 25° and 30°), the shear layer has relatively low level of fluctuations and does not exhibit the roll-up of the large vortices over the aerofoil.

- The comparison of the rigid and flexible membrane aerofoils indicates that the size of the separation region is smaller for the flexible membrane. The oscillations of membrane excite the shear layer, resulting in the roll-up of the large vortices over the aerofoil. This suggests that membrane flexibility might delay the stall.

CHAPTER 4: EFFECT OF PRE-STRAIN AND EXCESS LENGTH ON AERODYNAMICS OF MEMBRANE AEROFOILS

4.1 INTRODUCTION

Several previous studies of the aerodynamic characteristics of a membrane found that a membrane equilibrium shape is only a function of a tension parameter (Thwaites 1961; Nielsen 1963; Greenhalgh et al. 1984). The previous Chapter has already shown that the membrane with no initial pre-strain ($\delta_0 = 0\%$) can develop camber for even small aerodynamic loads, and has a strong interaction with the flow. These behaviours are expected to be dependent on the membrane pre-strain and initial camber (excess length). In addition, the membrane tension contributes significantly to the natural frequency, which can directly interact with vortex shedding frequency from a leading-edge. With these in mind, this Chapter extends the previous work of the two-dimensional membrane aerofoil with zero pre-strain to the effects of membrane pre-strain and excess length on the unsteady aspects of the fluid-structure interaction. The membrane aerofoils with different initial strains of $\delta_0 = 2.5\%$, $\delta_0 = 5\%$ and excess lengths of $\varepsilon = 2.5\%$, $\varepsilon = 5\%$ were investigated experimentally. The similar approach (such as the membrane shape visualisation, velocity measurements, and smoke visualisation) to that of the previous Chapter was employed.

4.2 MEAN SHAPE OF MEMBRANE

Figure 4.1 shows the maximum camber of the time-averaged membrane shape for different membrane pre-strains and excess lengths as a function of angle of attack at different freestream velocities. Note that the smallest angle of attack shown for a given aerofoil corresponds to the onset of the bistable instability. For the lowest freestream velocity U_∞ = 5 m/s, the maximum camber increases gradually up to a moderate incidence, then stays roughly constant for the aerofoils with nonzero pre-strains. For zero pre-strain and excess length cases, the changes in maximum camber are small as the angle of attack is varied, which is consistent with the simulations by Gordnier (2008). As expected, the largest maximum camber is observed for the aerofoils with excess length. However, the difference between the two aerofoils with different excess length appears to be small. With increasing freestream velocity to U_∞ = 7.5 m/s and 10 m/s, the maximum camber increases for all aerofoils. The observations are very similar for all speeds. The trend of the location of the maximum camber is similar to that of the previous Chapter with zero pres-strain. It is located at about the mid-chord point for small incidences, and tends to move forward as the angle of attack increases up to a certain incidence, and tends to move back at higher angles of attack. The location of the maximum camber is only slightly sensitive to the membrane pre-strain and excess length ratio, and is not very sensitive to the freestream velocity.

To observe the camber as a function of the membrane pre-strain and excess length, the range of camber over the tested incidences are plotted against these pre- values, for three freestream velocities as shown in Figure 4.2-a. It is seen that even though the camber is only slightly dependent of angle of attack (as also seen from the previous figure), it is greatly influenced by the pre-strain/excess length values. In addition, the dependency of the rise in camber on the freestream velocities is clearly seen in this figure. For higher freestream velocity, the larger dynamic pressure is expected to cause larger tension adding strain to the membrane, resulting in the larger camber. Figure 4.2-b shows the slope of camber as a function of pre-strain/excess length calculated at each pre-strain/excess length interval for each freestream velocity. It is seen that as the pre-strain/excess length becomes more positive, the camber slope is positive and increases up until ε =

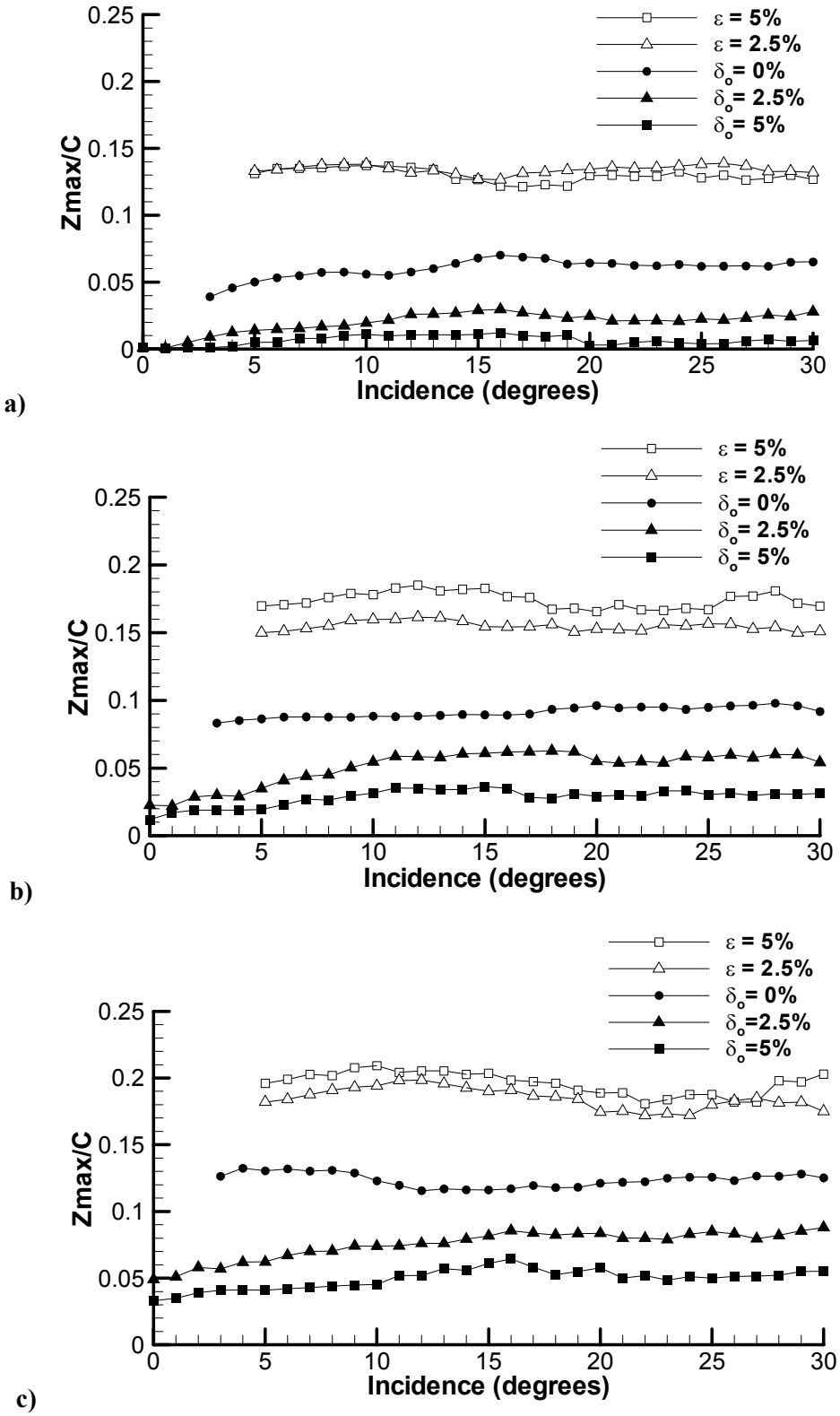

Figure 4.1: **Variation of maximum camber as a function of incidence for different pre-strains and excess lengths for: a) U_∞ = 5 m/s; b) U_∞ = 7.5 m/s; c) U_∞ = 10 m/s.**

2.5%. The trends of the rise in camber slope are quite similar for all freestream velocities. For each freestream velocity, the rise in camber can be attributed to the fact that the membrane with lower pre-strain (more positive) has less resistance to aerodynamic load.

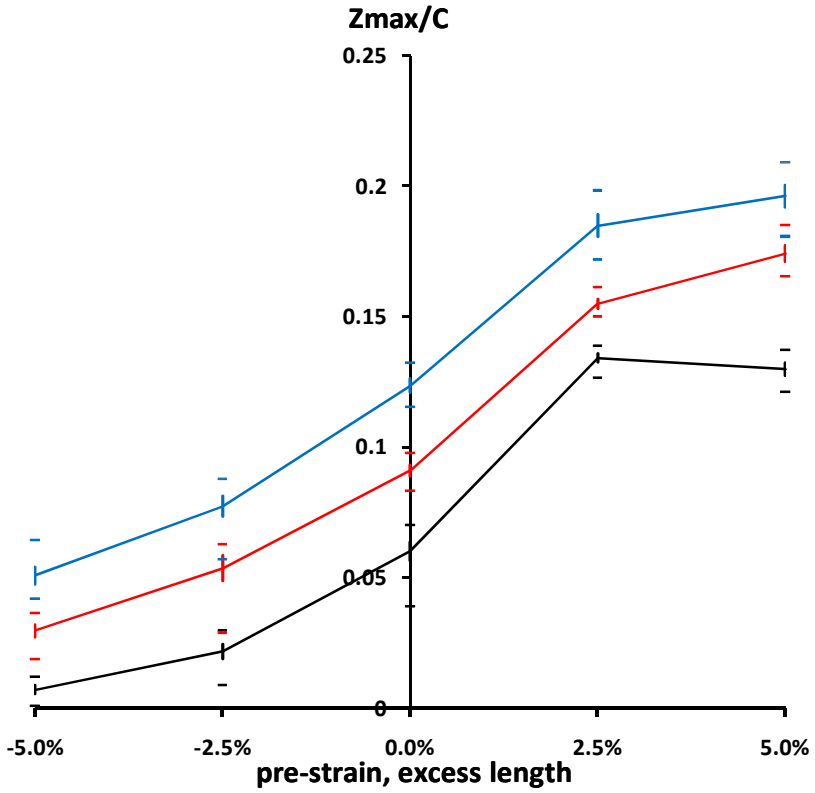

a)

	camber slope		
pre-strain/excess length	5 m/s	7.5 m/s	10 m/s
-5% to -2.5%	0.59	0.96	1.06
-2.5% to 0%	1.54	1.50	1.85
0% to 2.5%	2.96	2.55	2.45
2.5% to 5%	-0.17	0.77	0.45

b)

Figure 4.2: **a) The range of camber over incidences as a function of different pre-strain/excess length for three freestream velocities. The negative percentage values represent the pre-strains, whereas the positive values represent the excess lengths in this figure. The horizontal bars indicate the range of minimum and maximum camber over tested angles of attack. The solid lines connect the means of the cambers over tested incidences, where the vertical bars indicate standard deviations; b) The slope of camber as a function of pre-strain/excess length calculated at each pre-strain/excess length interval for each freestream velocity.**

As mentioned earlier, it should be noted that as the excess length value gets higher beyond ε = 2.5%, the camber slope values decrease. In particular at the lowest freestream velocity (U_∞ = 5 m/s) where the camber slope becomes negative. For this case, considering the larger mass of the membrane with excess length, such relatively low dynamic pressure might only be sufficient for the membrane to form a positive camber but not to produce tension. (The observation during the experiment revealed that when adjusting freestream velocity in a wind tunnel by increasing it from zero, the camber of the membrane with excess length remained negative at the freestream close to zero). This is also confirmed by a very small time-averaged strain at the lowest freestream velocity shown in Figure 4.3, in which case the membrane could behave just like an inextensible yet flexible camber. This may indicate the limitation of using the membrane with excess length at low freestream velocity. However, at larger freestream velocities (U_∞ = 7.5 and 10 m/s) the camber slopes are still positive. This implies that the self-adaptive camber feature of the membrane with large excess length (beyond the available data) still looks promising but only at sufficiently high freestream velocity.

The time averaged strain is shown in Figure 4.3. The aerofoils with excess length show larger time-averaged strain than the aerofoils with pre-strain at higher freestream velocities. This is particularly obvious at the highest freestream velocity, U_∞ = 10 m/s. The strain rate is very similar for aerofoils with δ_0 = 0%, ε = 2.5% and 5%. The strain increases with the freestream velocity for all aerofoils, but the rate of increase of strain with freestream velocity is larger for the aerofoils with δ_0 = 0%, ε = 2.5% and 5%.

These three different freestream velocities also represent three different regimes for the membrane tension. As the membrane tension is proportional to the total strain, $\overline{T} = E(\delta_0 + \overline{\delta})t$, it is seen that, for U_∞ = 5 m/s, the tension is dominated by the pre-strain. The membrane tension is much larger for δ_0 = 2.5% and 5% compared to other cases. With increasing freestream velocity to U_∞ = 7.5 m/s, the aerofoils with no pre-strain show a large increase in tension, although the tension is still larger for those with pre-strain. Eventually, at the largest freestream velocity U_∞ = 10 m/s, the membrane tension reaches similar levels for all cases. In terms of the tension coefficient, it decreases with increasing freestream velocity.

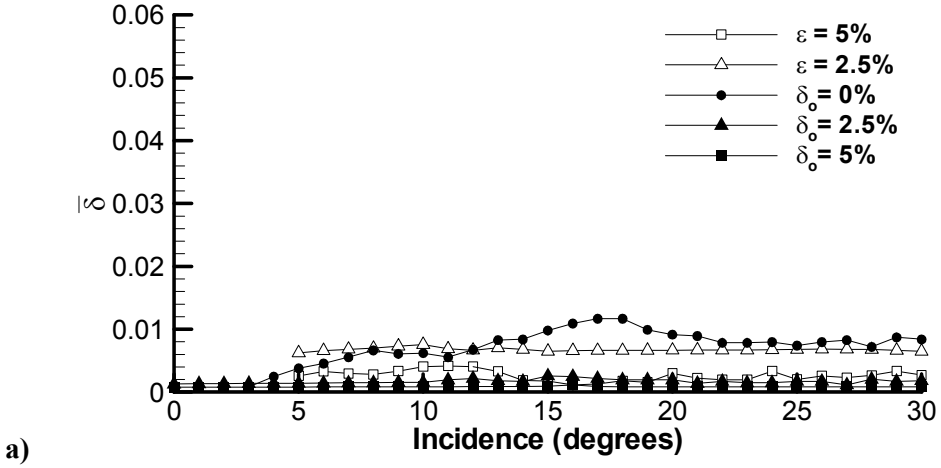

a)

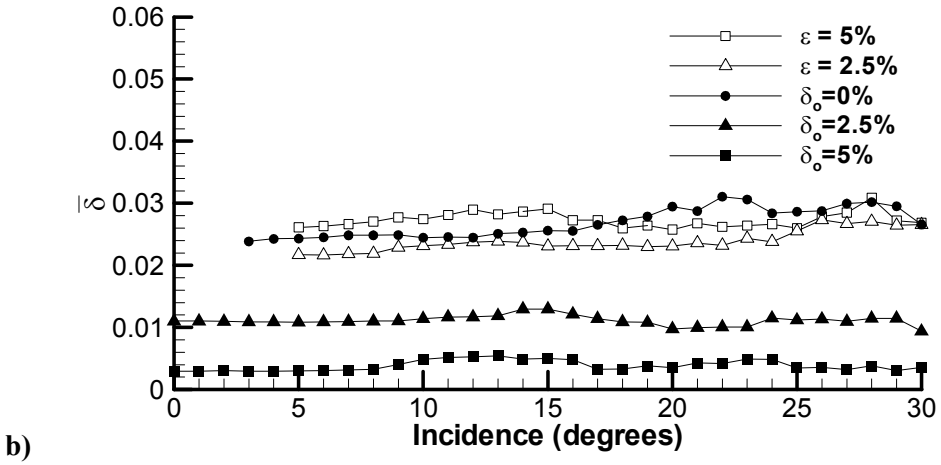

b)

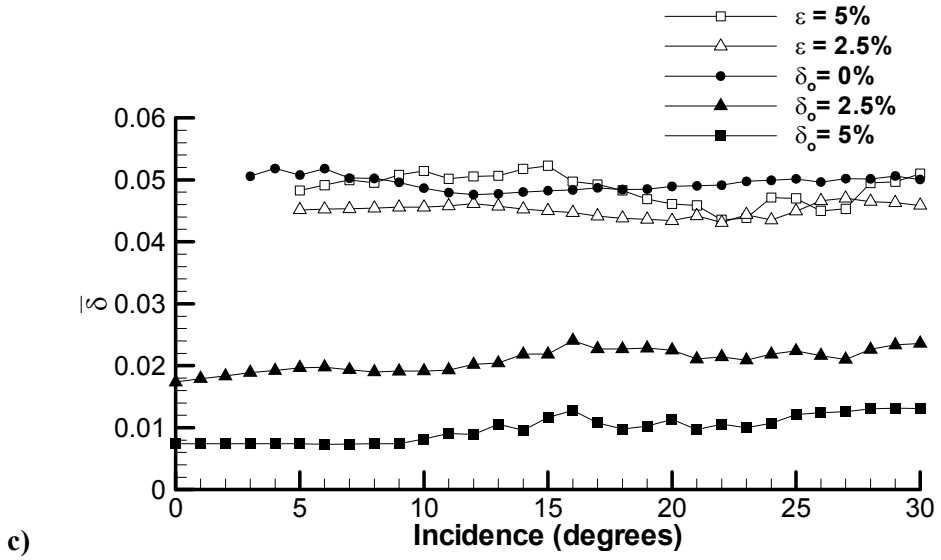

c)

Figure 4.3: **Variation of time-averaged strain as a function of incidence for different pre-strains and excess lengths for: a) U_∞ = 5 m/s; b) U_∞ = 7.5 m/s; c) U_∞ = 10 m/s.**

4.3 MEAN FLOW

Figure 4.4 shows the magnitude of the time-averaged velocity and streamlines for different aerofoils with pre-strain and excess length. Note that the flow is from right to left. In this figure, for each aerofoil, the mean flow is shown for $\alpha = 12°$ (left column) and $\alpha = 20°$ (right column). For the lowest freestream velocity, $U_\infty =$ 5 m/s, it is shown that the shear layer gets closer to the membrane surface and separation is delayed as the camber of the aerofoil increases due to the excess length. For $\delta_0 = 0\%$ and $\alpha = 12°$, even though the separation takes place at the leading-edge, the shear layer remains close to the membrane surface. For nonzero pre-strain, the shear layer moves away from the surface as the separation region becomes larger. In summary, the aerofoils with pre-strain have large flow separation regions, whereas the aerofoils with excess length, hence large camber, exhibit small separated regions. For all aerofoils, a comparison of left and right columns shows that the separation region becomes larger at $\alpha = 20^o$, as expected.

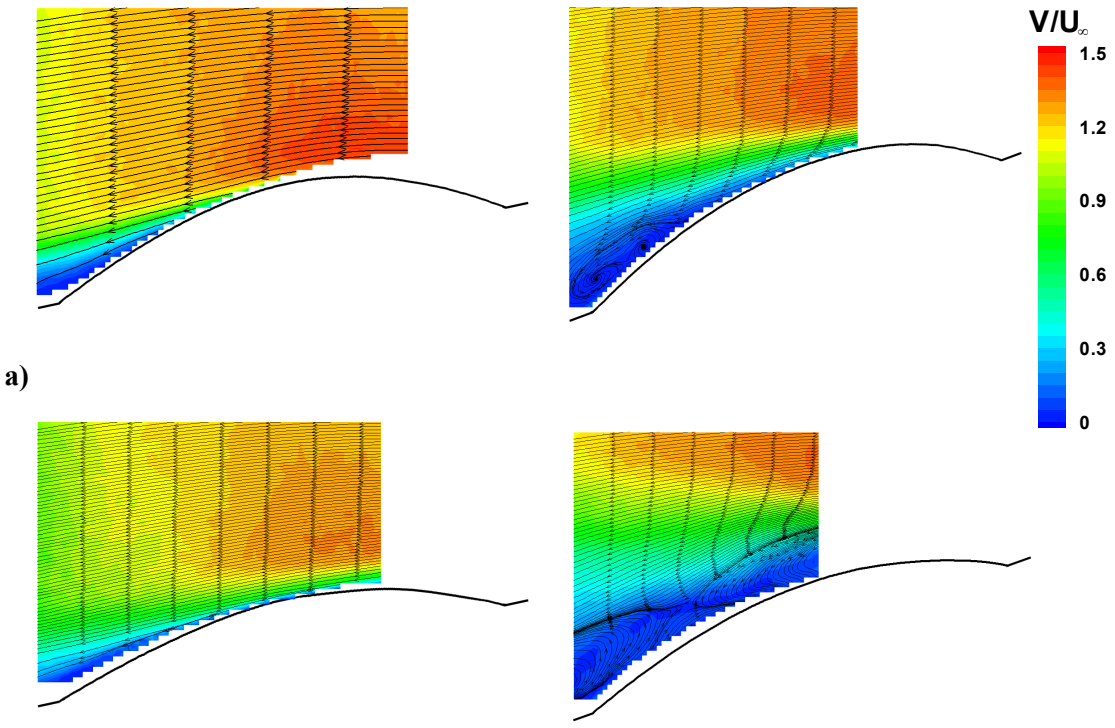

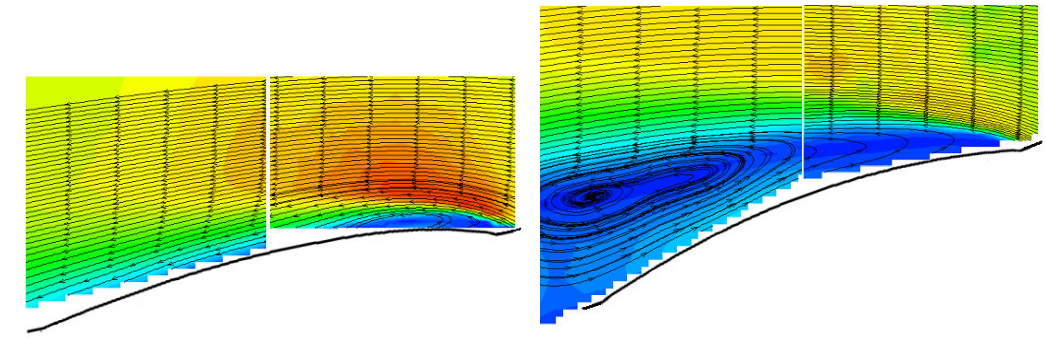

c)

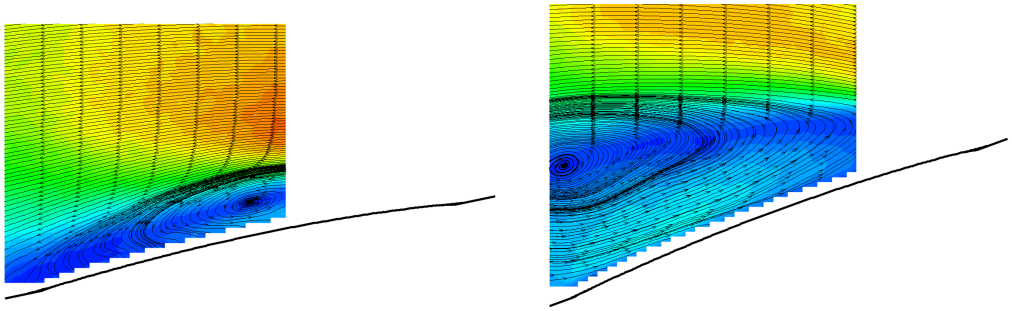

d)

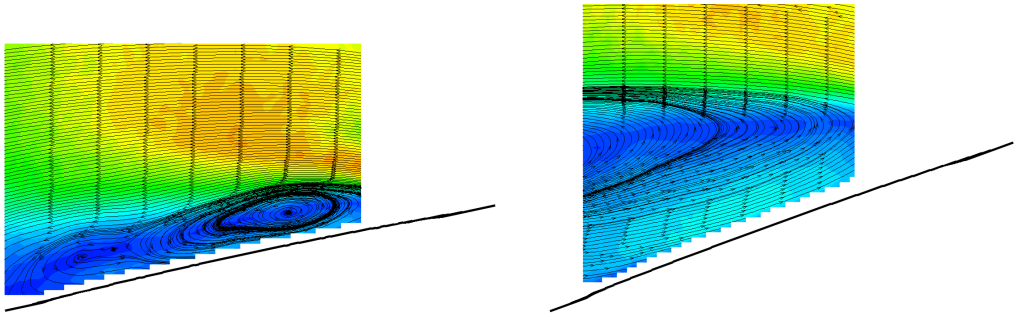

e)

Figure 4.4: **Magnitude of the time-averaged velocity and streamlines at U_∞ = 5 m/s (left: $\alpha = 12^o$, right: $\alpha = 20^o$) for: a) ε = 5%; b) ε = 2.5%; c) δ_0 = 0%; d) δ_0 = 2.5%; e) δ_0 = 5%. Flow is from *right* to *left*.**

Figure 4.5 shows a comparison of the mean flow for U_∞ = 5 m/s (left column) and U_∞ = 7.5 m/s (right column) for various aerofoils with pre-tension and excess length. For the angle of attack $\alpha = 20^o$, the aerofoils at the larger freestream velocity (U_∞ = 7.5 m/s) exhibit larger cambers and smaller separated regions. This is also consistent with the previous results in Chapter 3 which reported the trend of shear layer getting closer to the membrane surface as the camber increases.

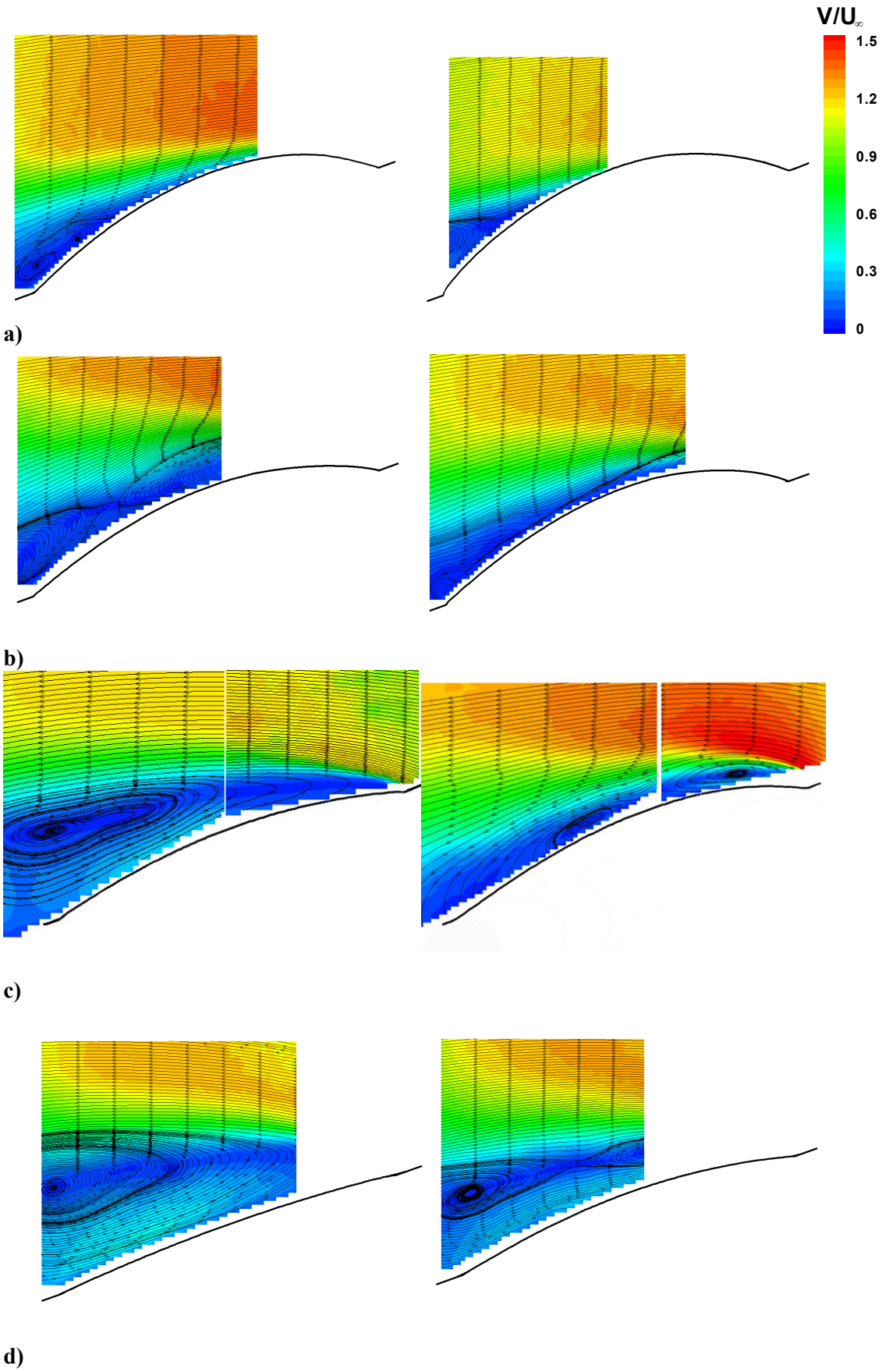

Figure 4.5: **Magnitude of the time-averaged velocity and streamlines at $\alpha = 20^{o}$ (left: $U_{\infty} = 5$ m/s, right: $U_{\infty} = 7.5$ m/s) for: a) $\varepsilon = 5\%$; b) $\varepsilon = 2.5\%$; c) $\delta_0 = 0\%$; d) $\delta_0 = 2.5\%$. Flow is from *right* to *left*.**

4.4 MEMBRANE OSCILLATIONS

Figure 4.6 summarises various regimes based on the observations of the membrane oscillations for different aerofoils with pre-strain and excess length. In the steady regime, where membrane oscillations are insignificant, the flow remains attached for small incidences. In some cases, such a steady regime was also observed at high angles of attack, which is likely to be due to the shear layer being far away from the membrane. In the unsteady regime, membrane oscillations are significant, and corresponding vibration modes and frequencies can be easily detected. In the bistable regime, which is observed for small angles of attack near zero, the bistable instability (luffing) occurs and the membrane can easily switch from positive to negative camber. It is seen in Figure 4.6 that the bistable regime is more dominant for aerofoils with excess length. The onset of the membrane vibrations also occurs at a slightly larger angle of attack for aerofoils with excess length.

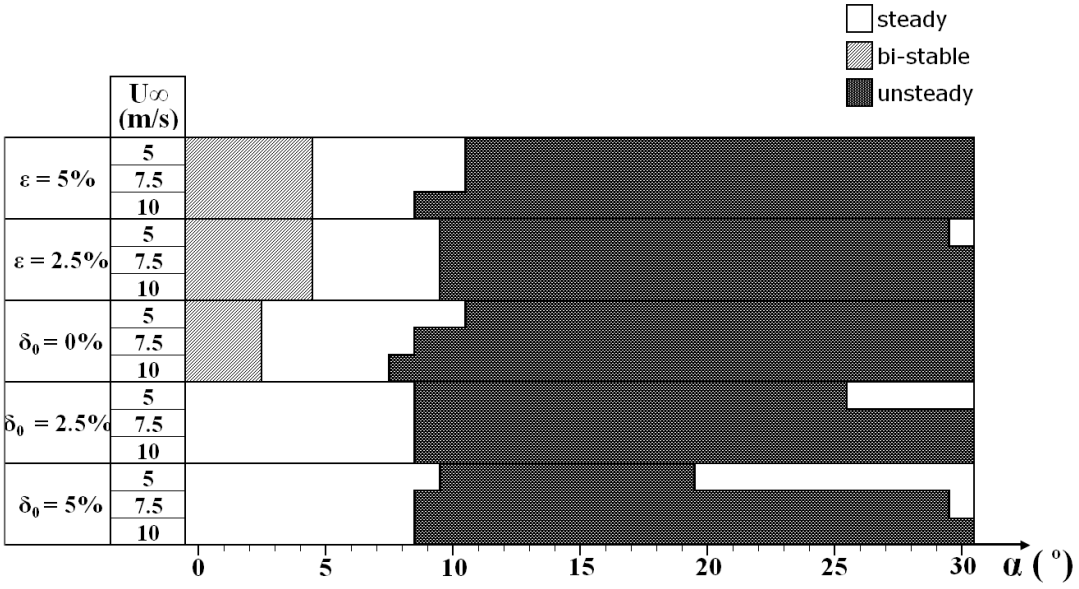

Figure 4.6: Membrane regimes as a function of incidence at different freestream velocities for different pre-strains and excess lengths.

Figure 4.7 - Figure 4.10 show the power spectral density of the membrane displacement (at the chordwise location where the standard deviation of the membrane displacement was maximum), as a function of Strouhal number, fc/U_∞, and angle of attack for $\delta_0 = 5\%$, $\delta_0 = 2.5\%$, $\varepsilon = 2.5\%$ and $\varepsilon = 5\%$ respectively. These plots show the frequencies at which large amplitudes of vibrations (shown

with the dark shades, in log-scale) take place for each incidence. In general, aerofoils with excess length and zero pre-strain (shown in Figure 3.8) have larger amplitude oscillations compared to the aerofoils with nonzero pre-strain. It is seen that the vibration occurs at certain modes. Figure 4.7 - Figure 4.10 show that the aerofoils with pre-strain exhibit the first and second modes predominantly. The aerofoils with excess length tend to have higher mode numbers than those with pre-strain at all incidences. For all freestream velocities and all aerofoils, there are certain incidences where there are jumps in the dominant mode. In particular, a change to the second mode at high incidences is observed.

The general trend for aerofoils with zero or excess length is that the higher modes are observed at moderate incidences ($\alpha \geq 10°$) when noticeable oscillations start. The separation is typically delayed for these aerofoils (see Figure 4.4 for $\alpha = 12°$). It is likely that the membrane vibrations couple with the most unstable frequencies of the shear layer. Although the natural frequency of the shear layer instabilities for rigid aerofoils was not measured in this investigation, we expect that the natural frequency of the separated shear layer is higher than the shedding frequency in the wake. Wu et al. (1998) estimates that the ratio of the shear layer frequency to the wake shedding frequency is 6.6 for NACA 0012, which provides an estimate of $fc/U_\infty \cong 2.5$ for this aerofoil. In the present investigation, we obtain $fc/U_\infty = 2$ to 3, if the same ratio of the frequencies is used. On the other hand, at higher angles of attack, flows are typically separated at the leading-edge (see Figure 4.4 for $\alpha = 20°$) and the membrane appears to couple with the wake instabilities as will be discussed further later on.

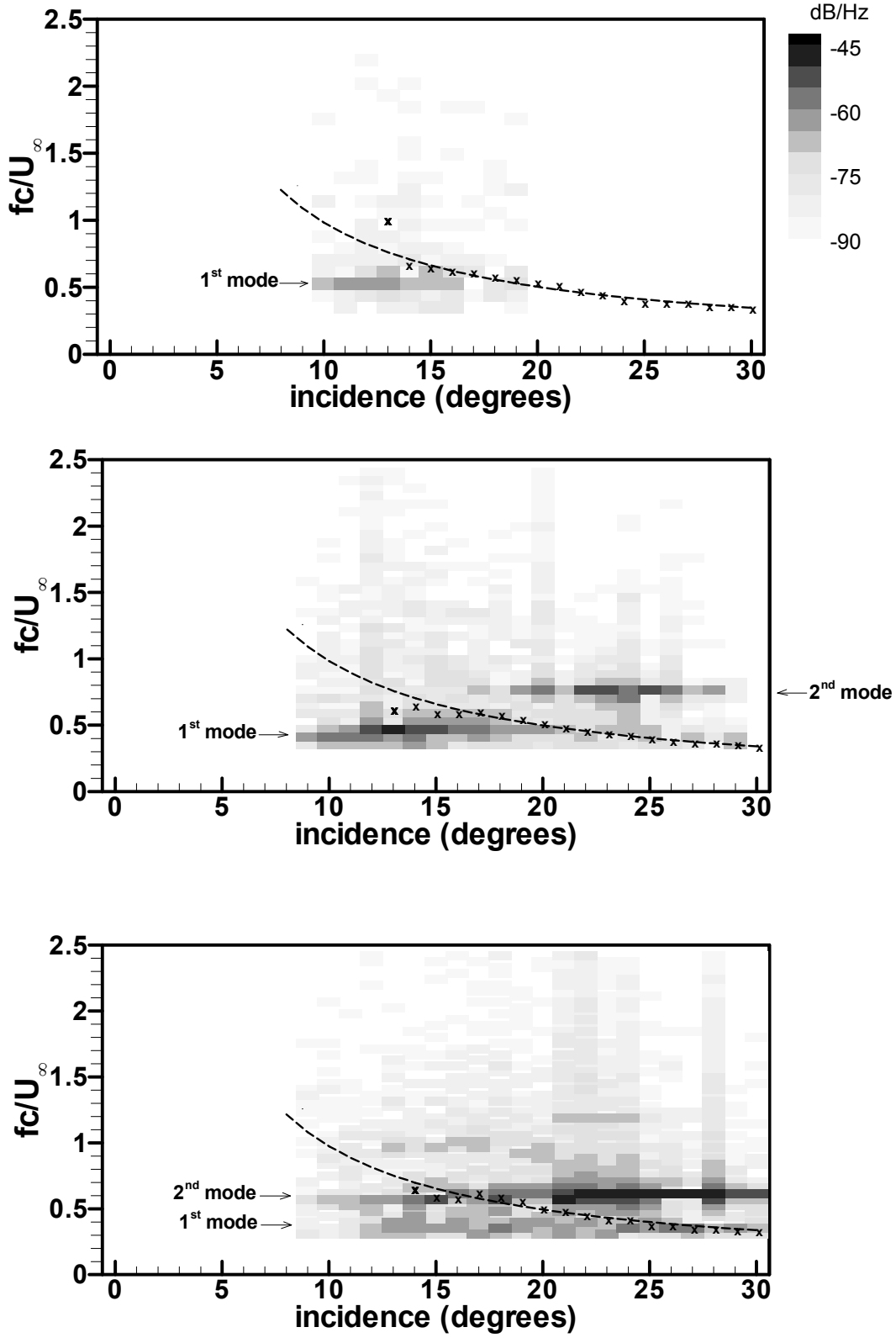

Figure 4.7: **Power spectral density of the membrane oscillations as a function of angle of attack for δ_0 = 5% for: a) U_∞ = 5 m/s; b) U_∞ = 7.5 m/s; c) U_∞ = 10 m/s. The density is plotted as an intensity map, indicating the membrane vibration in log-scale.**

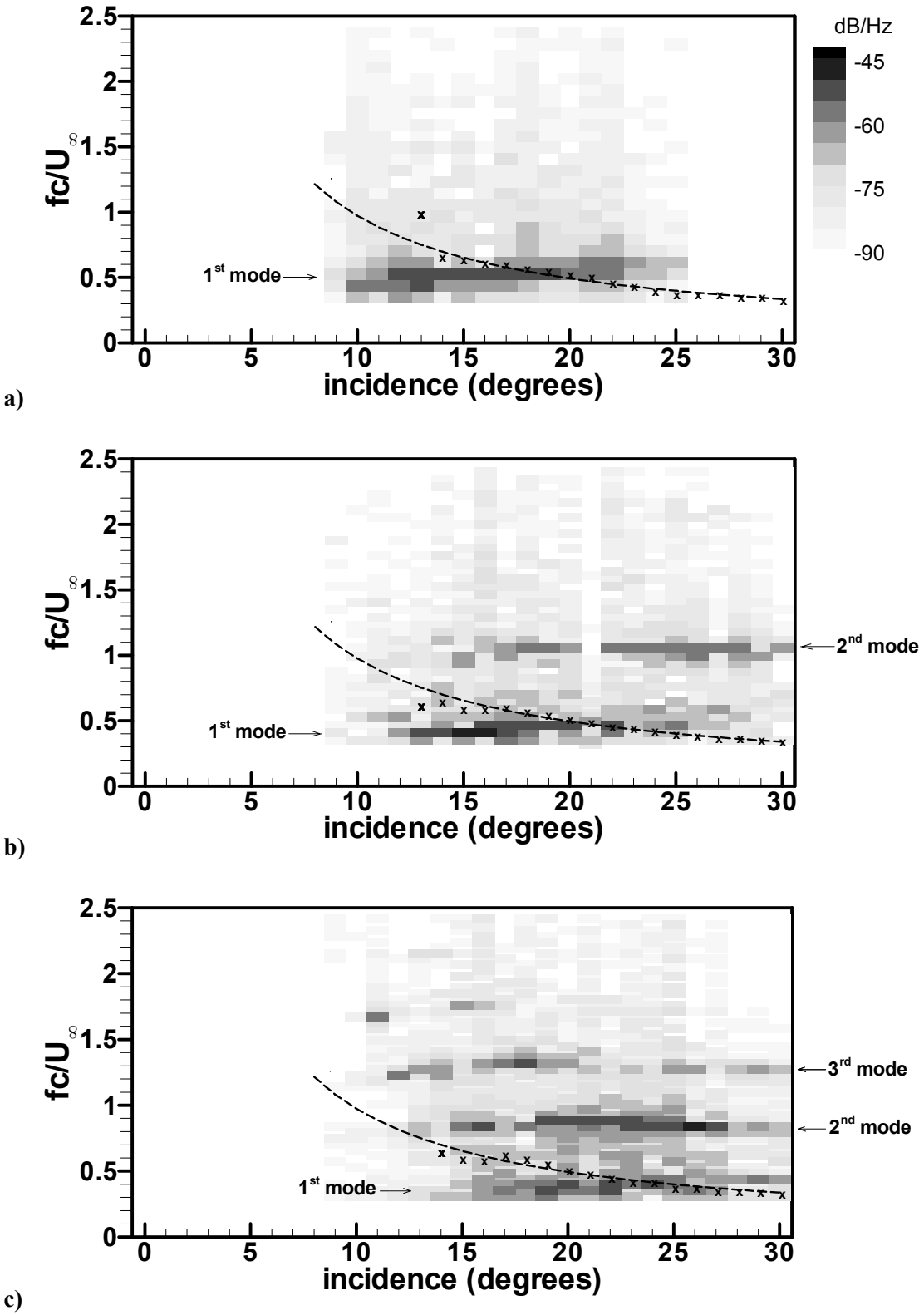

Figure 4.8: **Power spectral density of the membrane oscillations as a function of angle of attack for δ_0 = 2.5% for: a) U_∞ = 5 m/s; b) U_∞ = 7.5 m/s; c) U_∞ = 10 m/s. The density is plotted as an intensity map, indicating the membrane vibration in log-scale.**

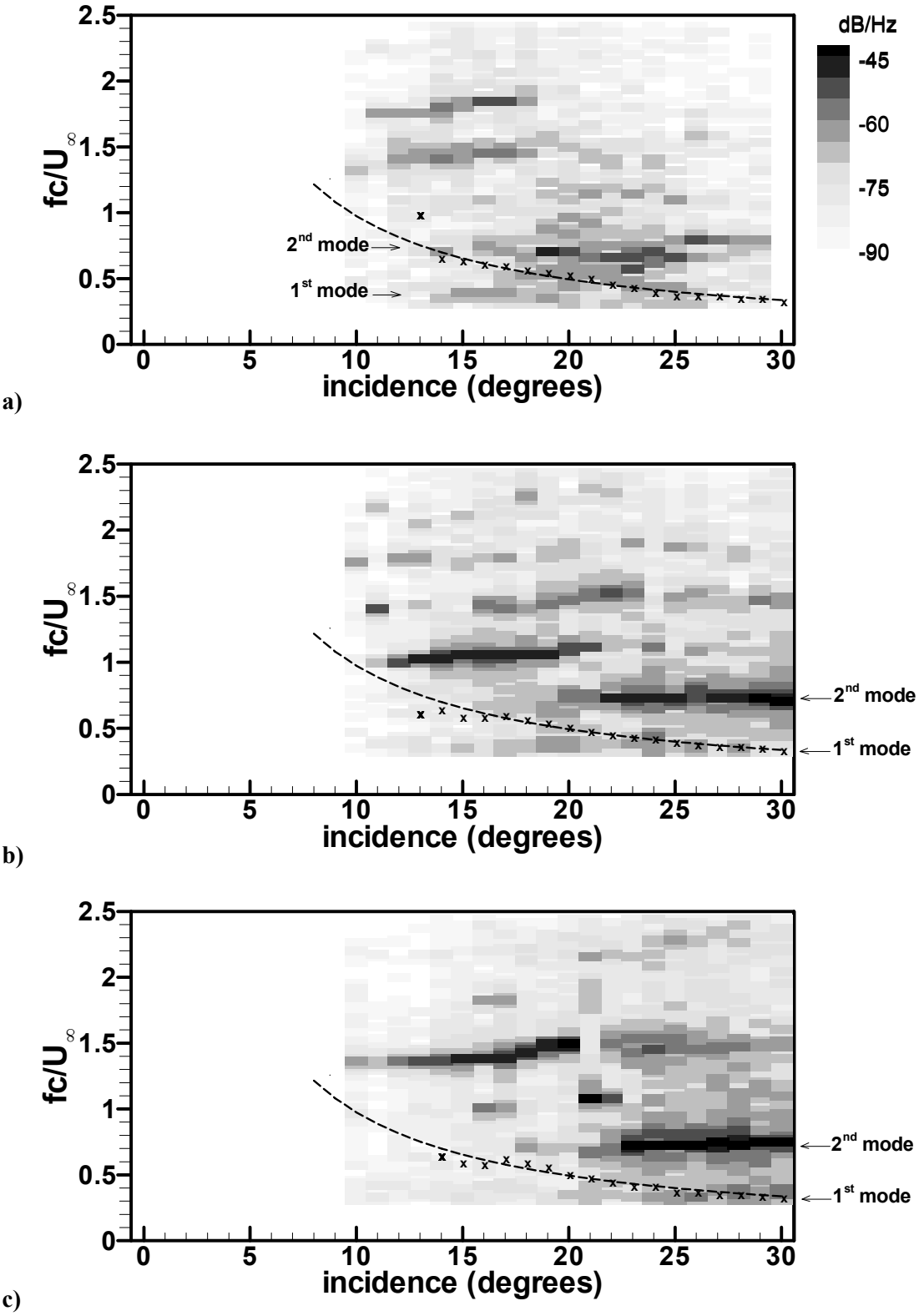

Figure 4.9: **Power spectral density of the membrane oscillations as a function of angle of attack for ε = 2.5% for: a) U_∞ = 5 m/s; b) U_∞ = 7.5 m/s; c) U_∞ = 10 m/s. The density is plotted as an intensity map, indicating the membrane vibration in log-scale.**

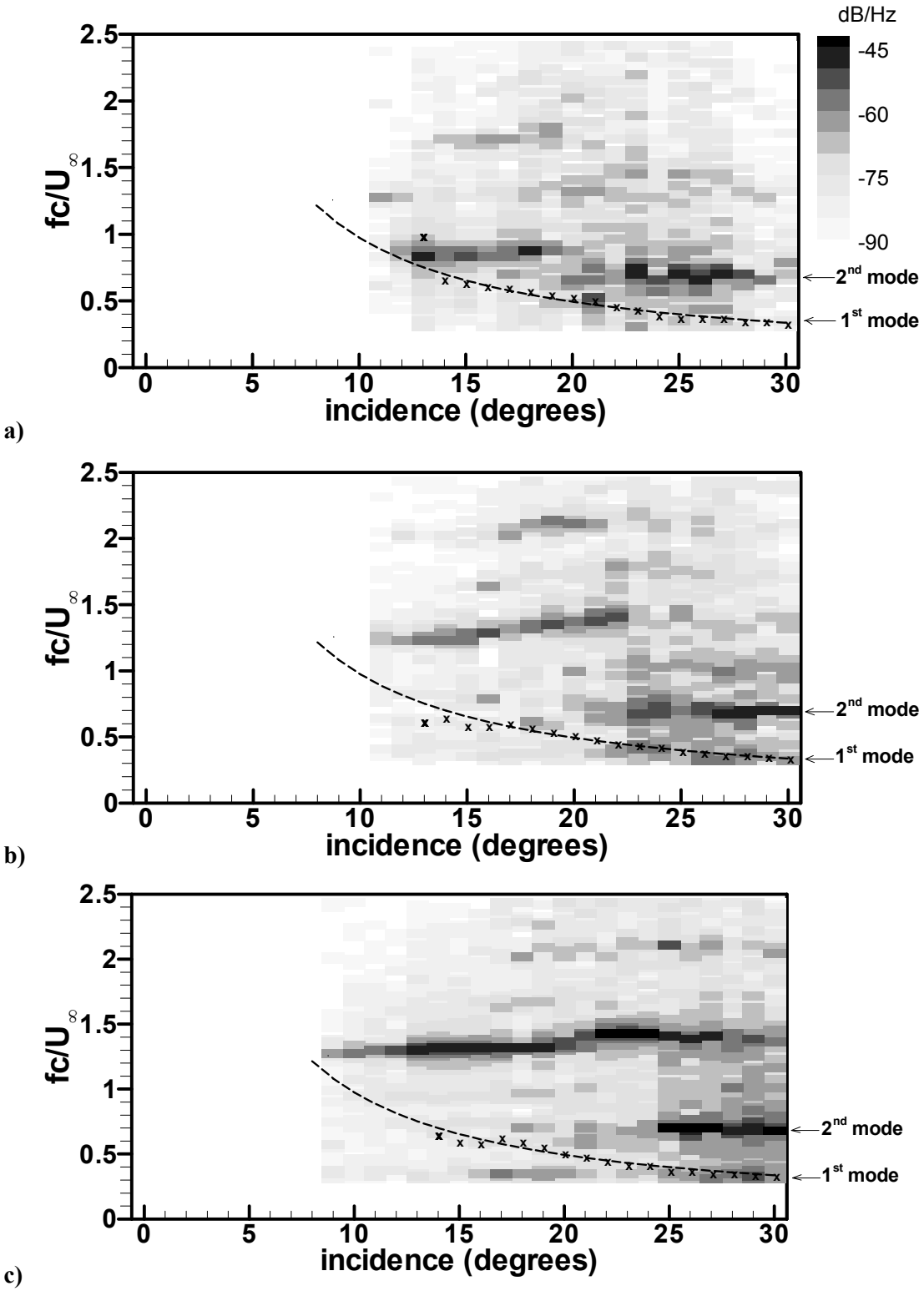

Figure 4.10: **Power spectral density of the membrane oscillations as a function of angle of attack for ε = 5% for: a) U_∞ = 5 m/s; b) U_∞ = 7.5 m/s; c) U_∞ = 10 m/s. The density is plotted as an intensity map, indicating the membrane vibration in log-scale.**

Similar to the previous Chapter, an attempt was made to predict the natural frequencies of the membrane based on the linear elastic theory, using the estimated tension from the mean deformation. Assuming two-dimensional membrane shape, the predictions for the first mode varied between ±100% of the experimentally measured frequencies, depending on the freestream velocity, pre-strain or excess length, with no clear trend. It is believed that this highlights the nonlinear nature of the fluid-structure interaction. In general, the Strouhal number is on the order of unity. At relatively high angles of attack, where the second mode is always observed, the Strouhal number is close to unity regardless of the pre-strains and excess lengths of the membrane. This is consistent with previous results for the zero pre-strain aerofoil, suggesting a coupling of the membrane oscillation with vortex shedding from the membrane.

As mentioned earlier, the alternative definition of the Strouhal number is reported to be constant for flat-plates and thin aerofoils, with values given in the range of 0.16 to 0.22 (Fage and Johansen 1927; Abernathy 1962; Miranda et al. 2005). In this study, the vortex shedding frequency in the wake of a rigid membrane (an equivalent rigid cambered aerofoil which was used in the previous investigation) was obtained with hot-wire anemometry and is shown in Figure 4.7 to Figure 4.10 as cross symbols. It should be noted that the natural wake frequencies were not measured for a range of camber values, and the rigid thin aerofoil had a shape derived from the zero pre-strain membrane only. It represents an average of the cases with smaller camber (aerofoils with pre-strain) and larger camber (aerofoils with excess length). Nevertheless, the constant for the modified Strouhal number is expected to be not too different, as it is around 0.2 for various bluff bodies. In these figures, the symbols show the measured frequencies in the wake and the dashed line shows the variation of the Strouhal number calculated from the alternative definition based on the vertical distance between the leading-edge and trailing-edge, assuming a constant value of 0.17 to fit our data. The results suggest that the membrane oscillations might be coupled with the vortex shedding. In particular, at high incidences where the second mode is observed, the membrane oscillations might be coupled with the first harmonic of the natural frequency. In active flow control studies with rigid aerofoils by Miranda et al. (2005) and Wu et

al. (1998), it was found that vortex shedding may lock on the first harmonic or the subharmonic of the natural frequency.

4.5 UNSTEADY FLOW

Figure 4.11 shows the comparison of the turbulence intensity $\overline{u'^2 + v'^2} / U_\infty^2$ in the measurement plane for the aerofoils with excess length of 2.5%, 5%, and pre-strain 2.5%, 5%, together with the results of the aerofoil with zero pre-strain at $\alpha = 14^o$ (left column), 18^o (middle column) and 25^o (right column), for $U_\infty = 5$ m/s. For $\alpha = 14^o$, the weakest shear layer fluctuations are seen for the aerofoil with excess length, whereas the strongest turbulence intensity is observed for the membrane with pre-tension. By increasing the angle of attack, the shear layer moves away from the membrane surface. For aerofoils with excess length, the turbulence intensity increases with increasing angles of attack. For other aerofoils, there is a decrease in turbulence intensity with increasing incidence.

The Reynolds stress component shown in Figure 4.12 exhibits similar trend to that of the turbulence intensity. The location of the maximum values of the Reynolds stress moves away from the membrane surface and downstream with increasing angle of attack. Peak magnitudes are observed for the aerofoil with 2.5% pre-strain at $\alpha = 14°$ and 18°, and for the aerofoil with 5% excess length at $\alpha = 25°$. The relatively large value of the Reynolds stress observed for these cases is related to the formation of vortices. Examinations of the instantaneous flow fields suggest that the peak of the Reynolds stress coincides with the roll-up of the large vortices.

4.6 SMOKE FLOW VISUALISATION

The smoke flow patterns for 2.5% excess length ratio and 2.5% pre-tension together with the results for the aerofoil with zero pre-tension and the rigid aerofoil are presented in Figure 4.13. It is seen that at the lower incidence ($\alpha = 14^o$), the size of the separation region for $\varepsilon = 2.5\%$ and $\delta_0 = 0\%$ is small. The oscillation of the membrane with excess length seems to excite the shear layer. The aerofoil with pre-tension shows a larger size of separation region than the one with zero pre-tension, and this is more evident at the higher incidence. At the higher incidence ($\alpha = 18^o$) the roll-up of large vortices is evident over the flexible

membrane with ε = 2.5% and δ_0 = 0%. The membrane aerofoil with ε = 2.5% shows the smallest size of separation region among other aerofoils. The aerofoil with pre-tension does not induce the roll-up of vortices over the aerofoil. This is also similar to the flow pattern for the rigid aerofoil.

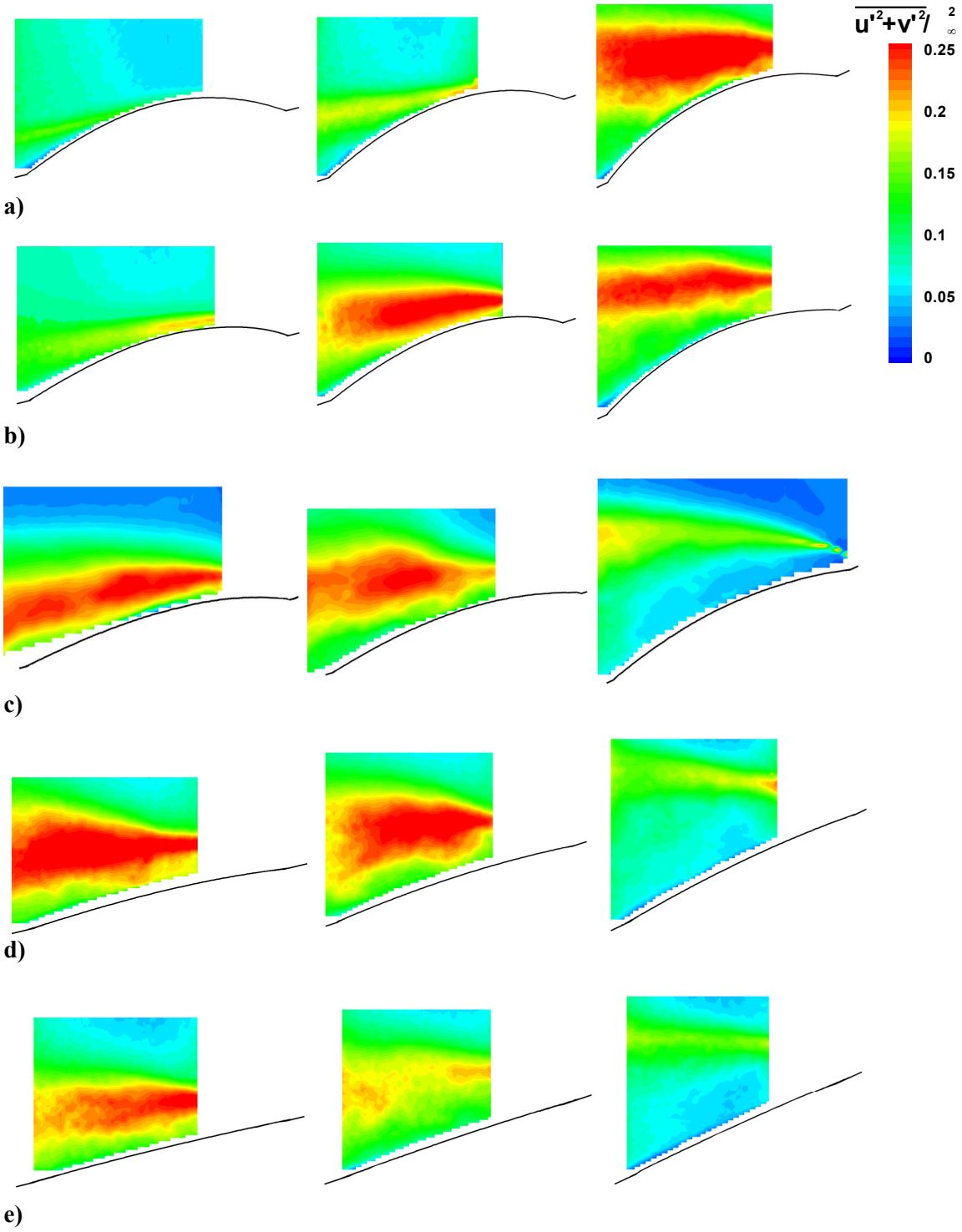

Figure 4.11: Turbulence intensity at U_∞ = 5 m/s (left: α = 14°, middle: α = 18°, right: α = 25°) for: a) ε = 5%; b) ε = 2.5%; c) δ_0 = 0%; d) δ_0 = 2.5%; e) δ_0 = 5%. Flow is from *right* to *left*.

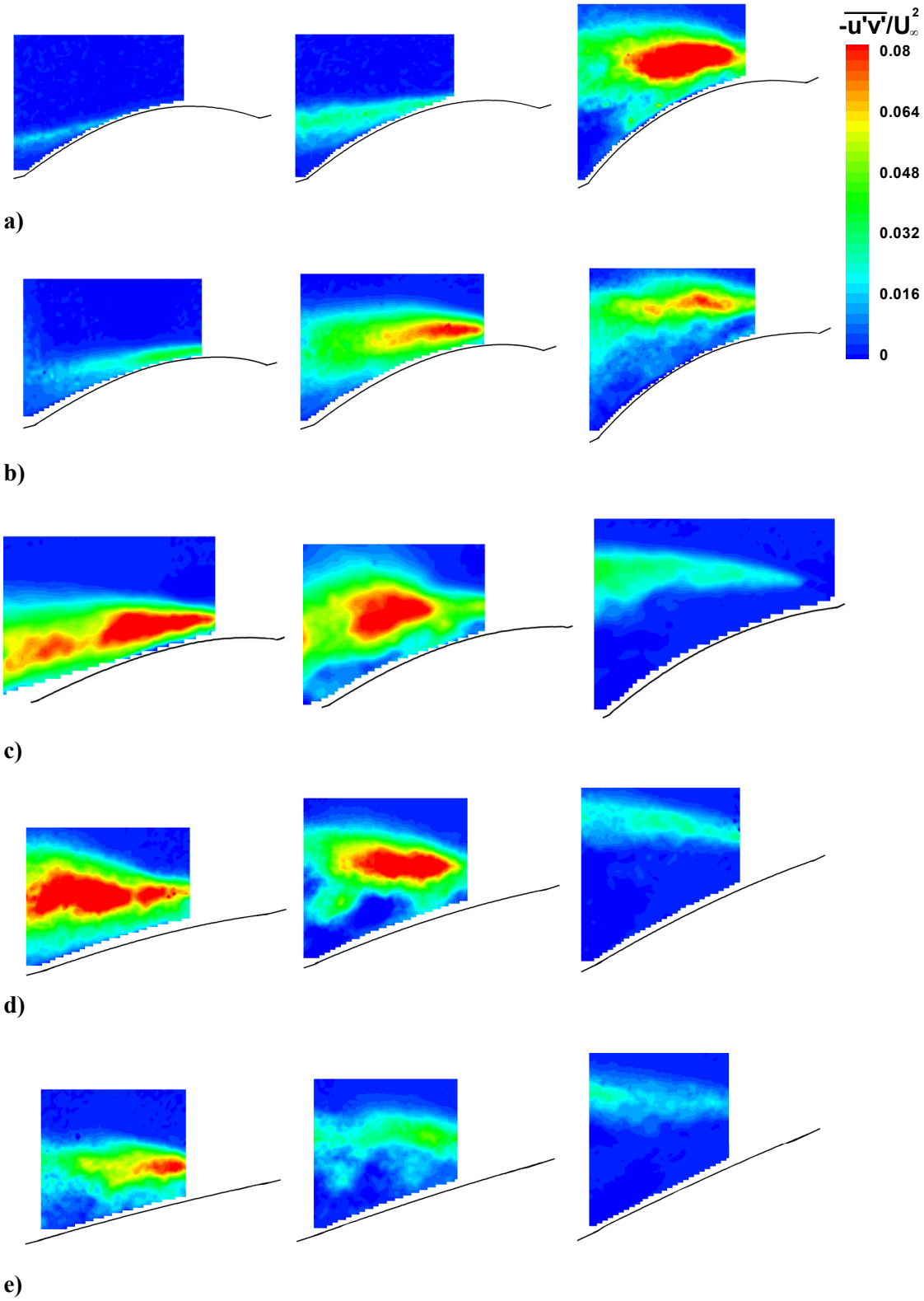

Figure 4.12: Reynolds stress at U_∞ = 5 m/s (left: $\alpha = 14^o$, middle: $\alpha = 18^o$, right: $\alpha = 25^o$) for: a) ε = 5%; b) ε = 2.5%; c) δ_0 = 0%; d) δ_0 = 2.5%; e) δ_0 = 5%. Flow is from *right* to *left*.

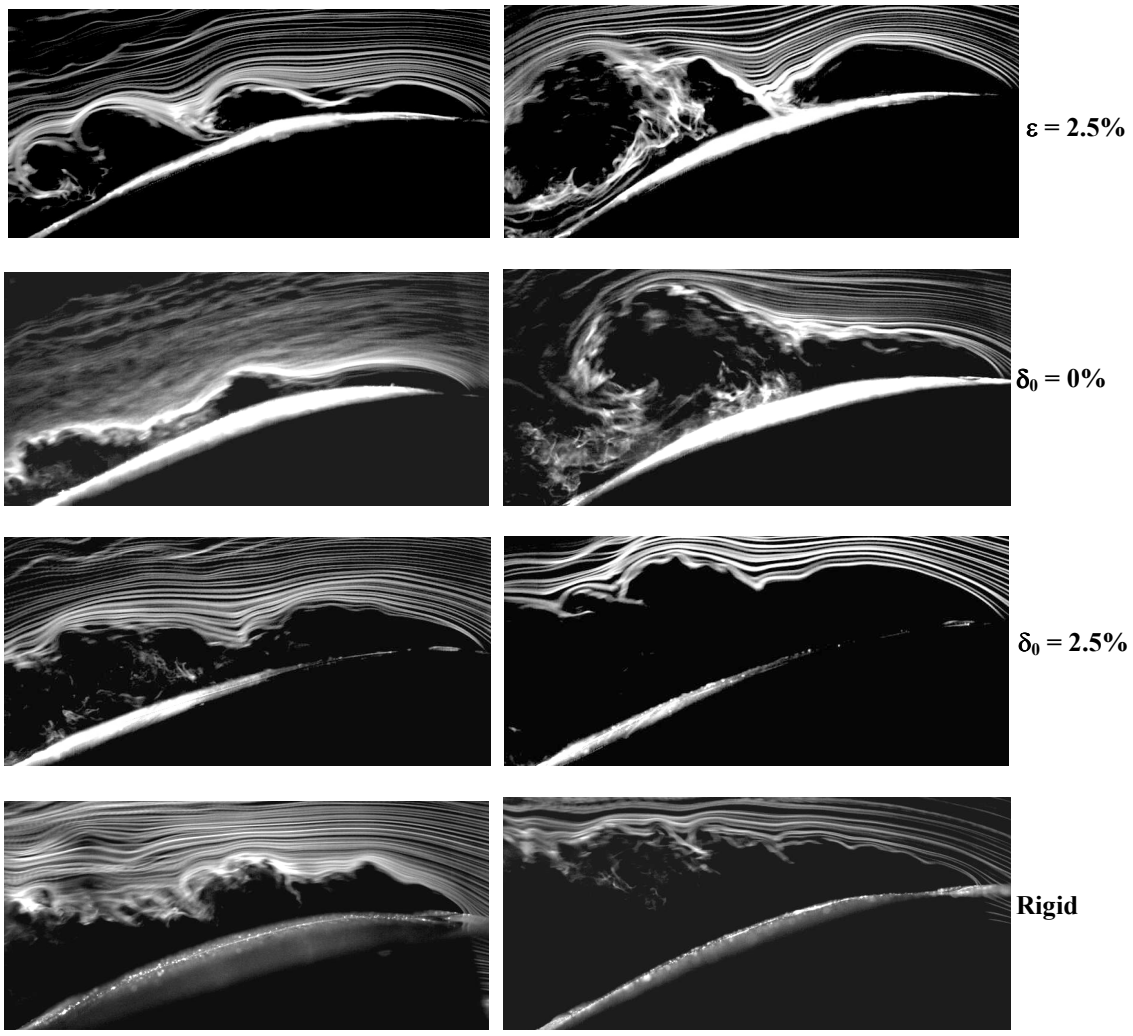

Figure 4.13: Smoke flow visualisation for flexible (ε = 2.5%, δ_0 = 0%, and δ_0 = 2.5%) and rigid aerofoils, U_∞ = 5 m/s, (left: α = 14°, right: α = 18°). Flow is from *right* to *left*.

4.7 CONCLUSIONS

High frame rate measurements of deformation and velocity fields were conducted for various membrane aerofoils with pre-strain and excess length. The following conclusions are drawn:

- The maximum camber and strain of the time-averaged membrane depends on the membrane pre-strain and excess length. The effect of the angle of attack is small for these mostly separated flows at low Reynolds numbers. The largest camber is observed for the aerofoil with excess length. The strain is also largest for the aerofoil with excess length.

- The membrane tension is dominated by the pre-tension at the smallest freestream velocity, but it becomes of similar magnitude for all aerofoils with increasing freestream dynamic pressure.

- The time-averaged velocity field exhibits smaller separated region for aerofoils with excess length due to their larger camber. The shear layer moves closer to the aerofoil surface and separation is delayed with increasing freestream velocity. On the other hand, the aerofoils with pre-strain have large flow separation regions.

- The onset of the membrane vibrations is delayed to a larger angle of attack for the aerofoils with excess length. In general, the mode number of the membrane vibrations is larger for the membranes with excess length than for those with pre-strain. The Strouhal number remains on the order of unity. Both the mode number and Strouhal number tend to decrease with increasing angle of attack.

- Measured frequencies of the membrane vibrations suggest a possible coupling with the wake instabilities.

- The magnitude of the shear layer fluctuations is seen to be dependent on the angles of attack, and the trends are different for the aerofoils with excess length and pre-strain. The Reynolds stress component shows a similar trend to that of the turbulence intensity.

- The roll-up of large vortices excited by the membrane oscillations at a high angle of attack is more evident, and the shear layer is closer to the aerofoil surface for the aerofoil with excess length than for the one with pre-tension, which generally behaves more similarly to a rigid aerofoil.

CHAPTER 5: UNSTEADY AERODYNAMICS OF LOW ASPECT RATIO MEMBRANE WINGS

5.1 INTRODUCTION

The findings obtained on the two-dimensional membrane aerofoils, presented previously, served as a motivation for the experimental results presented in this Chapter. The interaction of the membrane oscillation and the unsteady flow has already shown favourable effects for the two-dimensional membrane aerofoils, encouraging further investigation into three-dimensional wings. Therefore, this Chapter extends the previous studies on the unsteady fluid-membrane interactions of two-dimensional membrane aerofoils to low aspect ratio membrane wings. Particular focus is on the unsteady fluid-structure interactions and the role of the vortex lift. A low aspect ratio rectangular membrane wing and a simple nonslender delta wing are investigated. The use of wing flexibility as a passive flow control method for thin flat-plate delta wings was previously studied by Vardaki et al. (2005). A nonslender delta wing with sweep angle of $\Lambda = 50^o$ shows an increase in lift coefficient of up to 45%, whereas there is no lift enhancement for a slender wing. Therefore the delta wing with $\Lambda = 50^o$ is chosen for the present experiment as a promising candidate. Membrane deformation was measured with a Digital Image Correlation system. Measurements of the time-averaged membrane deformation and the time-averaged normal force coefficient were combined with the measurements of unsteady deformation and spectral analysis of vibration frequency. In addition, measurements of the velocity field with a Digital Particle Image Velocimetry were conducted.

5.2 TIME-AVERAGED DEFORMATION

For the rectangular wing, Figure 5.1 shows examples of the time-averaged membrane displacement in the direction normal to the chord-line, for U_∞ = 5 m/s.

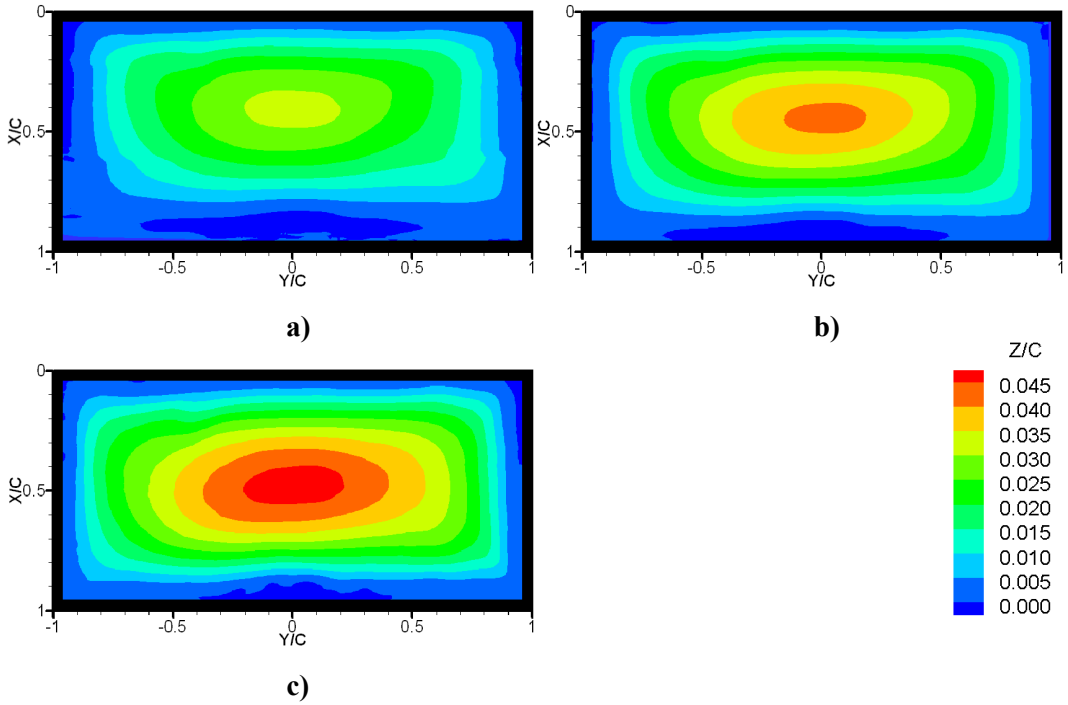

Figure 5.1: Magnitude of time-averaged displacement for U_∞ = 5 m/s; a) α = 10°; b) α = 14°; c) α = 25°. Flow is from top-side.

Even though there are in-plane motions (in the x and y directions) due to the nature of membrane skin, the deformation in the out-of-plane direction is considerably more dominant. As expected, the magnitude of the time-averaged displacements increases with increasing angles of attack. The displacement contours are approximately symmetrical with respect to a mid-span plane. The peak locations are slightly towards the leading-edge. This is consistent with the previous study of the two-dimensional membrane aerofoil, for which the maximum cambers occur slightly forward of the mid-chord. The variation of these maximum magnitudes of z-displacement as a function of angles of attack is shown in Figure 5.2 for different freestream velocities. For the lowest freestream velocity U_∞ = 5 m/s, the maximum displacement increases gradually up to about α = 20°, then stays roughly constant. The membrane generates a larger magnitude of the maximum camber as the freestream velocity is increased. Notably, there is also camber at zero angle of attack particularly at U_∞ = 10 m/s.

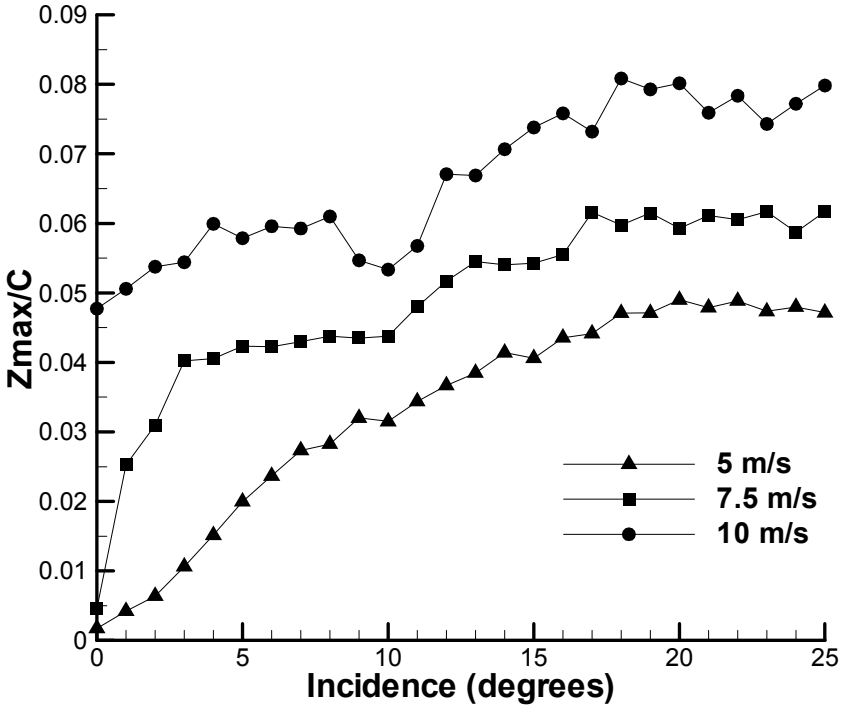

Figure 5.2: Maximum magnitude of time-averaged displacement as a function of incidence for the rectangular wing.

Typical examples of the time-averaged normalised membrane displacements of the delta wing are shown in Figure 5.3. Similar to the rectangular wing, the z displacement is larger at higher angles of attack.

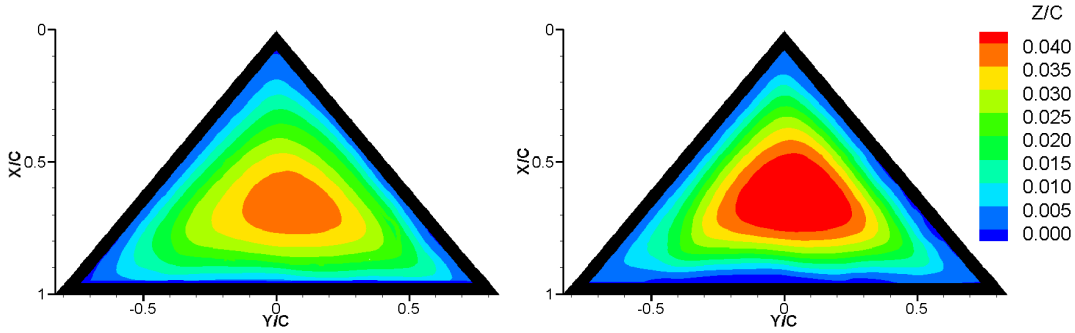

Figure 5.3: Magnitude of time-averaged displacement for U_∞ = 10 m/s; a) $\alpha = 10^o$; b) $\alpha = 25^o$. Flow is from top-side.

The variation of the maximum magnitudes of the normalised displacement as a function of angles of attack is shown in Figure 5.4 for different freestream velocities. Generally, the delta wing exhibits similar trends of the variations in displacements to those of the rectangular wing, but with smaller magnitude. For U_∞ = 5 m/s and at small incidences, the slope is relatively steep which means that the membrane cambering is more sensitive to the change in angles of attack within this range. For this freestream velocity, the maximum displacement increases

gradually up to about $\alpha = 21^{o}$. Once again the membrane shows a larger magnitude of the maximum displacement as the freestream velocity is increased. However the rate of the increase of the maximum displacement z_{max}/c with angle of attack α is smaller for the higher freestream velocities.

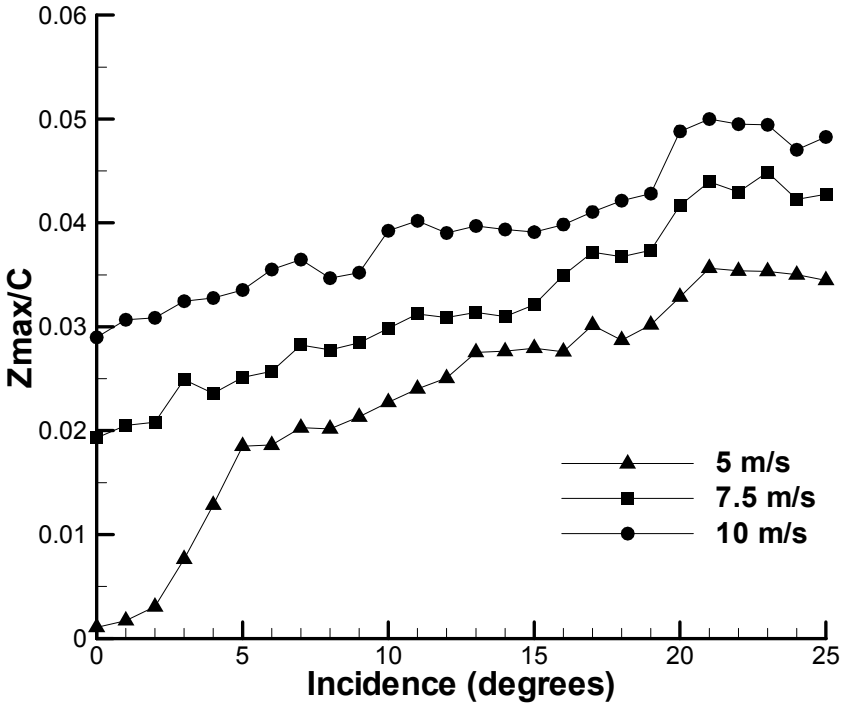

Figure 5.4: Maximum magnitude of time-averaged displacement as a function of incidence for the delta wing.

5.3 NORMAL FORCE COEFFICIENT

The variation of the time-averaged normal force coefficient is shown as a function of angle of attack in Figure 5.5 for the membrane and rigid rectangular wings at different freestream velocities. The normal force was measured by using a load cell attached underneath the wing's support, described in section 2.4.6. Even though the displacement slopes (Figure 5.2) are not linear, the normal force slope is nearly linear until the stall. The flexible membrane wings have higher slopes than the rigid wings, and the stall angles are only slightly affected. These favourable larger slopes are not unexpected as the induced wing camber increases with increasing angle of attack. However, the corresponding increase in the camber alone does not explain the significant increase in the force slope. This will be discussed further with the PIV measurements of the tip vortices, which produce the vortex lift on low aspect ratio wings.

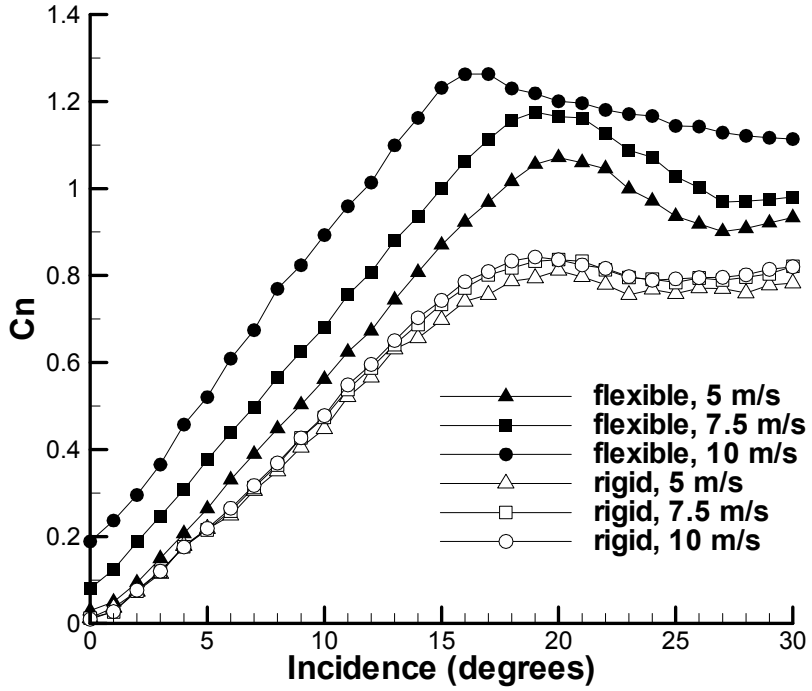

Figure 5.5: Normal force coefficient as a function of incidence for the flexible and rigid rectangular wings.

For rigid aerofoils, too much camber can result in a decrease in lift slope (Null and Shkarayev 2005). In contrast, the membrane wings tested in the present experiments exhibit the largest C_n slope for the largest camber. In addition, it is observed that the membrane wings start to generate the lift at $\alpha = 0^o$. This is consistent with the wing's maximum displacement (Figure 5.2) which shows a small camber at zero angle of attack. At the highest freestream velocity, $U_\infty = 10$ m/s, the membrane wing reaches the highest maximum normal force coefficient $C_{n,max}$ of approximately 1.26, which is about 1.5 times of that of the rigid wing.

Similar to the rectangular wing, the flexible delta wing exhibits a larger time-averaged normal force coefficient than the rigid delta wing as shown in Figure 5.6. At the highest freestream velocity, $U_\infty = 10$ m/s, the membrane wing reaches the highest $C_{n,max}$ of 1.16, which is approximately 1.2 times that of the rigid wing.

By comparing the delta wing with the rectangular wing, the stall angle of the delta wing is larger than that of the rectangular wing for all freestream velocities, for both flexible membrane and rigid wings. Even though the rigid delta wing reaches a higher $C_{n,max}$ than the rigid rectangular wing, the membrane delta wing has slightly lower $C_{n,max}$ than the membrane rectangular wing. For a delta wing in general, the flow pattern over its surface is vortex dominated. These vortices

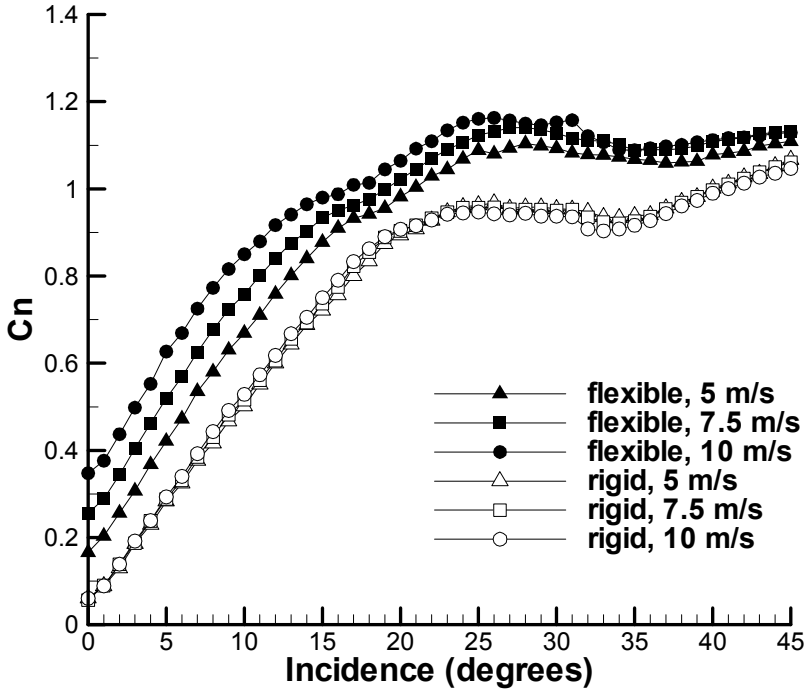

Figure 5.6: Normal force coefficient as a function of incidence for the flexible and rigid delta wings.

create a strong suction force on the top surface near the leading-edges, which enhances the lift. It is therefore no surprise to observe that the rigid delta wing has a larger $C_{n,max}$ and stall angle than the rigid rectangular wing. However it is interesting that the flexibility of the membrane provides more benefits to the rectangular wing than to the delta wing by enhancing the C_n slope and $C_{n,max}$ at a larger scale.

5.4 UNSTEADY DEFORMATION

For the rectangular wing, magnitudes of the normalised standard deviation z_{SD}/c are plotted in Figure 5.7 for different freestream velocities and angles of attack. The membrane vibrations are due to the unsteady flow over the wing. For low aspect ratio (LAR) wings, the unsteadiness is associated with the leading-edge separation as well as tip vortices. Combination of tip vortices and vortex shedding results in rather complicated unsteady deformation for this LAR membrane wing. The vibrational modes are symmetric with respect to the wing symmetry plane in most cases, although asymmetries are observed at some moderate to high angles of attack.

Figure 5.7-a illustrates the z_{SD}-contours for U_∞ = 5 m/s, at the low incidence ($\alpha = 10^o$), intermediate incidence ($\alpha = 17^o$) and relatively high incidence ($\alpha = 23^o$). At α

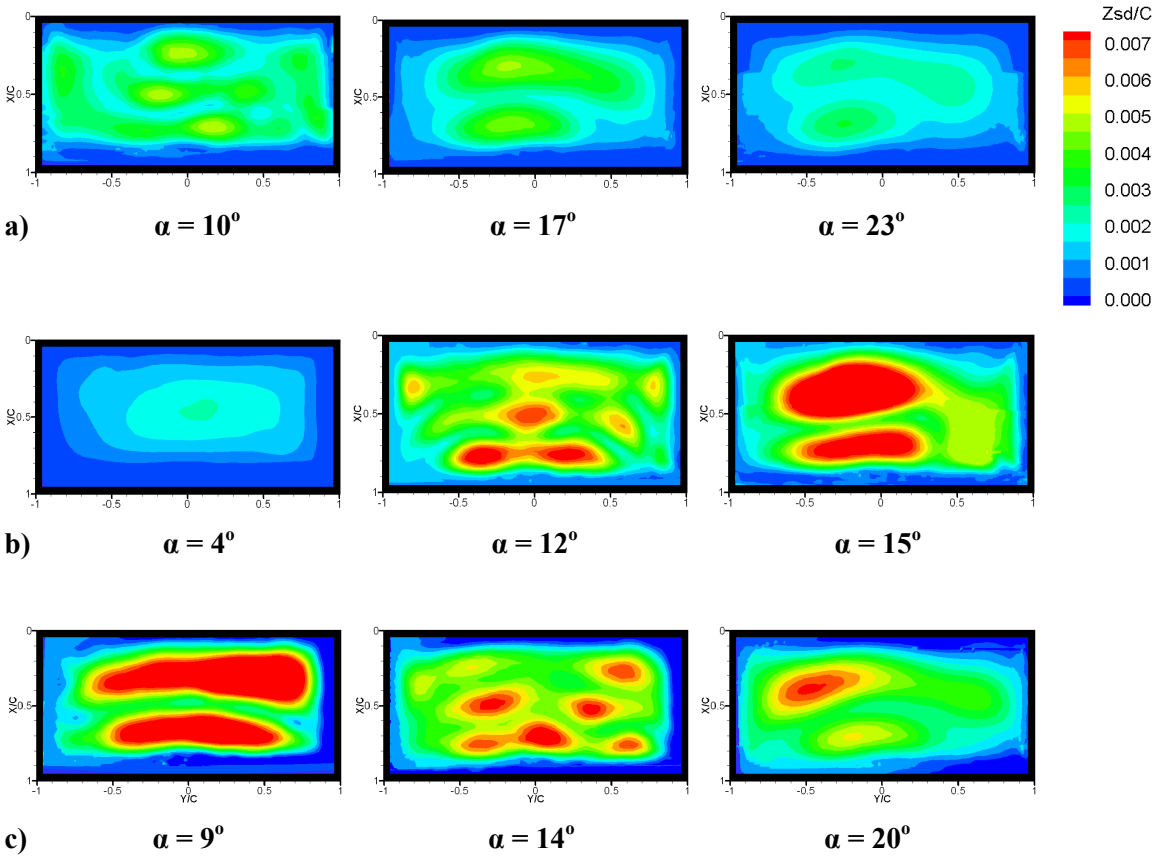

Figure 5.7: **Magnitude of standard deviation of membrane displacement at different incidences: a) U_∞ = 5 m/s; b) U_∞ = 7.5 m/s; c) U_∞ = 10 m/s. Flow is from top-side.**

= 10°, dominant vibrational modes could be identified as a spanwise mode of three and a streamwise mode of three. The two peaks near the wing tips suggest the membrane oscillations are induced by tip vortices, whereas the other peaks suggest the vibrations are induced by vortex shedding from the leading-edge. At the higher angle of attack (α = 17°) the vibrational modes in the spanwise direction are no longer visible, and only the streamwise mode of two is observed. In the previous study of the two-dimensional membrane aerofoil, there was evidence of coupling of membrane oscillations with the vortex shedding in the wake at high incidences and the dominant mode was also the second mode. We propose that the rectangular membrane wing at α = 17° might respond to the vortex shedding in the wake as well and this will be discussed later on with the help of the spectral analysis of the membrane vibrations. Similarly, for α = 23°, the second mode is also noticed with smaller magnitude. For U_∞ = 7.5 m/s, at the small incidence (α = 4°), a small amplitude of oscillation is observed indicating the first mode (see Figure 5.7-b). For the higher angle of attack, α = 12°, there are

mixed vibrational modes in the streamwise and spanwise directions. This oscillating pattern is similar to the pattern for U_∞ = 5 m/s, $\alpha = 10^o$ as discussed earlier. Again, the second mode in the streamwise direction is noticed at the higher angle of attack, $\alpha = 15^o$. For U_∞ = 10 m/s, the second mode is observed early at $\alpha = 9^o$ (see Figure 5.7-c). For the higher incidence, $\alpha = 14^o$, the higher vibrational modes are observed over the wing surface. This complicated pattern might be the result of the membrane responding to mixture of tip vortices and vortex shedding from the leading-edge.

Figure 5.8 shows the frequency spectra computed from the z-displacement of the membrane sampled at the point of maximum standard deviation. For small incidences, the dominant normalised frequencies (Strouhal numbers $St = fc/U_\infty$) are rather difficult to identify, suggesting that the magnitudes of vibration are very small. However starting around $\alpha \approx 7^o$ to 9^o, the dominant normalised frequencies fall in a well-defined band, and on the order of unity for all freestream velocities. Within certain ranges of angles of attack (such as $\alpha = 11^o$ to 14^o at U_∞ = 5 m/s in Figure 5.8-a), there seems to be higher modes. Of course, the change in the dominant frequencies is related to the change in the mode shapes. For example, the third mode of vibration for U_∞ = 5 m/s and $\alpha = 10^o$ shown in Figure 5.7-a corresponds to dominant frequency of approximately St = 1.1 as shown in Figure 5.8-a. On the other hand, the second modes for U_∞ = 5 m/s at $\alpha = 17^o$ and $\alpha = 23^o$ match with the dominant frequencies of St = 0.85 and 0.83, respectively. The relation between the mode shape and its corresponding dominant frequency is also visible for the higher freestream velocities (U_∞ = 7.5 m/s and 10 m/s). In addition, the standard deviation contours (as shown in Figure 5.7) suggest that the membrane tends to exhibit stronger vibrations at higher freestream velocities. This is confirmed by the frequency spectrum plot shown in Figure 5.8, in which we observe higher spectral density (darker bands) as the freestream velocity increases. On the other hand, the Strouhal number decreases slightly with increasing U_∞, particularly for incidences equal to and larger than $\alpha = 15^o$. At high incidences, where the second mode is always observed, the Strouhal numbers are in a similar range with those of the two-dimensional membrane aerofoils as shown previously in Chapter 3 (Figure 3.8). For two-dimensional membrane aerofoils, the oscillation in this range suggests coupling with the vortex shedding in the

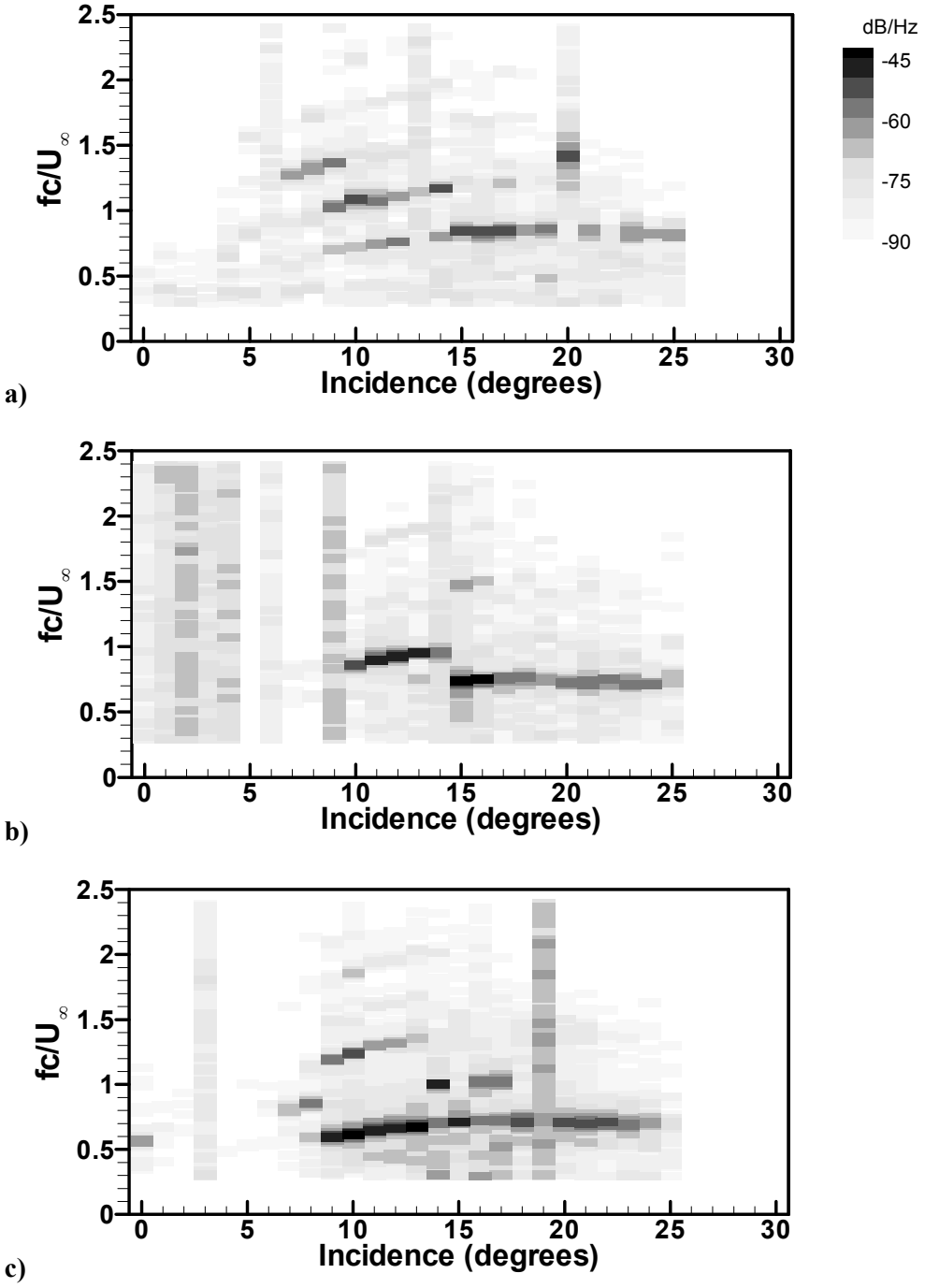

Figure 5.8: **Power spectrum of the membrane oscillating frequency as a function of angle of attack for the rectangular wing: a) U_∞ = 5 m/s; b) U_∞ = 7.5 m/s; c) U_∞ = 10 m/s. The density is plotted as an intensity map, indicating the membrane vibration in log-scale.**

wake. Therefore the present results suggest a possible coupling of membrane oscillation for the rectangular wing with the wake instabilities. In addition, the two-dimensional membrane aerofoil exhibits stronger vibrations at all freestream velocities compared with the rectangular wing, as suggested by the higher spectral density.

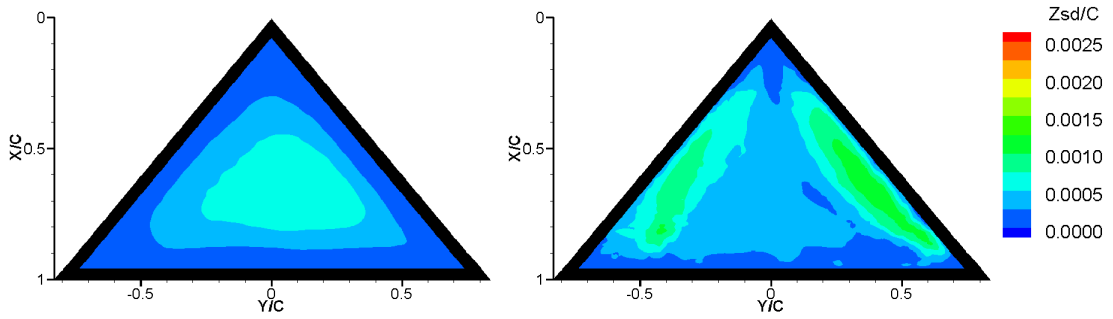

α = 14° α = 19°

α = 22° α = 25°

a)

α = 12° α = 22°

α = 23° α = 25°

b)

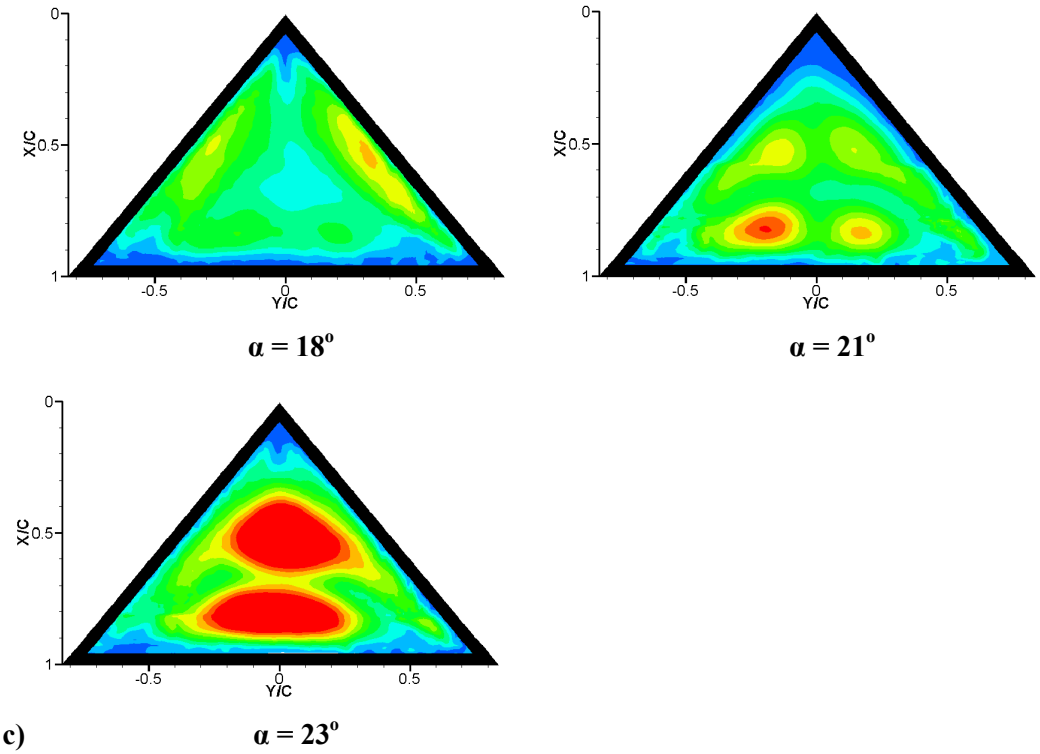

Figure 5.9: **Magnitude of standard deviation of membrane displacement at different incidences: a) U_∞ = 5 m/s; b) U_∞ = 7.5 m/s; c) U_∞ = 10 m/s. Flow is from top-side.**

Figure 5.9 illustrates the magnitude of standard deviation of membrane displacement normalised by the chord length for different freestream velocities and angles of attack for the delta wing. For U_∞ = 5 m/s and α = 14° (Figure 5.9-a), the membrane wing indicates the first mode of oscillation with small amplitude located approximately at the centre of the wing. At the larger incidence, α = 19°, it could be assumed that the leading-edge vortices become dominant, exciting the membrane symmetrically along the leading-edge of the wing. These vibrational modes alongside the wing leading-edge seem to blend with the other two in the streamwise direction as the incidence increases to α = 22°. At α = 25°, the vibrations close to the wing tips disappear and the second mode in the streamwise direction is observed. For the larger freestream velocity, U_∞ = 7.5 m/s (Figure 5.9-b), the membrane is substantially influenced by the leading-edge vortices at α = 12°. At α = 22°, the membrane clearly shows a higher mode with four peaks. It is possible that the vortex breakdown occurs within this range, resulting in the vibration pattern along the wing leading-edges becoming less-defined. The magnitude of the vibrations becomes weaker at α = 23°. Finally at α = 25° the second mode in the streamwise direction is observed. A similar trend of

vibrational modes at various angles of attack are seen for U_∞ = 10 m/s as shown in Figure 5.9-c. The vibrations along the wing leading-edges are noticed at $\alpha = 18^o$. The higher mode with four peaks appears at $\alpha = 21^o$. At last, the large magnitude of oscillation with the second mode is visible at $\alpha = 23^o$. Generally, the delta wing exhibits smaller amplitudes of oscillation compared to the rectangular wing. This can be seen from the lighter shade of the frequency spectra shown in Figure 5.10. The dominant frequencies are difficult to define except for at high angles of attack where the dominant frequencies are on the order of unity. It is well-known that the periodic fluctuations due to the vortex breakdown have a similar range of frequencies (Gursul 2005).

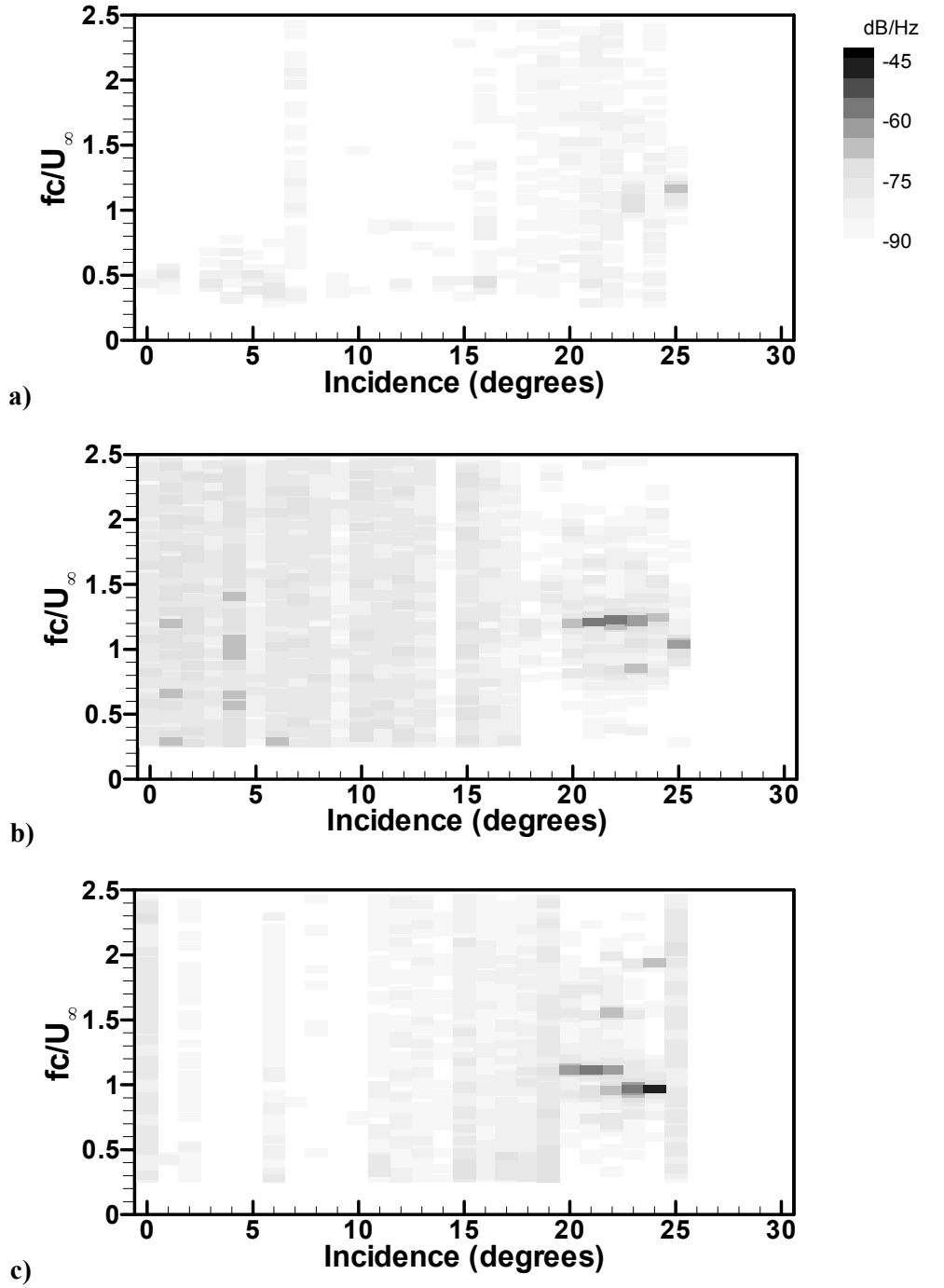

Figure 5.10: **Power spectrum of the membrane oscillating frequency as a function of angle of attack for the delta wing: a) U_∞ = 5 m/s; b) U_∞ = 7.5 m/s; c) U_∞ = 10 m/s. The density is plotted as an intensity map, indicating the membrane vibration in log-scale.**

5.5 VELOCITY FIELD

Figure 5.11 shows the comparison of the magnitude of the time-averaged velocity field superimposed on the streamline pattern for the rectangular wings at selected angles of attack. The data was taken for the rigid wing at U_∞ = 5 m/s, and the membrane wing at U_∞ = 5 m/s and 10 m/s. Starting with small incidence $\alpha = 5^o$, the flow remains attached for all wings. At higher angle of attack $\alpha = 10^o$, the flow on the rigid wing becomes separated. Even though the time-averaged velocity for the membrane wing at this angle shows that the flow is mostly attached, significant velocity fluctuations develop near the surface at U_∞ = 5 m/s as shown in Figure 5.12, which will be discussed later. For $\alpha = 16^o$, the shear layer moves away from the surface for the rigid wing, while the flow on the membrane wing is separated but the shear layer remains close to the surface. It is also seen that at this angle of attack, with increasing freestream velocity to U_∞ = 10 m/s, the shear layer for the membrane wing is getting closer to the wing surface while the camber of the wing increases. This effect of increasing freestream velocity is consistent with the previous work for two-dimensional membrane aerofoil. The separated shear layer moves further away from the surface with increasing angle of attack to $\alpha = 23^o$ for all wings. Again, the separation region is largest for the rigid wing, and smallest for the membrane wing with U_∞ = 10 m/s. For the latter, the closed streamline pattern (recirculation region) is seen on the wing surface, while it is located further downstream for the lower freestream velocity, and even further away from the trailing-edge for the rigid wing.

Figure 5.12 shows the turbulence intensity corresponding to the velocity field illustrated in Figure 5.11. For all wings, with increasing angle of attack the shear layer velocity fluctuations move away from the surface and also become stronger. With increasing camber at a given angle of attack, the region of velocity fluctuations moves closer to the wing surface. For the largest angle of attack $\alpha = 23^o$ and the largest freestream velocity U_∞ = 10 m/s, the velocity fluctuations are strong and located in a region just above the wing. The location of the high intensity velocity fluctuations with respect to the membrane surface affects the amplitude and mode of the membrane vibrations as shown in the previous Chapters. Here, in this Chapter, this can be seen from the comparison of membrane vibrations in Figure 5.8 and velocity fluctuations in Figure 5.12. The

membrane vibrations are the largest for the largest freestream velocity, when the shear layer is the closest to the wing surface. Also, the largest membrane vibrations are observed for intermediate incidences, because the shear layer moves further away from the wing surface at high incidences.

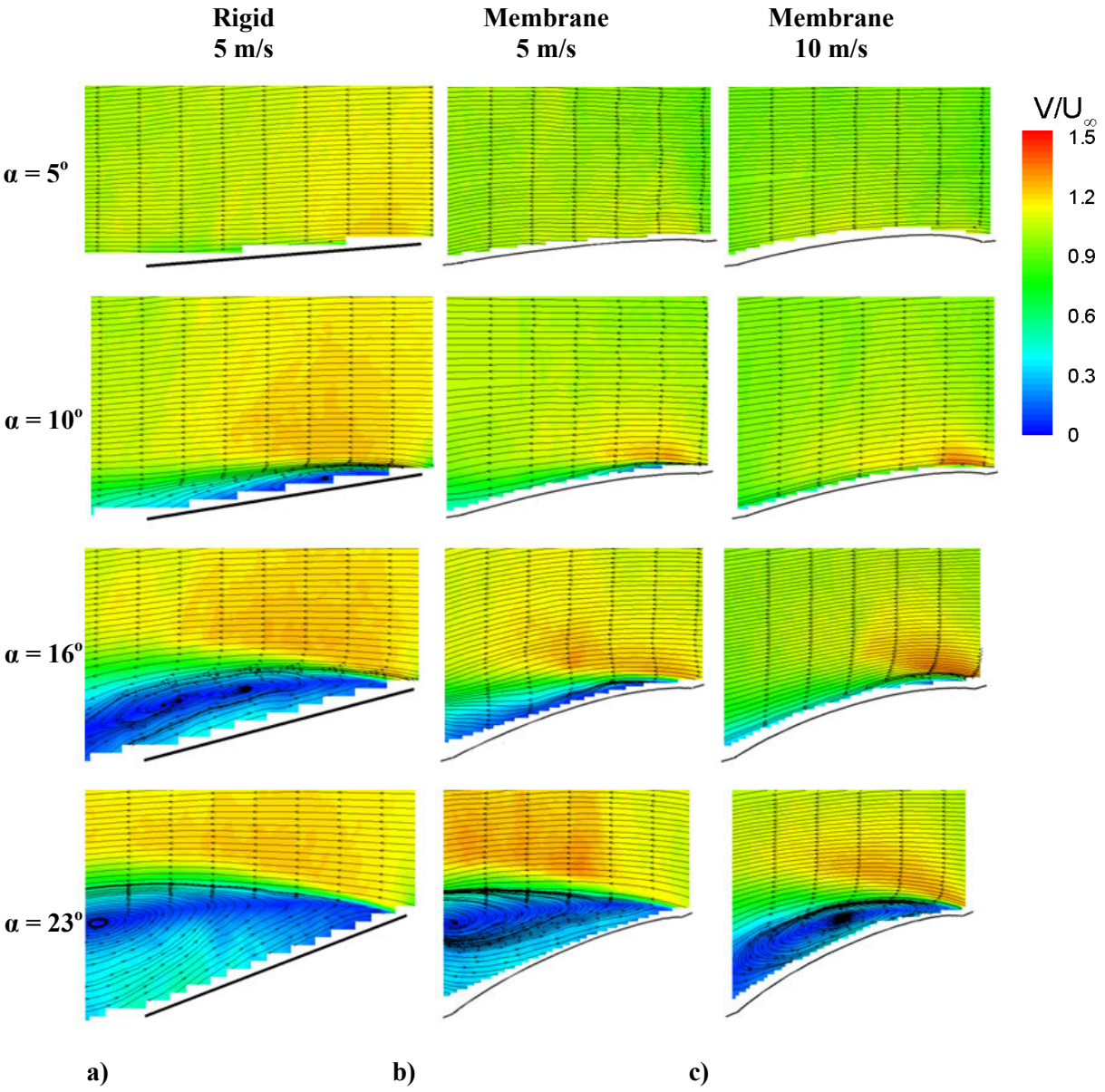

Figure 5.11: **Magnitude of the time-averaged velocity and streamlines in a mid-span plane for the rectangular wings; a) rigid wing U_∞ = 5 m/s; b) membrane wing U_∞ = 5 m/s; c) membrane wing U_∞ = 10 m/s. Flow is from *right* to *left*.**

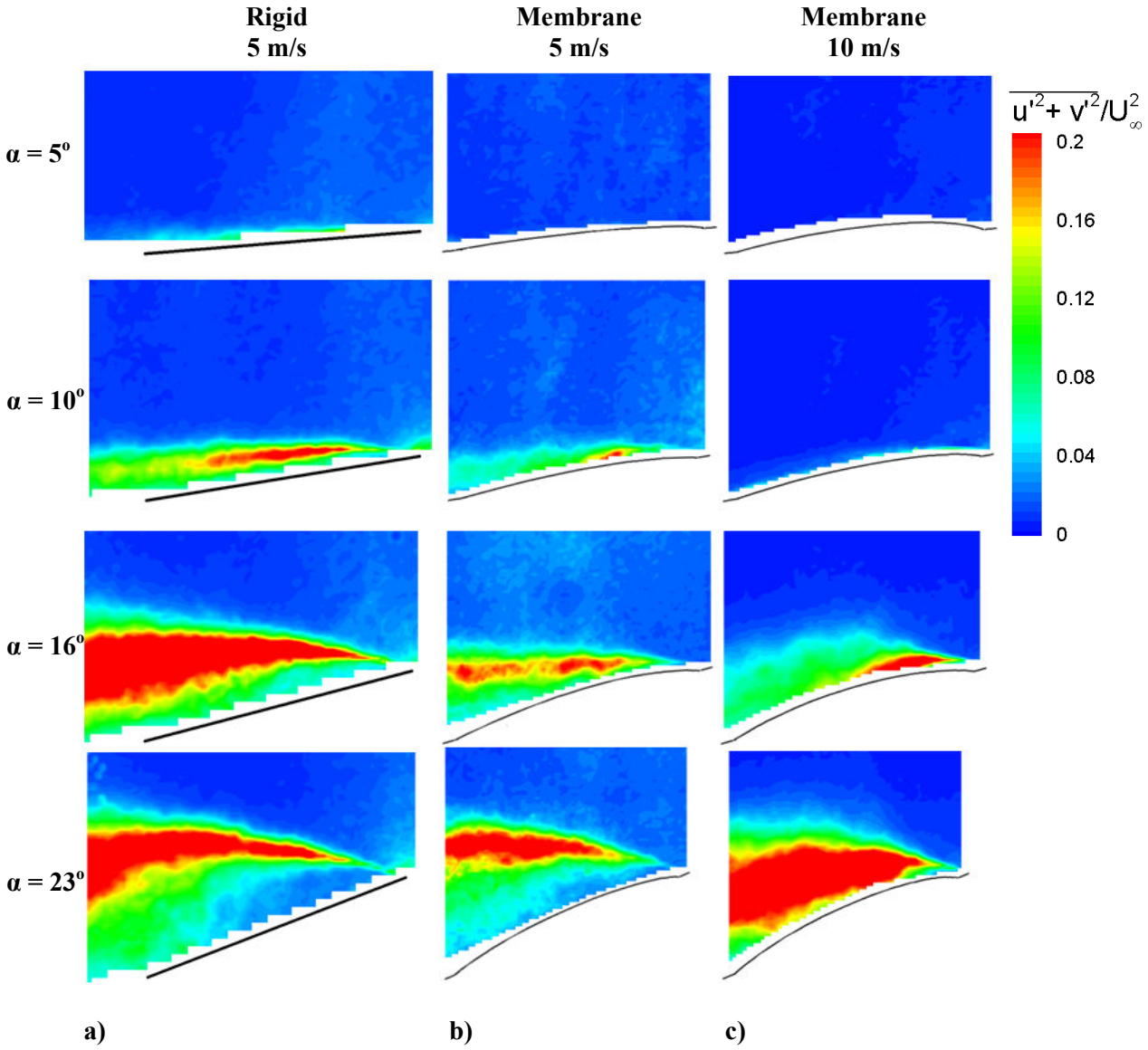

Figure 5.12: Magnitude of the turbulence intensity in a mid-span plane for the rectangular wings; a) rigid wing U_∞ = 5 m/s; b) membrane wing U_∞ = 5 m/s; c) membrane wing U_∞ = 10 m/s. Flow is from *right* to *left*.

Figure 5.13 shows the magnitude of the time-averaged velocity in a cross-flow plane near the trailing-edge for the rectangular rigid and membrane wings. The cross-flow velocity is seen to increase with increasing flexibility. This suggests stronger tip vortices with increasing camber. The magnitude of turbulence intensity in a cross-flow plane shown in Figure 5.14 also corresponds to the turbulence intensity in a mid-span plane shown in Figure 5.12. For the membrane wings, with increasing angle of attack velocity fluctuations become stronger. The variation of normalised circulation of the tip vortices is calculated as seen in

Figure 5.15. The circulation is calculated from the area integral of vorticity distributions in the cross-flow plane based on the PIV measurements. The clockwise and counter clockwise circulations on each side of wing tips were averaged. It is seen that the membrane wing has larger magnitude of the circulation than the rigid wing for both freestream velocities. Since the tip vortices (and vortex lift) contribute significantly to the total lift, this may be an additional mechanism for the increased lift with increasing membrane deformation (see Figure 5.5). Whereas the normalised circulation of the rigid wing remains virtually unchanged with increasing freestream velocity (Reynolds number), the normalised circulation increases for the membrane wing. It is also seen that the slope of the circulation decreases at high angles of attack for all wings. This corresponds to the decline in the normal force in the stall region.

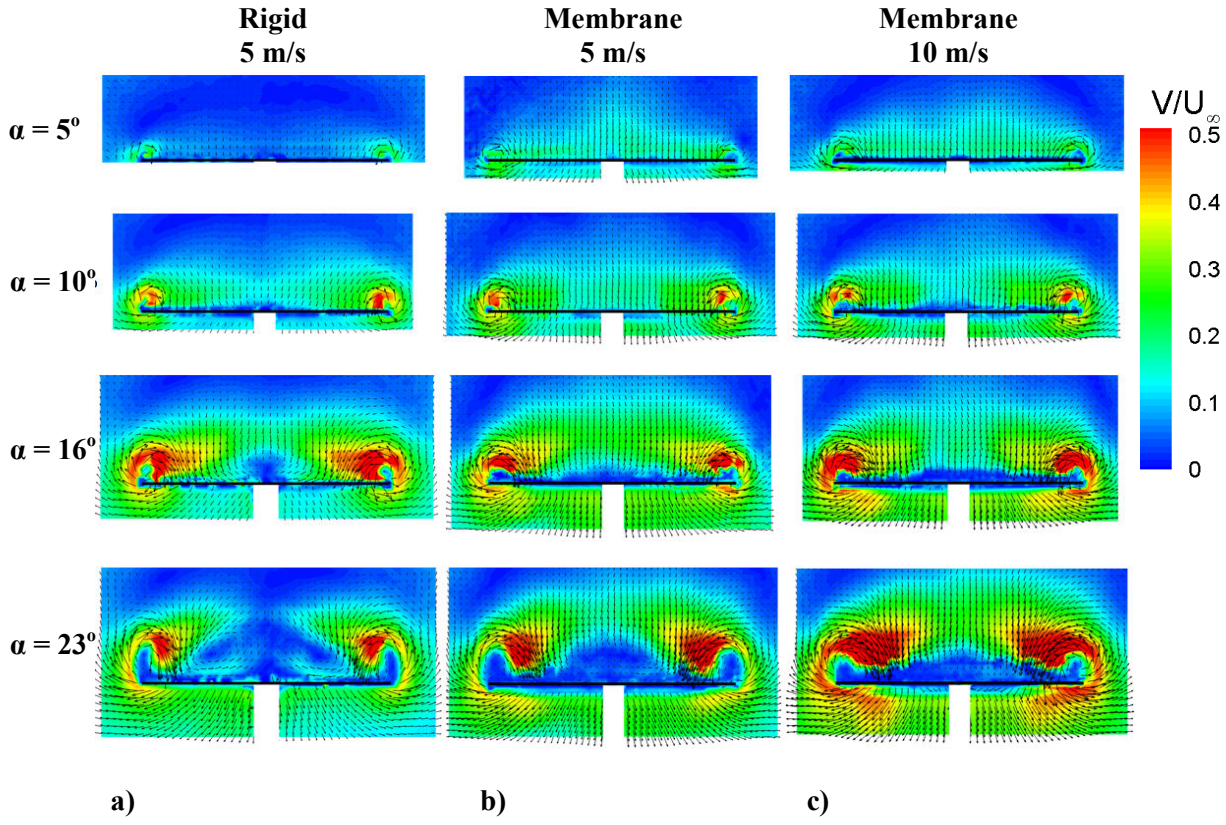

Figure 5.13: Magnitude of the time-averaged velocity in a cross-flow plane near a trailing-edge for the rectangular wings; a) rigid wing U_∞ = 5 m/s; b) membrane wing U_∞ = 5 m/s; c) membrane wing U_∞ = 10 m/s.

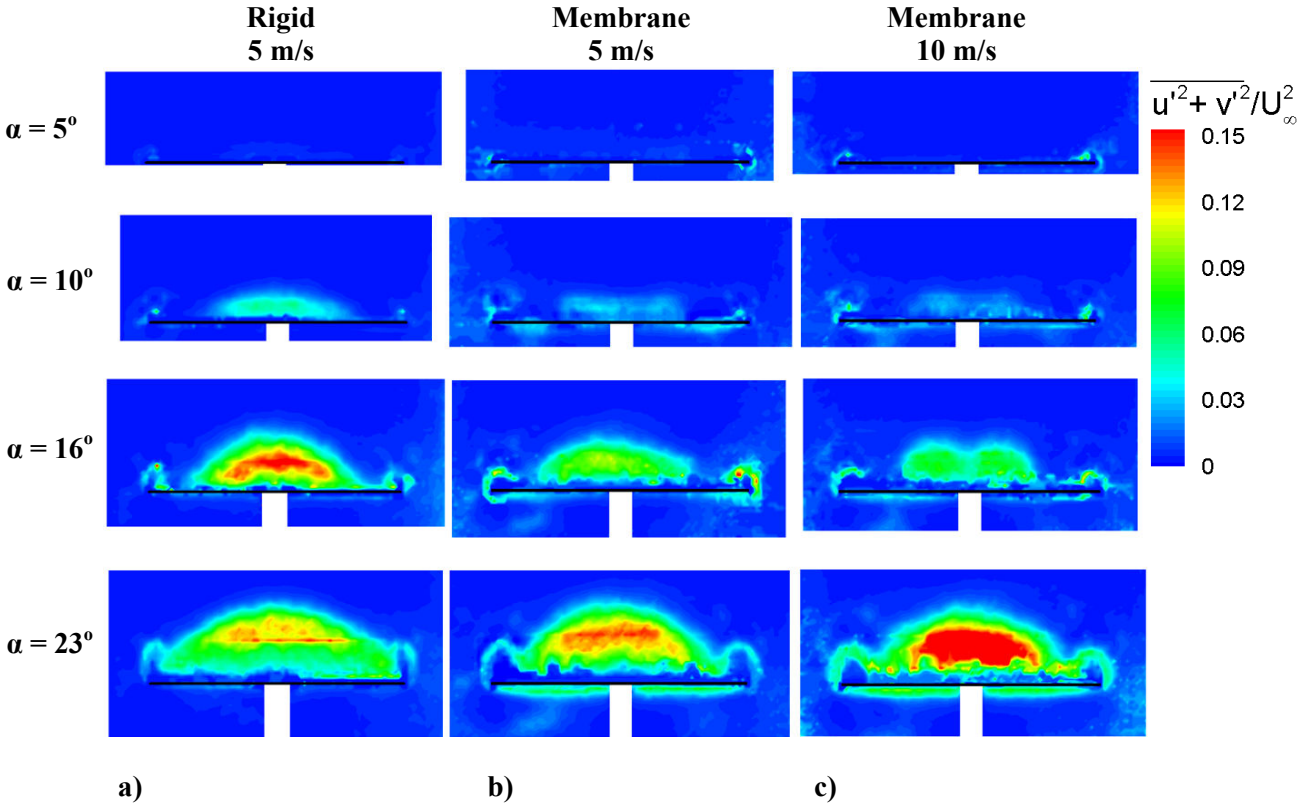

Figure 5.14: **Magnitude of the turbulence intensity in a cross-flow plane near a trailing-edge for the rectangular wings; a) rigid wing U_∞ = 5 m/s; b) membrane wing U_∞ = 5 m/s; c) membrane wing U_∞ = 10 m/s.**

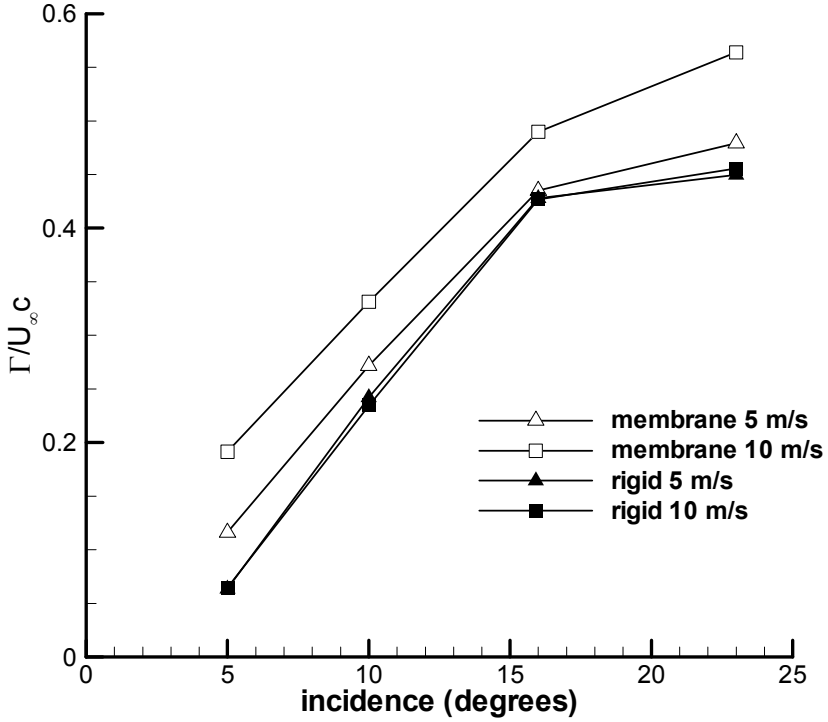

Figure 5.15: **Variation of normalised circulation of tip vortices in a cross-flow plane near a trailing-edge as a function of angle of attack for the rigid and membrane rectangular wings.**

5.6 CONCLUSIONS

Unsteady aerodynamics of low aspect ratio membrane wings (rectangular wing and delta wing) has been investigated. Measurements of membrane deformation, normal force coefficient and velocity field were conducted. The following conclusions are drawn:

- The magnitude of the time-averaged displacement increases with increasing angles of attack as well as increasing freestream velocities for both rectangular and delta wings.

- The comparison of the normal force coefficient between the flexible and rigid wings indicates that flexibility enhances the normal force.

- The flexibility benefits the rectangular wing more than the delta wing by increasing the maximum normal force, as well as the normal force slope by a larger scale when compared with the rigid wings of similar geometry.

- The normalised standard deviation contours indicate the existence of both streamwise and spanwise vibrational modes for the rectangular wing. The combination of tip vortices, and vortex shedding results in a mixture of streamwise and spanwise vibrational modes. For the delta wing, large oscillations near the wing leading-edges generally appear at moderate incidences, suggesting that the membrane responds to the unsteadiness of the leading-edge vortices. For both rectangular and delta wings, at higher angles of attack, the membrane oscillations are observed in a streamwise mode.

- The second mode always appears at high incidences, for all freestream velocities, which is similar to the observations for the two-dimensional membrane aerofoils. It is suggested that the membrane responds to the vortex shedding in the wake in the post-stall region.

- Comparison of the flow field measurements of the rigid and membrane wings indicates that the separation region becomes smaller with increasing membrane deformation. The tip vortices are also stronger for higher freestream velocities (increasing deformation) leading to increased circulation. The vortex lift due to

the tip vortices as well as increased camber enhances the total lift for the low aspect ratio membrane wings.

CHAPTER 6: CONCLUSIONS

The aerodynamics of flexible membranes was investigated experimentally in an open-jet wind tunnel for different values of the aeroelastic parameter and Reynolds number, over a range of angles of attack. The study covered a wide range of aspects such as the time-averaged shape of the membrane, mean flows, membrane oscillations, unsteady flows, and with particular emphasis on the unsteady aspects of the fluid-membrane interaction. The effects of membrane pre-strain and excess length on these characteristics were included. The low aspect ratio membrane wings were studied for both rectangular and nonslender delta wings. The role of flexibility in the lift enhancement and stall delay was examined.

The investigation of the two-dimensional membrane aerofoil indicates that even though the mean membrane shape is not very sensitive to the changes in angle of attack, the mean flow differs considerably. The flow remains attached at small incidences, and becomes weakly separated at moderate incidences with shear layer remaining close to the surface, and finally becomes fully separated with large recirculation at high incidences. It is found that the amplitude and mode of the membrane vibrations depend mainly on the relative location and magnitude of the unsteadiness of the shear layer. The oscillations are negligibly small when the flow remains attached at small incidences, and become more significant with increasing angles of attack, and are the largest when the separated shear layer is close to the surface. As the camber increases due to the increasing freestream velocity (increasing Reynolds number and decreasing aeroelastic parameter), the separated shear layer becomes more energetic and gets closer to the aerofoil surface. Strong coupling of the membrane oscillations with the unsteady flow is

demonstrated with a high degree of correlation. At moderate incidences, the flapping of the shear layer is more dominant, whereas at larger incidences, the roll-up of large vortices is more characteristic of the flow. The second mode is always observed at high incidences ($\alpha \geq 20°$), regardless of the Reynolds number. The variation of the Strouhal number suggests a possible coupling of membrane oscillations with the vortex shedding phenomenon in the wake. The comparison of the rigid and flexible membrane aerofoil indicates that the flexible membrane has a smaller size of the separation region. The roll-up of the large vortices excited by the membrane oscillations at larger incidences (α = 16° to 20°) keeps the shear later closer to the aerofoil and suggests delayed stall.

For the effects of membrane pre-strain and excess length, the aerofoils with excess length exhibit a smaller separated region due to their larger camber, and also larger mode numbers of vibrations than the aerofoils with pre-strain. This smaller separated region delays the onset of the membrane vibrations to a larger angle of attack. With increasing freestream velocity, the shear layer moves closer to the surface and separation is delayed for all aerofoils. The membrane tension is dominated by the pre-tension at the smallest freestream velocity, but it becomes of similar magnitude for all aerofoils with increasing freestream dynamic pressure. Measured frequencies of the membrane vibrations suggest a possible coupling with the wake instabilities for all aerofoils. The roll-up of large vortices excited by the membrane oscillations at high angle of attack is more evident for the aerofoil with excess length than for the aerofoil with pre-tension, which generally behaves more similarly to a rigid aerofoil.

It is found that the flexibility benefits the low aspect ratio rectangular wing more than the delta wing by increasing the maximum normal force, as well as the normal force slope, when compared to the rigid wings, by a larger amount. The combination of tip vortices, and vortex shedding results in a mixture of streamwise and spanwise vibrational modes. For the delta wing, large oscillations near the wing leading-edges generally appear at moderate incidences, suggesting that the membrane responds to the unsteadiness of the leading-edge vortices. The streamwise modes appear at higher angles of attack for both rectangular and delta wings. Similar to the two-dimensional membrane aerofoils, the second mode always appears at high incidences, for all freestream velocities. The Strouhal

numbers of membrane vibration frequencies are on the order of unity, and have a similar range to those of two-dimensional aerofoils. The results suggest that the membrane responds to the wake instabilities in the post-stall region. The comparison with the rigid wing indicates that the membrane wing induces stronger tip vortices, resulting in the increased circulation. This vortex lift contributes significantly to the total lift enhancement.

Much progress has been made in this research area, and the series of experimental results obtained in this thesis includes several features of the flow-membrane interaction that are quite surprising. However, there are other issues that are not focused on quantitatively such as added mass effects or fluid forcing due to leading-edge vortex shedding. Under aerodynamic loads, the response frequencies depend on both the natural frequencies of the membrane and the distribution of vortex-shedding frequencies. The correlation between the added mass and the membrane displacement could provide better insight into the unsteady aspect. In addition, since all experiments are investigated by varying freestream the velocity, not only the Reynolds number but also the aeroelastic parameter is changed, and it is therefore difficult to look at these effects separately. The solution to this issue would be by using different membrane material such as different membrane thickness or elastic modulus. The present experiments have already shed light on the aerodynamic characteristics of the membrane, but adding these missing details along with a numerical validation would benefit the design of membrane wing vehicles even greater.

REFERENCES

ABERNATHY, F.H., 1962. Flow over an inclined plate. *Transactions of the ASME, Journal of Basic Engineering*, pp. 380-388.

ALBERTANI, R., STANFORD, B., HUBNER J.P., and IFJU, P.G., 2007. Aerodynamic coefficients and deformation measurements on flexible micro air vehicle wings. *Experimental Mechanics*, 47(5), pp. 625-635.

ALVING, A.E., and FERNHOLZ, H.H, 1996. Turbulence measurements around a mild separation bubble and downstream of reattachment. *Journal of Fluid Mechanics*, 322, pp. 297-328.

ANDERSON, JR. J.D., 1989. *Introduction to Flight*. 3rd ed. New York: McGraw-Hill International Edition.

ANDERSON, JR. J.D., 2001. *Fundamentals of Aerodynamics*. 3rd ed. New York: McGraw-Hill International Edition.

BENDAT, J.S., and PIERSOL, A.G., 1986. *Random Data, Analysis and Measurement Procedures*. 2nd ed. Wiley-InterScience.

BISHOP, K.L., 2006. The relationship between 3-D kinematics and gliding performance in the southern flying squirrel, Glaucomys Volans. *Journal of Experimental Biology*, 209(4), pp. 689-701.

BRENDEL, M., and MUELLER, T.J., 1988. Boundary layer measurements on an airfoil at a low Reynolds number in an oscillating freestream. *AIAA Journal*, 26(3), pp. 257-263.

BRUCK, H.A., MCNEILL, S.R., SUTTON, M.A., and PETERS, W.H., 1989. Digital image correlation using Newton-Raphson method of partial differential correction. *Experimental Mechanics*, 29(3), pp. 261-267.

CARMICHAEL, B.H., 1981. Low Reynolds number airfoil survey. *NASA CR-165803*.

CHU, T.C., RANSON, W.F., SUTTON, M.A., and PETERS, W.H., 1985. Applications of digital-image-correlation techniques to experimental mechanics. *Experimental Mechanics*, 25(3), pp. 232-244.

CRABTREE, L.F., 1957. Effect of leading-edge separation on thin wings in two-dimensional incompressible flow. *Journal of Aeronautical Sciences*, 24, pp. 597-604.

DELUCA, A.M., REEDER, M.F., and OL, M.V., 2004. Experimental investigation into the aerodynamic properties of a flexible and rigid wing micro air vehicle. *24th AIAA Aerodynamic Measurement Technology and Ground Testing Conference*, 28 Jun – 1 Jul, Portland, Oregon, AIAA 2004-2396.

EARNSHAW, P.B., and LAWFORD, J.A., 1964. Low speed wind tunnel experiments on a series of sharp-edged delta wings. *Aeronautical Research Council Reports and Memoranda*, 3424.

FAGE, A., and JOHANSEN, F.C., 1927. On the flow of air behind an inclined flat plate of infinite span. *Proceedings of the Royal Society of London, Series A*, 116, pp. 170-197.

FOUR D RUBBER LATEX™, 2005. *Data sheet*. Four D Rubber Co.LTD.

GAD-EL-HAK, M., 1990. Control of low-speed airfoil aerodynamics. *AIAA Journal*, 28(9), pp. 1537-1552.

GAD-EL-HAK, M., 2001. Micro-air-vehicles: can they be controlled better?. *Journal of Aircraft*, 38(3), pp. 419-429.

GAITONDE, D., and VISBAL, M., 1998. High-order schemes for Navier-Stokes equations: algorithm and implementation into FDL3DI. Technical report AFRL-VA-WP-TR-1998-3060, *Air Force Research Laboratory, Wright-Patterson AFB*.

GAITONDE, D., and VISBAL, M., 1999. Further development of a Navier-Stokes solution procedure based on higher-order formulas. *AIAA Press*, Washington, DC., AIAA 99-0557.

GALVAO, R., ISRAELI, E., SONG, A., TIAN, X., BISHOP, K., SWARTZ, S., and BREUER, K., 2006. The Aerodynamics of compliant membrane wings modelled on mammalian flight mechanics. *36th AIAA Fluid Dynamics Conference and Exhibit*, Jun, San Francisco, AIAA 2006-2866, CA5-8.

GORDNIER, R., 2008. High fidelity computational simulation of a membrane wing airfoil. *46th AIAA Aerospace Sciences Meeting and Exhibit*, 7-10 Jan, Reno, Nevada, AIAA-2008-614.

GORDNIER, R., 2009. High fidelity computational simulation of a membrane wing airfoil. *Journal of Fluids and Structures*, 25, pp. 897-917.

GORDNIER, R., and ATTAR, P.J., 2009. Implicit LES simulations of a low Reynolds number flexible membrane wing airfoil. *47th AIAA Aerospace Sciences Meeting including the New Horizons Forum and Aerospace Exposition*, 5-8 Jan, Orlando, Florida, AIAA 2009-579, pp. 1-23.

GREENHALGH, S., CURTISS, H.C., and SMITH, B., 1984. Aerodynamic properties of a two-dimensional inextensible flexible airfoil. *AIAA Journal*, 22(7), pp. 865-870.

GURSUL, I., 2004. Vortex flows on UAVs: Issues and challenges. *The Aeronautical Journal*, 108(1090), pp. 597-610.

GURSUL, I., 2005. Review of unsteady vortex flows over slender delta wings. *Journal of Aircraft*, 42(2), pp. 299-319.

GURSUL, I., GORDNIER, R., and VISBAL, M., 2005. Unsteady aerodynamics of nonslender delta wings. *Progress in Aerospace Sciences*, 41(7), pp. 515-557.

HÄGGMARK, C.P., HILDINGS, C., and HENNINGSON, D.S., 2001. A numerical and experimental study of a transitional separation bubble. *Aerospace Science and Technology*, 5(5), pp. 317-328.

HASELGROVE, M., and TUCK, M., 1976. Stability properties of the two-dimensional sail model. *Society of Naval Architects and Marine Engineers, New England Sailing Yacht Symposium*, 24th Jan, New London, CN.

HEDENSTRÖM, A., JOHANSSON, L.C., WOLF, M., VON BUSSE, R., WINTER, Y., and SPEDDING, G.R., 2007. Bat flight generates complex aerodynamic tracks. *Science*, 316, pp. 894-897.

HILLIER R, and CHERRY N.J., 1981. The effect of stream turbulence on separation bubbles. *Journal of Wind Engineering and Industrial Aerodynamics*, 8, pp. 49-58.

HUANG, R.F., and LIN, C.L., 1995. Vortex shedding and shear-layer instability of wing at low-Reynolds numbers. *AIAA Journal*, 33, pp. 1398-1430.

HUANG, R.F., and LEE, H.W., 2000. Turbulence effect on frequency characteristics of unsteady motions in wake of wing. *AIAA Journal*, 38(1), pp. 87-94.

HUANG, R.F., WU, J.Y., JENG, J.H., and CHEN, R.C., 2001. Surface flow and vortex shedding of an impulsively started wing. *Journal of Fluid Mechanics*, 441, pp. 265-292.

HUBEL, T.Y., HRISTOV, N.I., SWARTZ, S.M., and BREUER, K.S., 2009. Time-resolved wake structure and kinematics of bat flight. *Experiments in Fluids*, published online 22 Feb 2009.

IFJU, P.G., JENKINS, D.A., ETTINGER, S., LIAN, Y., and SHYY, W., 2002. Flexible-wing-based micro air vehicles. *40th AIAA Aerospace Sciences Meeting and Exhibit*, Jan, Reno, Nevada, AIAA 2002-0705, pp. 1-13.

JACKSON, P.S., 1983. A simple model for elastic two-dimensional sails. *AIAA Journal*, 21(1), pp. 153-155.

JACKSON, P.S., and CHRISTIE, G.W., 1987. Numerical analysis of three-dimensional elastic membrane wings. *AIAA Journal*, 25(5), pp. 676-682.

JACKSON, P.S., and FIDDES, S., 1995. Two dimensional viscous flow past flexible sail sections close to ideal incidence. *The Aeronautical Journal*, 99, pp. 217-225.

JENKINS, C.H.M., and KORDE, U.A., 2006. Membrane vibration experiments: an historical review and recent results. *Journal of Sound and Vibration*, 295, pp. 602-613.

KINSLER, L.E., FREY, A.R., COPPENS, A.B., and SANDERS, J.V., 1982. *Fundamentals of Acoustics*. 4rd ed. New York: Wiley.

KIYA, M., and SASAKI, K., 1983. Free-stream turbulence effects on a separation bubble. *Journal of Wind Engineering and Industrial Aerodynamics*, 14, pp. 375-386.

LAITONE, E.V., 1997. Wind tunnel tests of wings at Reynolds numbers below 70000. *Experiments in Fluids*, 23(5), pp. 405-409.

LANG, M., RIST, U., and WAGNER, S., 2004. Investigations on controlled transition development in laminar separation bubble by means of LDA and PIV. *Experiments in Fluids*, 36(1), pp. 43-52.

LEVIN, O., and SHYY, W., 2001. Optimization of a low Reynolds number airfoil with flexible membrane. *Cmes-Computer Modelling in Engineering and Sciences*, 2(4), pp. 523-536.

LIAN, Y., and SHYY, W., 2003. Three-dimensional fluid-structure interactions of a membrane wing for micro air vehicle applications. *44th AIAA/ASME/ASCE/AHS Structures, Structural Dynamics, and Materials Conference*, 7-10 Apr, Norfolk, Virginia, AIAA 2003-1726.

LIAN, Y., SHYY, W., VIIERU, D., and ZHANG, B., 2003a. Membrane wing aerodynamics for micro air vehicles. *Progress in Aerospace Sciences*, 39(6-7), pp. 425-465.

LIAN, Y., SHYY, W., and HAFTKA, R., 2003b. Shape optimization of a membrane wing for micro air vehicles. *41th AIAA Aerospace Sciences Meeting and Exhibit*, 6-9 Jan, Reno, Nevada, AIAA 2003-0106, pp. 1-9.

LIAN, Y., and SHYY, W., 2005. Numerical simulations of membrane wing aerodynamics for micro air vehicle applications. *Journal of Aircraft*, 42(4), pp. 865-873.

LISSAMAN, P.B.S., 1983. Low-Reynolds-number airfoils. *Annual Review of Fluid Mechanics*, 15, pp.223-239.

LIU, H.T., 1992. Unsteady aerodynamics of a Wortmann wing at low Reynolds number. *Journal of Aircraft*, 29, pp. 532-539.

MATTHEWS, L.A., GREAVES, D.M., and WILLIAMS, C.J.K., 2008. Numerical simulation of viscous flow interaction with an elastic membrane. *International Journal for Numerical Methods in Fluids*, 57(11), pp. 1577-1602.

MCAULIFFE, B.R., and YARAS, M.I., 2007. Transition mechanisms in separation bubbles under low and elevated freestream turbulence. *Proceedings of the ASME Turbo Expo*, Montreal, Canada, GT2007-27605.

MIRANDA, S., VLACHOS, P.P., TELIONIS, D.P., and ZEIGER, M.D., 2005. Flow control of a sharp-edged airfoil. *AIAA Journal*, 43(4), pp. 716-726.

MUELLER, T.J., POHLEN, L.J., CONIGLIARO, P.E., and JANSEN, B.J., 1983. The influence of free-stream disturbances on low Reynolds number airfoil experiments. *Experiments in Fluids*, 1, pp. 3-14

MUELLER, T.J., 1999. Aerodynamic measurements at low Reynolds numbers for fixed wing micro-air vehicles. Presented at the RTO AVT/VKI special course on *Development and Operation of UAVs for Military and Civil Applications*, VKI, Belgium.

MUELLER, T.J., 2001. Fixed and flapping wing aerodynamics for micro air vehicle applications, *Progress in Astronautics and Aeronautics*, V-195. AIAA, Reston, VA.

MUELLER, T.J., and DELAURIER, J.D., 2003. Aerodynamics of small vehicles. *Annual Review of Fluid Mechanics*, 35, pp. 89-111.

MUIJRES, F.T., JOHANSSON, L.C., BARFIELD, R., WOLF, M., SPEDDING, G.R., and HEDENSTRÖM, A., 2008. Leading-edge vortex improves lift in slow-flying bats. *Science Magazine* (in Reports), 319, 29 Feb, pp. 1250-1253.

MURAI, H., and MURAYAMA, S., 1982. Theoretical investigation of sailwing airfoils taking account of elasticities. *Journal of Aircraft*, 19(5), pp. 385-389.

NEILSEN, J.N., 1963. Theory of flexible aerodynamic surfaces. *Journal of Applied Mechanics*, 30, pp. 435-442.

NEWMAN, B.G., and LOW, H.T., 1984. Two-dimensional impervious sails; experimental results compared with theory. *Journal of Fluid Mechanics*, 144, pp. 445-462.

NEWMAN, B.G., 1987. Aerodynamic theory for membranes and sails. *Progress in Aerospace Sciences*, 24, pp. 1-27.

NORBERG, U.M., and RAYNER, J.M.V., 1987. Ecological morphology and flight in bats (mammalian; Chiroptera): wing adaptations, flight performance, foraging strategy and echolocation. *Philosophical Transactions of the Royal Society B*, 316, pp. 335-427.

NULL, W., and SHKARAYEV, S., 2005. Effect of camber on the aerodynamics of adaptive-wing micro air vehicles. *Journal of Aircraft*, 42, pp. 1537-1542.

PELLETIER, A., and MUELLER, T.J., 2000. Low Reynolds number aerodynamics of low-aspect-ratio, thin/flat/cambered-plate wings. *Journal of Aircraft*, 37(5), pp. 825-832.

PETERS, W.H., and RANSON, W.F., 1982. Digital imaging techniques in experimental stress analysis. *Optical Engineering*, 21, pp. 427-431.

RISKIN, D.K., WILLIS, D.J., IRIARTE_DIAZ, J., HEDRICK, T.L., KOSTANDOV, M., CHEN, J., LAIDLAW, D.H., BREUER, K.S., and SWARTZ, S.M., 2008. Quantifying the complexity of bat wing kinematics. *Journal of Theoretical Biology*, 254, pp. 604-615.

ROSHKO, A., 1954. On the drag and shedding frequency of two-dimensional bluff bodies. *NACA TN*, 3169.

SCHMITZ, F.W., 1967. Aerodynamics of the model airplane, Part I, Airfoil measurements. *Redstone Arsenal Translation*, RSIC-721, Huntsville, AL.

SEIDE, P., 1977. Large deflections of rectangular membranes under uniform pressure. *International Journal of Nonlinear Mechanics*, 12, pp. 397-406.

SHYY, W., and SMITH, R., 1995. Computation of laminar flow and flexible structure interaction. *Computational Fluid Dynamics Review, A*, 1, pp.777-796.

SHYY, W., JENKINS, D.A., and SMITH, R.W., 1997. Study of adaptive shape airfoils at low Reynolds number in oscillatory flows. *AIAA Journal*, 35(9), pp. 1545-1548.

SHYY, W., BERG, M., and LJUNGQVIST, D., 1999a. Flapping and flexible wings for biological and micro air vehicles. *Progress in Aerospace Sciences*, 35(5), pp. 455-505.

SHYY, W., KLEVEBRING, F., NILSSON, M., SLOAN, J., CARROLL, B., and FUENTES, C., 1999b. Rigid and flexible low Reynolds number airfoils. *Journal of Aircraft*, 36(3), pp. 523-529.

SHYY, W., IFJU, P., and VIIERU, D., 2005. Membrane wing-based micro air vehicles. *Applied Mechanics Reviews*, 58(4), pp. 283-301.

SHYY, W., LIAN, Y., TANG, J., VIIERU, D., and LIU, H., 2008. *Aerodynamics of Low Reynolds Number Flyers*. New York, NY: Cambridge University Press.

SMITH, R., and SHYY, W., 1995a. Computational model of flexible membrane wings in steady laminar flow. *AIAA Journal*, 33(10), pp. 1769-1777.

SMITH, R., and SHYY, W., 1995b. Computation of unsteady laminar flow over a flexible 2D membrane wing. *Physics of Fluids*, 7(9), pp. 2175-2184.

SMITH, R., and SHYY, W., 1996. Computation of aerodynamic coefficients for a flexible membrane airfoil in turbulent flow: a comparison with classical theory. *Physics of Fluids*, 8(12), pp. 3346-3353.

SONG, A.J., and BREUER, K.S., 2007. Dynamics of a compliant membrane as related to mammalian flight. *45th AIAA Aerospace Sciences Meeting and Exhibit*, 8-11 Jan, Reno, Nevada, AIAA 2007-665.

SONG, A., TIAN, X., ISRAELI, E., GALVAO, R., BISHOP, K., SWARTZ, S., and BREUER, K., 2008a. The aero-mechanics of low aspect ratio compliant membrane wings, with applications to animal flight. *46th AIAA Aerospace Sciences Meeting and Exhibit*, AIAA 2008-517, pp 1-15.

SONG, A., TIAN, X., ISRAELI, E., GALVAO, R., BISHOP, K., SWARTZ, S., and BREUER, K., 2008b. Aeromechanics of membrane wings with implications for animal flight. *AIAA Journal*, 46(8), pp. 2096-2106.

STANFORD, B., ALBERTANI, R., VIIERU, D., SHYY, W., and IFJU, P., 2007a. Static aeroelastic model validation of membrane micro air vehicle wings. *45thAIAA Aerospace Sciences Meeting and Exhibit*, 8-11 Jan, Reno, Nevada, AIAA2007-1067, pp. 1-17.

STANFORD, B., SYTSMA, M., ALBERTANI, R., VIIERU, D., SHYY, W., and IFJU, P., 2007b. Static aeroelastic model validation of membrane micro air vehicle wings. *AIAA Journal*, 45(12), pp. 2828-2837.

STANFORD, B., IFJU, P., ALBERTANI, R., and SHYY, W., 2008. Fixed membrane wings for micro air vehicles: Experimental characterization, numerical modeling, and tailoring. *Progress in Aerospace Sciences*, 44, pp. 258-294.

STANFORD, B., and IFJU, P., 2009. Membrane micro air vehicles with adaptive aerodynamic twist: numerical modeling. *Journal of Aerospace Engineering*, 22(2), pp. 173-184.

SWARTZ, S.M., GROVES, M.S., KIM, H.D., and WALSH, W.R., 1996. Mechanical properties of bat wing membrane skin. *Journal of Zoology*, 239, pp. 357-378.

SWARTZ, S.M., 1998. Skin and bones: the mechanical properties of bat wing tissues. *In*: T.H. KUNZ, and P.A. RACEY, editors. *Bats: Phylogeny, Morphology, Echolocation, and Conservation Biology*. Washington, DC.: Smithsonian Institution Press, pp. 109-126.

SWARTZ, S.M., IRIARTE-DIAZ, J., and RISKIN, D.K., 2007. Wing structure and the aerodynamic basis of flight in bats. *45th AIAA Aerospace Sciences Meeting and Exhibit*, 8-11 Jan, Reno, Nevada, AIAA 2007-42, pp. 1-10.

TAMAI, M., MURPHY, J., and HU, H., 2008. An experimental study of flexible membrane airfoils at low Reynolds numbers. *46th AIAA Aerospace Sciences Meeting and Exhibit*, 7-10 Jan, Reno, Nevada.

TANI, I., 1964. Low-speed flows involving bubble separations. *Progress in Aerospace Sciences*, 5, pp. 70-103.

TAYLOR, G.S., SCHNORBUS, T., and GURSUL, I., 2003. An investigation of vortex flow over low sweep delta wings. *33th AIAA Fluid Dynamics Conference and Exhibit*, 23-26 Jun, Orlando, Florida, AIAA 2003-4021.

TAYLOR, G.S., and GURSUL, I., 2004a. Buffeting flows over a low-sweep delta wing. *AIAA Journal*, 42(9), pp. 1737-1745.

TAYLOR, G.S., and GURSUL, I., 2004b. Lift enhancement over a flexible delta wing. *2nd Flow Control Conference*, 28-1 Jul, Portland, Oregon, AIAA 2004-2618.

TAYLOR, G.S., WANG, Z., VARDAKI, E., and GURSUL, I., 2007. Lift enhancement over flexible nonslender delta wings. *AIAA Journal*, 45(12), pp. 2979-2993.

THWAITES, B., 1960. *Incompressible Aerodynamics*, New York: Dover.

THWAITES, B., 1961. The aerodynamic theory of sails I: Two-dimensional sails. *Proceedings of the Royal Society, Series A*, 261, pp. 402-442.

TORRES, G.E., and MUELLER, T.J., 2000. Aerodynamic characteristics of low aspect ratio wings at low Reynolds numbers. *Proceedings of the Conference on Fixed, Flapping and Rotary Wing Vehicles at Very Low Reynolds Numbers*, 5-7 Jun, University of Notre Dame, Notre Dame, Indiana, pp. 278-305.

TORRES, G.E., and MUELLER, T.J., 2004. Low-aspect-ratio wing aerodynamics at low Reynolds numbers. *AIAA Journal*, 42(5), pp. 865-873.

VARDAKI, E., GURSUL, I., and TAYLOR, G.S., 2005. Physical mechanisms of lift enhancement for flexible delta wings. *43th AIAA Aerospace Sciences Meeting and Exhibit*, 10-13 Jan, Reno, Nevada, AIAA 2005-867.

VIDELER, J.V., 2005. *Avian Flight*. New York City, NY: Oxford University Press.

VIIERU, D., LIAN, Y., SHYY, W., and IFJU, G., 2003. Investigation of tip vortex on aerodynamic performance of a micro aerial vehicle. *33rd AIAA Fluid*

Dynamics Conference and Exhibit, 23-26 Jun, Orlando, Florida, AIAA 2003-3597.

VIIERU, D., ALBERTANI, R., SHYY, W., and IFJU, G., 2005. Effect of tip vortex on wing aerodynamics of micro air vehicles. *Journal of Aircraft*, 42(6), pp. 1530-1536.

VISBAL, M.R., and GAITONDE, D., 1999. High-order accurate methods for complex unsteady subsonic flows. *AIAA Journal*, 37(10), pp. 1231-1239.

WARD, J.R., 1963. The behavior and effects of laminar separation bubbles on airfoils in incompressible flow. *Journal of the Royal Aeronautical Society*, 67, pp. 83-90.

WASZAK, M.R., JENKINS, L.N., and IFJU, P., 2001. Stability and control properties of an aeroelastic fixed wing micro aerial vehicle. *AIAA Atmospheric Flight Mechanics Conference*, 6-9 Aug, Montreal, Canada, pp. 1-11.

WATMUFF, J.H., 1999. Evolution of a wave packet into vortex loops in a laminar separation bubble. *Journal of Fluid Mechanics*, 397, pp. 119-169.

WHITE, F.M., 1999. *Fluid Mechanics*. 4th ed. McGraw-Hill Series in Mechanical Engineering.

WINTER, Y., and VON HELVERSEN, O., 1998. The energy cost of flight: do small bats fly more cheaply than birds?. *Journal of Comparative Physiology B-Biochemical Systemic and Environmental Physiology*, 168(2), pp. 105-111.

WOOTTON, R., 2000. From insects to microvehicles. *Nature*, 403, pp. 144-145.

WU, J.Z., LU, X., DENNY, A.G., FAN, M., and WU, J.M., 1998. Post-stall flow control on an airfoil by local unsteady forcing. *Journal of Fluid Mechanics*, 371, pp. 21-58.

YARUSEVYCH, S., SULLIVAN, P.E., and KAWALL, J.G., 2006. Coherent structures in an airfoil boundary layer and wake at low Reynolds numbers. *Physics of Fluids*, 18(4), pp. 1-11.

ZBIKOWSKI, R., 2002. On aerodynamic modelling of an insect-like flapping wing in hover for micro air vehicles. *Philosophical Transactions: Mathematical, Physical and Engineering Sciences*, 360(1791), pp. 273-290.

ZHANG, W., HAIN, R., and KAHLER, J., 2008. Scanning PIV investigation of the laminar separation bubble on a SD7003 airfoil. *Experiments in Fluids*, 45(4), pp. 725-743.

LIST OF PUBLICATIONS

Book Chapter

ROJRATSIRIKUL, P., WANG, Z., and GURSUL, I., 2010. Unsteady fluid–structure interactions of membrane airfoils at low Reynolds numbers. *In*: G.K. TAYLOR, M.S. TRIANTAFYLLOU, and C. TROPEA, eds. *Animal Locomotion: The Physics of Flying, The Hydrodynamics of Swimming*. Springer Berlin Heidelberg, pp. 297-310.

Journal Articles

ROJRATSIRIKUL, P., WANG, Z., and GURSUL, I., 2010. Effects of pre-strain and excess length on unsteady fluid-structure interactions of membrane airfoils. *Journal of Fluids and Structures*, 26(3), pp. 359-376.

ROJRATSIRIKUL, P., WANG, Z., and GURSUL, I., 2009. Unsteady fluid–structure interactions of membrane airfoils at low Reynolds numbers. *Experiments in Fluids*, 46(5), pp. 859-872.

Conference Papers

ROJRATSIRIKUL, P., WANG, Z., and GURSUL, I., 2010. Unsteady aerodynamics of low aspect ratio membrane wings. *48th AIAA Aerospace Sciences Meeting including the New Horizons Forum and Aerospace Exposition*, 4-7 Jan, Orlando, Florida, AIAA 2010-729, pp. 1-19.

ROJRATSIRIKUL, P., WANG, Z., and GURSUL, I., 2009. Effects of pre-strain and excess length on unsteady fluid-structure interactions of membrane airfoils. *47th AIAA Aerospace Sciences Meeting including the New Horizons Forum and Aerospace Exposition*, 5-8 Jan, Orlando, Florida, AIAA 2009-578, pp. 1-20.

ROJRATSIRIKUL, P., WANG, Z., and GURSUL, I., 2008. Unsteady aerodynamics of membrane airfoils. *46th AIAA Aerospace Sciences Meeting and Exhibit*, 7-10 Jan, Reno, Nevada, AIAA 2008-613, pp. 1-20.

APPENDIX A

Journal Article 1

ROJRATSIRIKUL, P., WANG, Z., and GURSUL, I., 2009. Unsteady fluid–structure interactions of membrane airfoils at low Reynolds numbers. *Experiments in Fluids*, 46(5), pp. 859-872.

APPENDIX B

Journal Article 2

ROJRATSIRIKUL, P., WANG, Z., and GURSUL, I., 2010. Effects of pre-strain and excess length on unsteady fluid-structure interactions of membrane airfoils. *Journal of Fluids and Structures*, 26(3), pp. 359-376.